Studies of the Electron Neutrino Charged-current Interaction on ^{127}I

by

Peibo An

Department of Physics
Duke University

Date: _____

Approved:

_____
Phillip Spencer Barbeau, Supervisor

_____
Kate Scholberg

_____
Steffen A Bass

_____
Calvin R Howell

_____
Kenneth R Brown

Dissertation submitted in partial fulfillment of the requirements for the degree of
Doctor of Philosophy in the Department of Physics
in the Graduate School of Duke University
2022

Abstract

Studies of the Electron Neutrino Charged-current Interaction on ^{127}I

by

Peibo An

Department of Physics
Duke University

Date: _____

Approved:

_____
Phillip Spencer Barbeau, Supervisor

_____
Kate Scholberg

_____
Steffen A Bass

_____
Calvin R Howell

_____
Kenneth R Brown

An abstract of a dissertation submitted in partial fulfillment of the requirements for the degree of Doctor of Philosophy in the Department of Physics in the Graduate School of Duke University
2022

Abstract

An inclusive measurement of the cross section of the electron neutrino charged-current interaction on ^{127}I can probe the quenching of g_A, the axial-vector coupling constant, which affects the rate of neutrinoless double beta decays, and contribute to the design of next-generation solar neutrino detectors. At the Los Alamos Meson Production Facility (LAMPF), an exclusive measurement of the flux-averaged cross section was measured to be [2.84 ± 0.91 (stat) ± 0.25 (syst)] × 10^{-40} cm^2 [1]. This measurement has a large statistical error and only counts the number of ^{127}Xe in the bound state. To make a first measurement of the inclusive cross section with lower statistical uncertainties, a 185-kg NaI[Tl] prototype detector, NaIνE-185, was deployed by the COHERENT collaboration at the Spallation Neutron Source. To study electron neutrino charged-current interaction detection efficiencies, simulations were performed. To explore new approaches of steady state background rejection, a convolutional neural network (CNN) classifier and a XGBoost based classifier were developed. The best 4-class model, tested with simulations, achieved a 50.2% classification accuracy. To address the non-linearity of NaI[Tl] crystals at high energies, calibrations using Michel positrons from stopped muon decays were performed. The cross section measurement was done through probability density function (PDF) fitting. The flux-averaged total inclusive cross section, excluding forbidden transitions, was measured to be [9.2 + 2.1 − 1.8 (stat+syst)] × 10^{-40} cm^2, rejecting the null hypothesis by 5.8 σ.

Contents

List of Tables

List of Figures

Acknowledgements

Huge thanks to my parents for their financial and emotional support for the past decade. Huge thanks to my advisor, Dr. Phil Barbeau, for all his support. Huge thanks to Dr. Sam Hedges, Dr. Daniel Pershey, Dr. Long Li, Dr. Kate Scholberg and Dr. Diane Markoff for all their help along the way. Huge thanks to Dr. Jing Liu and Dr. Daniel Salvat for helping me with Geant4. Huge thanks to my PhD committee members for all their effort and support. The list could go on forever, so thanks to everyone who ever aided me. Last but not least, a big shout-out to my beloved cat, Kamali. I've done few things right in the past 10 years, but I adopted her.

1

Introduction

1.1 Neutrinos

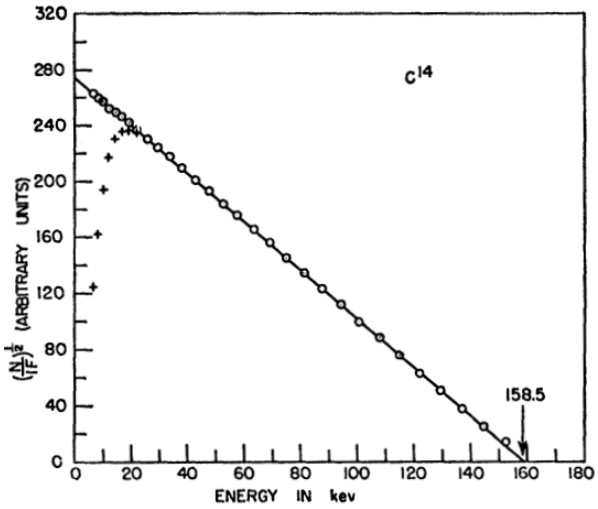

FIGURE 1.1: Beta decay spectrum of ^{14}C from A. V. Pohm et al. [2].

In 1911, Lise Meitner and Otto Hahn discovered that beta spectra consist of multiple different lines, unlike alpha spectra [3]. Later in 1913, Jean Danysz presented in his thesis that Radium B+C (beta decay of ^{214}Pb and ^{214}Bi) spectra contains 27 lines [4]. These results hinted, for the first time, that beta spectra are continuous

[3]. Figure 1.1 demonstrates the continuous spectrum of electrons emitted by ^{14}C in its beta decay. In this case, the law of energy conservation would be violated as the electrons were observed to carry less energy than the mass difference between the parent nucleus and the daughter nucleus. In 1930, Wolfgang Pauli proposed a new type of light neutral lepton called the neutrino, attempting to address this issue [5]. Shortly after Pauli's proposal, Enrico Fermi in 1934 incorporated the idea of neutrinos into his theory of beta decay [6]. Because neutrinos have no charge, they only interact through weak interactions or gravity. Additionally, neutrinos were believed to be massless. As a result, they were much much more difficult to detect than electrons.

In 1953, Reines and Cowan made the first tentative identification of electron neutrinos through inverse beta decay at the Hanford reactor [7]. This was later confirmed in 1956 at the Savannah River Plant [8]. Years later, this was followed by the discovery of two more neutrino flavors. In 1962, Danby et al. observed two different types of neutrinos, electron neutrinos and muon neutrinos at the Brookhaven Alternating Gradient Synchrotron [9]. Only two types of neutrinos were searched for because the tau lepton was not discovered until 1975 [10]. Finally in 2001, the DONUT collaboration made the first direct observation of tau neutrinos at the Fermi National Laboratory [11].

In 1976, Bahcall and Davis successfully measured the rate of the solar neutrino charged-current interaction on ^{37}Cl using the Brookhaven ^{37}Cl detector in a Homestake gold mine [12]. However, as noted by Bahcall, the measured solar neutrino rate was only about a third of the expected value from the Standard Solar Model [12, 13]. As a result, this discrepancy became known as the "solar neutrino problem". One of the proposals to address this problem was the possibility of neutrino oscillation, which introduced the mixing of neutrino mass and flavor eigenstates. In short, neutrinos could change flavors while traveling due to their finite mass. In 1998, the

Super-Kamiokande collaboration successfully observed atmosphere neutrino oscillations [14] through muon neutrino deficits. This result demonstrated that neutrinos have finite mass. However, the neutrino oscillation experiments could only help probe the differences of squared neutrino-mass eigenvalues, rather than the absolute mass [15].

There are three ways to measure the effective mass of neutrinos, defined as the incoherent sum of neutrino masses and lepton mixing matrix elements [16]. The first one is using cosmology models, coupled with astrophysical observations. Even though neutrinos have small mass, they have a density of 112 cm^{-3} per flavor in the universe [17]. As a result, neutrinos could contribute to the density of the universe. Constraints on this effect can be extracted through cosmological observations, with the assumption of the Standard Cosmological Model (ΛCDM) [18]. In 2022, the Dark Energy Survey (DES) collaboration reported that $\sum m_\nu < 0.13$ eV at a 95% confidence interval in ΛCDM, combining its data from galaxy clustering and gravitational lensing with other external data [19], such as the measurements of the Cosmic Microwave Background (CMB) by the Planck collaboration [20]. Another way to measure the effective mass of neutrinos is through beta decay. This method does not depend on cosmological models but is subject to the sensitivity of energy measurements. In 2022, the KATRIN Collaboration updated the upper limit of the effective mass of a neutrino, 0.8 eV/c^2 with a 0.7 eV/c^2 sensitivity at a 90% confidence interval [15].

Last but not least, neutrinoless double beta ($0\nu\beta\beta$) decay can also be used to measure the effective mass of neutrinos. If neutrinos are Majorana particles, meaning that neutrinos are their own anti-particles, they could annihilate each other in the process of double beta decay. The second order process for double beta decay was first considered by Maria Goeppert-Mayer in 1935 [21]. The neutrinoless decay was formulated by Ettore Majorana two years later [22]. Searches for $0\nu\beta\beta$ decay can be

traced back to 1966 [23, 24].

1.2 $0\nu\beta\beta$ Decay

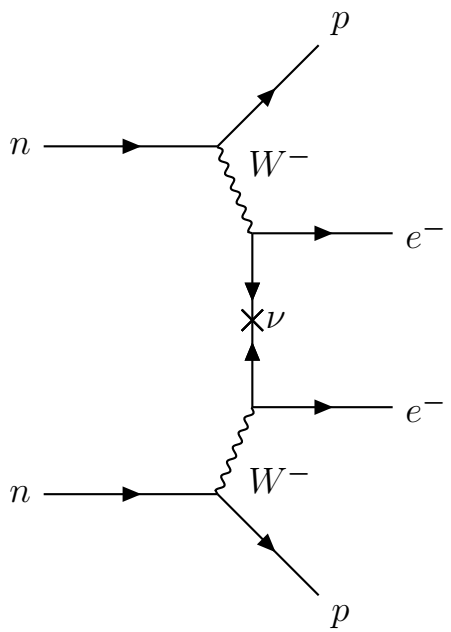

FIGURE 1.2: Feynman diagram of $0\nu\beta\beta$ decay.

Searches for $0\nu\beta\beta$ decay are of great importance in experimental particle physics because they offer the best sensitivity on Majorana nature of neutrinos and small neutrino masses [25]. As shown in figure 1.2, in this process, two neutrons transform into two protons by the emission of two electrons. There are many experimental programs that study $0\nu\beta\beta$ decay [26], including but not limited to LEGEND [27], nEXO [28], NEXT [29], CUPID [30], KamLANDZen [31], PandaX-III [32], SNO+ [33] and SuperNEMO [34, 35]. Using Fermi's golden rule, the inverse of the $0\nu\beta\beta$ decay half-life, $[T^{0\nu}_{\frac{1}{2}}]^{-1}$, can be written as (from ref [36]):

$$[T^{0\nu}_{\frac{1}{2}}]^{-1} = |\frac{m_{\beta\beta}}{m_e}|^2 [G^{0\nu}(E_0, Z)] |M^{0\nu}(\frac{g_A^{\text{eff}}}{g_A})^2|^2 \tag{1.1}$$

where $m_{\beta\beta}$ is the effective Majorana mass, $G^{0\nu}(E_0, Z)$ is the phase-space factor, which includes g_A^4, and $M^{0\nu}$ is the nuclear matrix element. The exceedingly long half-life combined with cosmic backgrounds makes $0\nu\beta\beta$ decay challenging to detect. Since the half-life depends on $(\frac{g_A^{\text{eff}}}{g_A})^4$, g_A quenching ($\frac{g_A^{\text{eff}}}{g_A} < 1$) would make it significantly more difficulty to detect the $0\nu\beta\beta$ decay. In 2022, the KamLAND-Zen Collaboration reported a lower bound of the $0\nu\beta\beta$ decay half-life: 2.3×10^{26} yr at a 90% confidence interval [37]. This half-life bound corresponds to upper limits on the effective neutrino mass of 36 – 156 meV [37].

1.3 Thesis Overview

In this thesis I present my work on electron neutrino charged-current interaction on ^{127}I ($^{127}\text{I}(\nu_e, e^-)^{127}\text{Xe}$). This work will lead to the first measurement of the inclusive cross section of this process, which offers insights on g_A quenching and other physics. In chapter 2, I cover the theories, motivations and a past measurement of the cross section of $^{127}\text{I}(\nu_e, e^-)^{127}\text{Xe}$. In chapter 3, I go through the COHERENT experiment, the design, setup and analysis chain of the NaIνE-185 detector. Then in chapter 4, I provide details and results of the relevant simulations performed. In chapter 5, I showcase machine learning approaches to reject backgrounds and select signals. In chapter 6, I go over high energy calibrations of the NaIνE-185 detector with Michel positrons. Finally in chapter 7, I present the results of the analysis on the cross section measurement.

2

Neutrino Charged-current Interactions

2.1 Formalism

A brief summary of the formalism of neutrino charged-current interaction, to be described in this work, is mainly inspired (section 2.1, 2.2 and 2.4.2 in particular) by the work of Dr. Sam Hedges [38]. The charged-current interaction is one of two types of weak interactions. Neutrino charged-current interaction is mediated through $W^{\pm}$

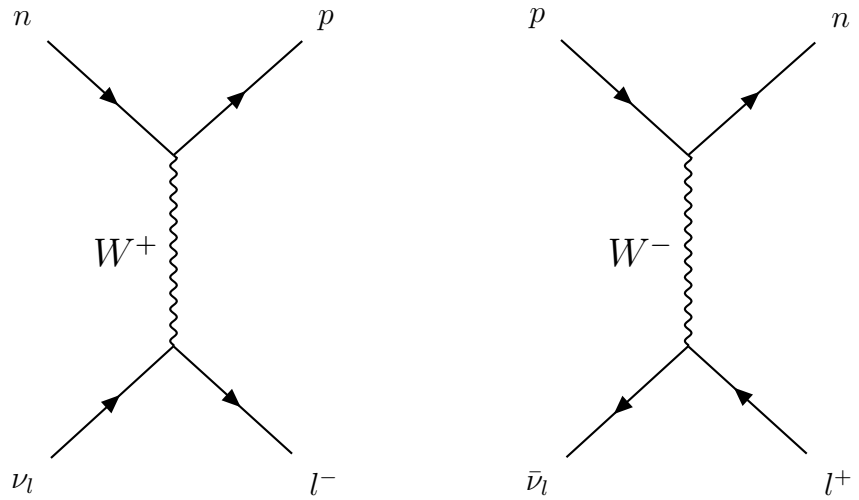

FIGURE 2.1: Feynman diagram examples for neutrino charged-current interaction (left) and anti-neutrino charged-current interaction (right).

as shown in the figure 2.1

The general expression of the differential cross section for a collision of two particles producing N outgoing particles, derived from the scattering matrix, can be written as [39]:

$$d\sigma = (2\pi)^4 \delta^{(4)} \left(\sum_f p_f^{'} - \sum_i p_i \right) \frac{1}{4[(p_{i,1} \cdot p_{i,2})^2 - (m_1 m_2)^2]^{1/2}} \left(\prod_f \frac{d^3 p_f^{'}}{(2\pi)^3 2E_f^{'}} \right) |\mathcal{M}|^2 \tag{2.1}$$

where $\mathcal{M}$ is the invariant matrix element, f represents the final particles and i represents the initial particles and $\delta^{(4)}(E) = (\frac{1}{2\pi} \int e^{iEt} dt)^4$. Dr. Tina J. Leitner [40] showed that in the Born approximation and under low momentum transfer limit ($q^2 \ll M_W^2$), the matrix element can be written as a product of a leptonic component and a hadronic component. For weak interactions, such as neutrino charged-current interaction, the hadronic component is more complicated to evaluate as parity and current conservation are no longer constraints [40]. To make the cross section easier to simulate, Dr. Steven Gardiner applied the following approximations when studying neutrino charged-current interaction on ^{40}Ar [41]:

- The *impulse approximation*, in which the neutrino interacts with only a single nucleon.
- The *allowed approximation*: the long-wavelength limit, in which the four-momentum transfer q goes to 0, and the slow-nucleon limit, in which $|\mathbf{p}_N|/m_N$ goes to 0, where $\mathbf{p}_N$ is the initial three-momentum of the struck nucleon and m_N is its mass.

Under this approach, the differential cross section in the center-of-momentum (CM) frame for a neutrino charged-current transition to a particular allowed nuclear final

state can be written as [41]:

$$\frac{d\sigma}{d\cos\theta_\ell} = \frac{G_F^2}{2\pi}\mathcal{F}_{\rm CC}\left[\frac{E_i E_f}{s}\right] E_\ell\,|\mathbf{p}_\ell|\left[(1+\beta_\ell\cos\theta_\ell)\,B(\mathrm{F}) + \left(1-\frac{1}{3}\beta_\ell\cos\theta_\ell\right)B(\mathrm{GT})\right] \tag{2.2}$$

where G_F is the Fermi constant, s is the square of the total energy in the CM frame, $E_i(E_f)$ is the total energy of the initial (final) nucleus, E_l is the total energy of the final-state lepton, $\mathbf{p}_l$ is the three-momentum of the lepton, β_l=$|\mathbf{p}_l|/E_l$ is the speed of the lepton, θ is the scattering angle defined with respect to the incident neutrino direction, and $\mathcal{F}_{\rm CC}$ for charged-current is defined as [41]:

$$\mathcal{F}_{\rm CC} = |V_{ud}|^2 F_C \tag{2.3}$$

where V_{ud} is the Cabibbo-Kobayashi-Maskawa matrix element connecting the up and down quarks and F_C is the Coulomb correction factor accounting for the electromagnetic interaction between the outgoing lepton and the nucleus in an approximate way. $B(\mathrm{F})$ and $B(\mathrm{GT})$ are the spin-reduced Fermi and Gamow-Teller nuclear matrix elements defined as [41]:

$$B\,(\mathrm{F}) = \begin{cases} \frac{g_V^2}{2J_i+1}\,|\langle J_f\,\|\mathcal{O}_{\rm F}\|\,J_i\rangle|^2 & \text{if } J_i = J_F \text{ and } \Pi_i = \Pi_f \\ 0 & \text{otherwise} \end{cases} \tag{2.4}$$

and:

$$B\,(\mathrm{GT}) = \begin{cases} \frac{g_A^2}{2J_i+1}\,|\langle J_f\,\|\mathcal{O}_{\rm GT}\|\,J_i\rangle|^2 & \text{if } |J_i-1| \le J_f \le J_i+1 \text{ and } \Pi_i = \Pi_f \\ 0 & \text{otherwise} \end{cases} \tag{2.5}$$

where g_V is the vector weak coupling constant, g_A is the axial-vector weak coupling constant and $J_i(J_f)$ is the initial (final) nuclear spin. Both $B(\mathrm{F})$ and $B(\mathrm{GT})$ are subject to certain spin-parity selection rules. For neutrino charged-current interaction, the Fermi $\mathcal{O}_{\rm F}$ and Gamow-Teller operator $\mathcal{O}_{\rm GT}$ are defined as [41]:

$$\mathcal{O}_{\rm F} = \sum_{n=1}^{A} t_-(n) \tag{2.6}$$

and:

$$\mathcal{O}_{\mathrm{GT}} = \sum_{n=1}^{A} \boldsymbol{\sigma}(n) t_{-}(n) \tag{2.7}$$

where $\boldsymbol{\sigma}$ is the Pauli vector and t_{-} is the isospin lowering operator. For anti-neutrino charged-current interactions, t_{-} needs to replaced by t_{+}, the isospin raising operator. Putting everything together and doing the integral in equation 2.2 over $\cos\theta_l$ gives a total cross section neglecting forbidden transitions [41]:

$$\sigma = \frac{G_F^2}{\pi} \mathcal{F}_{\mathrm{CC}} \left[\frac{E_i E_f}{s} \right] E_\ell \left| \mathbf{p}_\ell \right| \left[B(\mathrm{F}) + B(\mathrm{GT}) \right] \tag{2.8}$$

2.2 Strength Distributions

As shown in the previous section, understanding the Gamow-Teller strength distributions $B(\mathrm{GT})$ and the Fermi strength distributions $B(\mathrm{F})$ is crucial to the estimation of the cross section. $B(\mathrm{F})$ has a much easier form compared to $B(\mathrm{GT})$. The majority of it is centered around the isobaric analog state (IAS). The strength of the IAS for neutrino interactions is given by the simple sum rule:

$$B(\mathrm{F}) = g_V^2 (N - Z) \tag{2.9}$$

where N is the neutron number and Z is the proton number. For anti-neutrino interactions, $(N - Z)$ becomes $(Z - N)$. The Gamow-Teller strength distributions follows a similar sum rule [42]:

$$S(\mathrm{GT}) = \sum_{f,i} \left| \left\langle J_f \left\| \mathcal{O}_{\mathrm{GT}}^{-} \right\| J_i \right\rangle \right|^2 - \sum_{f,i} \left| \left\langle J_f \left\| \mathcal{O}_{\mathrm{GT}}^{+} \right\| J_i \right\rangle \right|^2 = 3(N - Z) \tag{2.10}$$

where the added terms are defined without g_A unlike equation 2.5. There are different ways to actually measure $B(\mathrm{GT})$, such as using (p, n) reactions, beta decay life times, etc. In addition, they can be predicted by theoretical models, such as the

shell model [43], the quasi-random phase approximation (QRPA) [44] and the ab-initio approaches [45]. In this section, theories behind extracting $B(\mathrm{GT})$ from (p,n) reactions are discussed, due to their popularity.

In 1980, Bainum, et al. [46] observed a correlations between the 0° (p,n) scattering and Gamow-Teller strength distributions in ^{90}Zr. This result led Taddeucci, et al. [47], who later published their result in 1987, to conduct a systematic comparison of Gamow-Teller and Fermi strength distributions from (p,n) reactions and measurements of the strength from beta decay [38]. The definition of $B(\mathrm{GT})$ and $B(\mathrm{F})$ in the work of Taddeucci, et al. [47] are slightly different compared to equation 2.5 and 2.4 so to avoid confusion define:

$$\bar{B}(\alpha) = \frac{B(\alpha)}{g_\beta^2} \tag{2.11}$$

where α is either F or GT and β is either V or A. Then the cross section of (p,n) reactions can be written as:

$$\sigma = \hat{\sigma}_\alpha \left(E_p, A\right) F_\alpha(q,\omega)\bar{B}(\alpha) \tag{2.12}$$

where α is either F or GT, $\hat{\sigma}$ is the unit cross section of major interest, E_p is the bombarding energy, A is the atomic mass of the target nucleus, q is the momentum transfer, ω is the energy loss, $\bar{B}(\alpha)$ is the strength and F_α is the factor that describes the shape of σ distribution, as a function of q and ω. In the limit of zero momentum transfer and energy loss, F_α goes to 1.

Meanwhile in beta decay, the strengths are related to the lifetime:

$$g_V^2\bar{B}(\mathrm{F}) + g_A^2\bar{B}(\mathrm{GT}) = \frac{K}{ft} \tag{2.13}$$

where

$$\frac{K}{g_V^2} = 6166 \pm 2 \text{ sec}$$
$$\left(\frac{g_A}{g_V}\right)^2 = (1.260 \pm 0.008)^2 \tag{2.14}$$

and ft is related to the lifetime.

To understand the contribution of GT and F cross sections to the cross section at 0° for 0^+ and 1^+ mixed transitions, Taddeucci, et al. [47] used the ratio of unit cross section R^2:

$$R\left(E_p, A\right)^2 = \frac{\hat{\sigma}_{\mathrm{GT}}\left(E_p, A\right)}{\hat{\sigma}_{\mathrm{F}}\left(E_p, A\right)} \tag{2.15}$$

The experimental values of R^2 can be extracted from cross sections for $0^+ \rightarrow 0^+$ and $0^+ \rightarrow 1^+$ (p, n) transitions in target nucleus with even A and $N - Z \neq 0$ using the "exact" definition:

$$R^2 = \frac{\sigma_{\mathrm{GT}}\left(q_1, \omega_1\right)}{\sigma_{\mathrm{F}}\left(q_0, \omega_0\right)} \frac{N-Z}{\bar{B}(\mathrm{GT})} \frac{F\left(q_0, \omega_0\right)}{F\left(q_1, \omega_1\right)} \tag{2.16}$$

where the cross sections are for $\theta = 0^\circ$ in order to minimize the distortion and momentum transfer corrections. For nuclei with odd A, the 0° non-spin-flip cross section is an incoherent sum of Fermi and Gamow-Teller strengths and as a result:

$$R^2 = \frac{\sigma_{\mathrm{GT}}}{\sigma_{\mathrm{IAS}}} \frac{N-Z}{B_1(\mathrm{GT})} \frac{K\left(\omega_0\right)}{K\left(\omega_1\right)} \left[1 - \frac{\sigma_{\mathrm{GT}}}{\sigma_{\mathrm{IAS}}} \frac{B_0(\mathrm{GT})}{B_1(\mathrm{GT})} \frac{K\left(\omega_0\right)}{K\left(\omega_1\right)}\right]^{-1} \tag{2.17}$$

where $K(\omega)$ is the kinematic factor and the subscripts "0" and "1" refer to the IAS and pure GT transition respectively.

Then after comparing the strengths from (p, n) and beta decay for multiple targets, Taddeucci, et al. identified that:

$$R(E_p) = \frac{E_p}{E_0} \tag{2.18}$$

where

$$E_0 = 55 \pm 0.4 \text{ MeV} \tag{2.19}$$

As a result, the Gamow-Teller strength distributions $B(\text{GT})$ can be calculated by combining equation 2.16, 2.17 and 2.18. It turns out that the measured GT strength is smaller than the nominal value from the sum rule. One possible explanation, also the one of the motivations of this work, is the g_A quenching, which will be discussed in later sections. A review of possible reasons for g_A quenching is also described in reference [48].

2.3 Neutrino Charged-current Interaction on ^{127}I

$$\nu_e + {}^{127}\text{I} \rightarrow e^- + {}^{127}\text{Xe}^* \tag{2.20}$$

This work studies the cross section of electron neutrino charged-current interaction on ^{127}I, whose reaction formula is described above. When an electron neutrino interacts with a ^{127}I nucleus, an electron and a ^{127}Xe can be produced. The neutrino threshold energy of this process is 0.662 MeV. This can be estimated from the rest mass difference between ^{127}I and ^{127}Xe. However, transitions from the ground state of ^{127}I to ^{127}Xe is forbidden. As a result, the effective threshold is 0.789 MeV. This will leave the produced ^{127}Xe in the 125 KeV first excited ($\text{J}^\pi = \frac{3}{2}^+$) state. The * in the reaction formula indicates that the produced ^{127}Xe can be in the ground state as well as excited states. The ^{127}Xe in the ground state ($\text{J}^\pi = \frac{1}{2}^+$) decays into ^{127}I ground state ($\text{J}^\pi = \frac{5}{2}^+$) through orbital electron capture. During this process, ^{127}Xe atoms transition to $\text{J}^\pi = \frac{1}{2}^+$ and $\text{J}^\pi = \frac{3}{2}^+$ ^{127}I excited states with an almost 50% branching ratio, as shown in figure 2.2. Then these states emit 375 keV and 203 keV gamma ray or gamma ray series respectively and reach $\text{J}^\pi = \frac{5}{2}^+$ ground state. In the process, Auger electrons may also be emitted. Since the ^{127}Xe nuclei can be in the excited states especially for neutrinos with higher energies, the final state of the

process could also include:

- Protons from de-excitation
- Neutrons separated from energetic ^{127}Xe nuclei
- Gamma rays from de-excitation
- Alpha particles from de-excitation

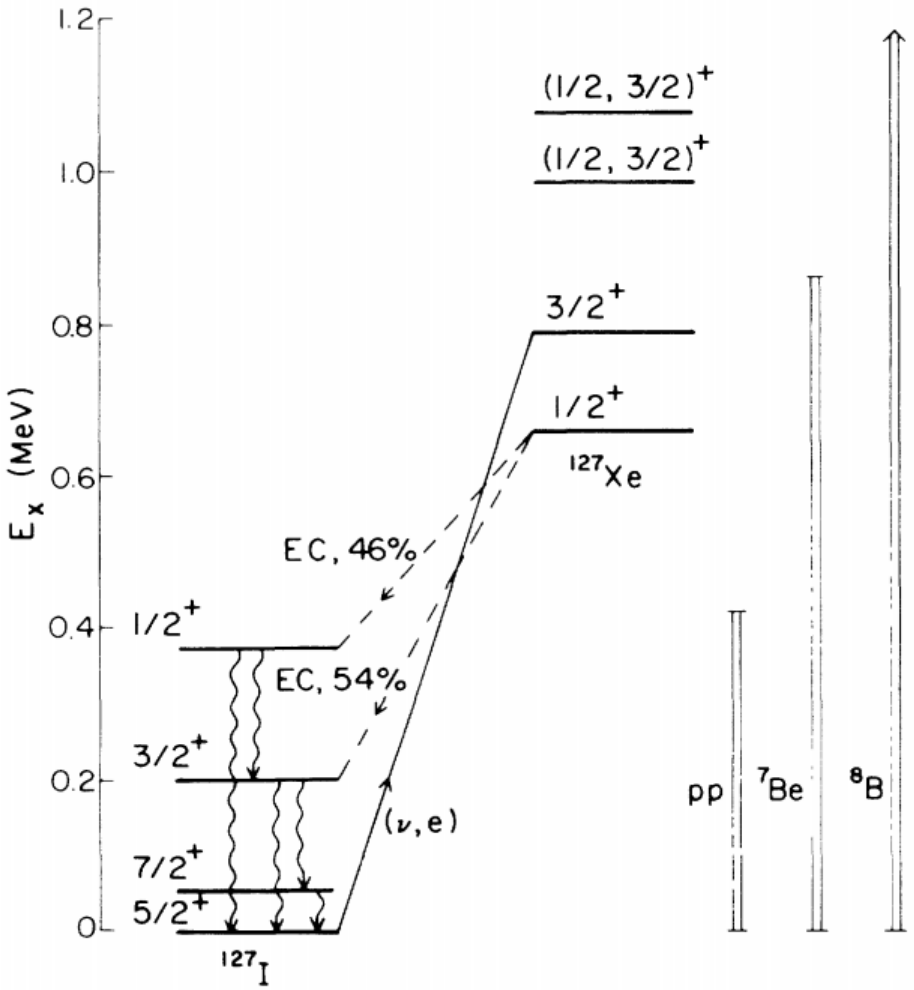

FIGURE 2.2: The level scheme showing weak transitions between ^{127}I and ^{127}Xe from Haxton [49]. The energy ranges of solar neutrinos are plotted on the right.

Table 2.1: Thresholds for different end states of charged-current interaction on ^{127}I, courtesy of Sam Hedge [38].

Reaction	Threshold [MeV]
$\nu_e + {}^{127}\mathrm{I} \rightarrow {}^{127}\mathrm{Xe} + e^-$	0.789
$\nu_e + {}^{127}\mathrm{I} \rightarrow {}^{126}\mathrm{Xe} + e^- + n$	7.886
$\nu_e + {}^{127}\mathrm{I} \rightarrow {}^{125}\mathrm{Xe} + e^- + 2n$	17.934
$\nu_e + {}^{127}\mathrm{I} \rightarrow {}^{126}\mathrm{I} + e^- + p$	8.362

The thresholds for some of the possible states are listed in table 2.1. All the de-excitation products could produce subsequent processes that cause energy depositions in a detector. For example, the emitted neutrons could cause nuclear recoils and eventually be captured on an I nucleus and emit gamma rays. These gamma rays could then cause pair productions or Compton scatterings. Therefore, a lot of factors have to be considered in order to measure the inclusive cross section. This work probes the physics behind this charged-current interaction through simulations, which will be explained in chapter 4.

2.4 Motivation

2.4.1 g_A Quenching

When studying the beta decay rate of nuclei with a mass number between 40 and 50, G. Martínez-Pinedo et al. [50] found that the experimental Gamow-Teller strengths, summed over certain low-lying states and scaled, were smaller than calculated values. Then it was suspected that the effective axial-vector coupling constant has a smaller value than the theoretical g_A ($g_A^{\mathrm{eff}} = 0.74 g_A$) [50]. What's more, this problem is not confined to just beta decay or electroweak operators. For example, some (p, n) and (n, p) experiments report the sum of $S_-(\mathrm{GT})$ values is considerably less than that from the sum rule defined in equation 2.10 (typically about half) [51]. One notable effect of g_A quenching is the reduction of the sensitivity of the next generation

neutrinoless double beta ($0\nu\beta\beta$) decay detectors. As seen in equation 1.1, the decay rate depends on g_A quenching to the 4th power. For example, if g_A quenching is about 0.74, then the $0\nu\beta\beta$ decay rate would be about only 30% of its theoretical value. As a result, the sensitivity of detectors would drop significantly.

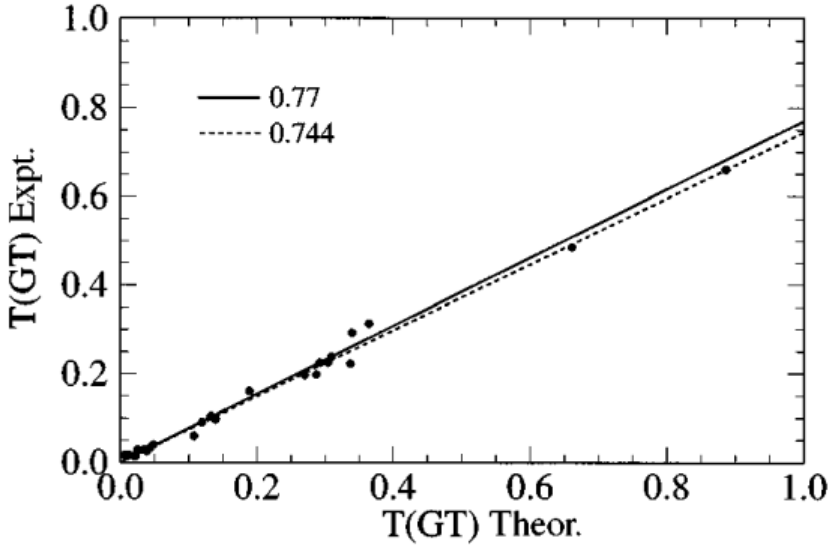

FIGURE 2.3: Comparison of the experimental values of the sums $T(\mathrm{GT})$, weighted squared root of scaled $B(\mathrm{GT})$, with the corresponding theoretical value based on the ''free nucleon'' Gamow-Teller operator from [50]. The solid line represents the fit in *sd* shell [52] while the dashed line in *pf* shell.

Theorists attribute g_A quenching to two possible sources: nuclear many-body correlations that escape calculations [53, 54, 55, 56] and many-nucleon weak currents [53, 57]. The former include short-range correlations, multi-phonon states, particle-hole excitations outside shell-model configuration spaces, etc. The latter represent non-nucleonic degrees of freedom, such as Δ-isobar excitations, in-medium modification of pion physics, partial restoration of chiral symmetry, etc. The consequences for $0\nu\beta\beta$ decay depend on which of these two complementary sources is mostly responsible for the renormalization of the $\mathcal{O}_{\mathrm{GT}}$ operator [48]. Theorists have not formed a conclusive argument when they tried to use many-body perturbation theory [58] to

quantify the effect of missing correlations on the $\mathcal{O}_{\mathrm{GT}}$ operator in the shell model. Siiskonen et al. [59] reported a 20% to 60% reduction of the Gamow–Teller strength for nuclei whose valence nucleons are in the sd and pf shells, depending on their atomic mass. However, Holt and Engel [60] studied $\beta\beta$ decay within a similar perturbative framework and reported a 20% enhancement of the $0\nu\beta\beta$ matrix element in ^{76}Ge and a 30% enhancement in ^{82}Se. When investigating the second source, theorists did not disagree as much. Menéndez et al. [61] applied many-nucleon currents to the single-β and $\beta\beta$ decay of medium mass nuclei and reported a 30% corresponding reduction of $0\nu\beta\beta$ decay matrix elements. In 2014, Ekström, Andreas et al. [62] included two-nucleon currents in coupled cluster calculations of single-β decay. They found a 10% reduction of the $\mathcal{O}_{\mathrm{GT}}$ operator on carbon and oxygen isotopes, which suggests a very small quenching of $0\nu\beta\beta$ decay matrix elements. These studies show that if the former quenching source dominates, then the current estimate of $0\nu\beta\beta$ decay matrix elements would be significantly too large. If the second source matters more, on the other hand, then the matrix elements would still be too large, but by a factor of less than 2. In 2017, Engel and Menéndez concluded that to determine which of the two contributions is more important and plumb the consequences for $0\nu\beta\beta$ decay, one would need calculations that treat many-body correlations in a comprehensive way and include many-nucleon currents consistently, which should be possible to achieve in the next five or so years [48].

Engel et al. [63] pointed out that the overall value of the charged-current cross section on ^{127}I, as well as the transition to specific nuclear states in ^{127}Xe, depend on the value of g_A, and thus it may be possible to study the quenching of g_A through charged-current interaction. Since the momentum transfer in charged-current transitions is around the energy of the neutrino, this way one could learn about the quenching of g_A through a weak-process at momentum transfers on the order of 10s of MeV. Table 2.2 demonstrates the impact of g_A quenching on the total charged-

current interaction cross section, and its transitions to specific nuclear states.

Table 2.2: Contributions of individual multipoles to the total cross section for neutrinos from muon decay, in units of 10^{-40} cm^2 from Engel et al.[63]. The two columns correspond to quenched and free values for g_A, respectively.

J^π	$g_A = -1.0$	$g_A = -1.26$
0^+	0.096	0.096
0^-	0.00001	0.00002
1^+	1.017	1.528
1^-	0.006	0.008
2^+	0.155	0.213
2^-	0.693	1.055
3^+	0.149	0.171
3^-	0.017	0.025
Total	2.098	3.096

2.4.2 Solar and Supernova Neutrino Detection

Noting Bahcall and Davis's success at solar neutrino counting in 1976 [12], in 1988 Haxton proposed using similar technology to study neutrino charged-current interaction on ^{127}I [49] for several reasons. First as discussed in earlier sections, the effective threshold of this reaction is about 789 keV, which is below the ^{37}Cl threshold of 814 keV. Second the cross section is expected to be significantly larger due the Gamow-Teller resonance in ^{127}I, which would also improve the sensitivity of the detector to supernova neutrinos [49]. Third, the ratio of the ^{7}Be/^{8}B cross section on ^{127}I is different from that on ^{37}Cl, so this iodine-based detector would help determine the relative ratio of solar neutrinos from the two different processes. Last but not least, the produced ^{127}Xe has a half-life of 36.4 days, which is long enough for a radiochemical approach.

As shown in figure 2.4, the reaction threshold if allowing forbidden transitions makes it possible to detect ^{7}Be, CNO, *pep*, *pp* and *hep* solar neutrinos. In addition, the ratio of the single neutron emission state to the zero neutron emission state,

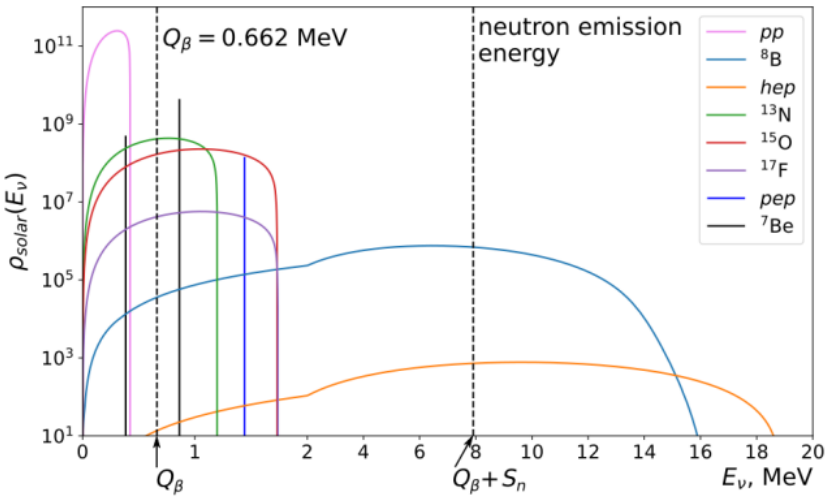

FIGURE 2.4: The solar neutrino spectrum according to the BS05(OP) model [64], along with two thresholds for the charged-current interaction on ^{127}I: one for the forbidden transition state and one for the single neutron emission state, from reference [65].

^{126}Xe/^{127}Xe, produced by the charged-current interaction could potentially be used to study the fraction of low-energy to high-energy solar neutrinos [65].

2.4.3 Previous Measurement

In 2003, Distel et al. [1] published the result of the exclusive $^{127}\mathrm{I}(\nu_e, e^-)\,^{127}\mathrm{Xe}_{\mathrm{boundstates}}$ cross section measurement: $[2.84 \pm 0.91\ (\mathrm{stat}) \pm 0.25\ (\mathrm{syst})] \times 10^{-40}$ cm^2. The experiment, deployed in 1990, featured a tank containing 1540 kg of NaI solution. The tank/detector was placed 8.53 m from the Los Alamos Meson Physics Facility (LAMPF) beamstop, where it received a typical flux of 5×10^7 $\nu_e/(\mathrm{cm}^2\ \mathrm{s})$. The neutrino source was the decay of stopped muons.^{127}Xe atoms produced in the neutrino captures were extracted at several week intervals from the target solution and were placed in miniature proportional counters. Then the proportional counters were installed in a 20–30 cm thick Pb and Cu shield and placed inside a well of a NaI detector. All events from these counters were recorded, typically for a period of a year, to determine the number of ^{127}Xe atoms present. The unique decay signature of

^{127}Xe back to ^{127}I via electron capture, whose half-lfie is about 36.4 days, allows the decay process to be tagged by the resulting coincidence of Auger electrons followed by a 203 or a 375 keV de-excitation gamma. The counters detect the Auger electrons while the NaI crystals detect the de-excitation gammas.

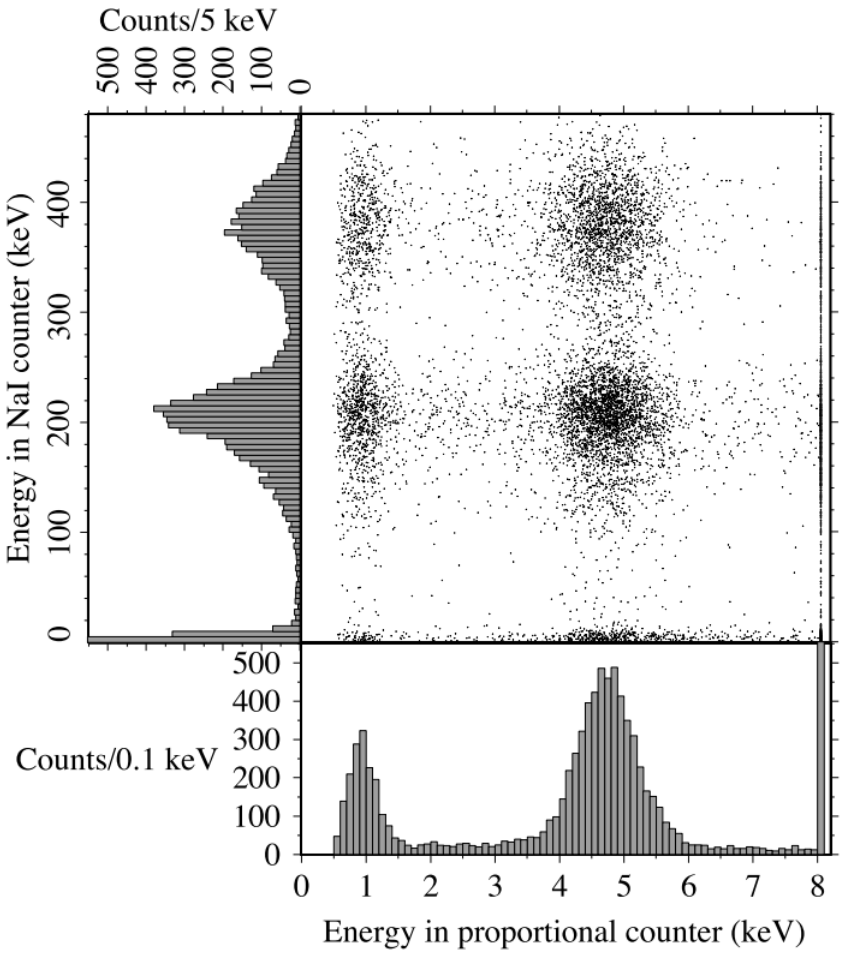

FIGURE 2.5: Measured Auger electron and nuclear gamma coincidence spectra from the decay of ^{127}Xe in a proportional counter inside the well of a NaI detector from reference [1].

The dominant background for this experiment at LAMPF was the ^{127}Xe produced by the $^{127}\mathrm{I}(p,n)^{127}\mathrm{Xe}$ reaction, which can be initiated by [1, 38]:

- Cosmic muons causing photonuclear evaporation of a proton from ^{127}I.

- Neutrons from local sources undergoing (n, p) reaction in the water to produce protons.

- Energetic alpha particles from unstable nuclei decays in the target, such as uranium and thorium, transferring energy to the proton through (α, p) scattering.

Notably,these backgrounds would not be relevant if one is to measure the inclusive cross section instead of only counting $^{127}\mathrm{Xe}_{\mathrm{boundstates}}$. The rather large statistical and systematic error could also be reduced with a more precise measurement. Additionally, it would be interesting to measure the energy dependence of the inclusive cross section using a NaI detector, as noted by Distel et al. [1] in their publication of the LAMPF result.

3

The NaI[Tl] Neutrino Experiment (NaIνE)

3.1 The Spallation Neutron Source

The Spallation Neutron Source (SNS) at the Oak Ridge National Laboratory (ORNL) uses a superconducting linear accelerator to produce the most intense beams of pulsed neutrons in the world for scientific research and industrial development across different fields [66].As shown in figure 3.1, after recent upgrades, a 60 Hz pulsed 1.4 MW beam of about 1 GeV protons strikes a mercury target. This process is equivalent to a delivery of 1,016 protons on target (POT) per second at 1.4 MW, which produces 20 to 30 neutrons per proton-mercury collision [67]. The pulsed beam allows better steady-state background rejection. Along with the neutrons, three different flavors of neutrinos are also produced after a short delay. Most of the π^+ from the spallation would be stopped and decay at rest with a lifetime of 26 ns into μ^+ and ν_μ, while 99% of the π^- are captured within the mercury target. The majority of the μ^+ also would be stopped and decay at rest with a lifetime of 2.2 μs into $\bar{\nu}_\mu$, ν_e and e^+. The remaining 1% π^- could go through a similar decay process and produce $\bar{\nu}_e$ but the probability would be too low.

The COHERENT collaboration, using a Geant4 simulation, calculated a total luminosity of 2.36 $\times$ 10^{15} neutrinos produced per second for an incident of 1 GeV proton beam at the SNS [68]. This is equivalent to about 4.25 $\times$ 10^{22} neutrinos per year, assuming a typical SNS operations of 7.0 GWhr/yr. The energy spectra and timing distributions of the neutrinos are shown in figure 3.2.

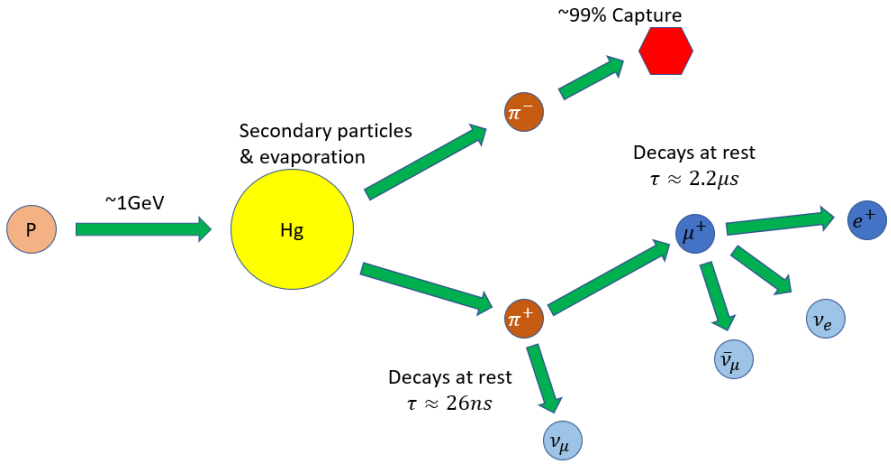

FIGURE 3.1: Illustration of neutrino production at the SNS.

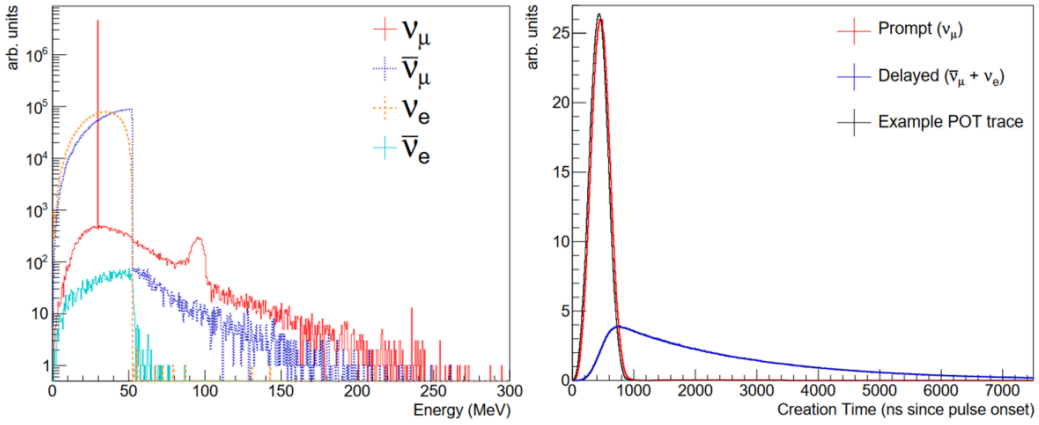

FIGURE 3.2: SNS neutrino energy spectra(left) and creation time distributions (right) predicted by the Geant4 simulation in reference [68]. This figure is from reference [67], which is a reproduction of the figure from reference [68].

3.2 The COHERENT Experiment

The COHERENT collaboration has deployed multiple detectors to Neutrino Alley at the SNS to study Coherent Neutrino Nucleus Scattering (CEνNS), neutrino inelastic interactions, dark matter and other important neutrino related interactions. The COHERENT collaboration is also deploying more detectors deployed in the near future, as shown in both table 3.1 and 3.2. These detectors are roughly 19 to 29 meters away from the mercury target, as indicated in figure 3.3 and table 3.1. In Neutrino Alley, the detectors are exposed to an ample amount of neutrinos, with excellent background rejection. The simulations performed by the COHERENT collaboration [69] predict a flux of 4.7×10^7 neutrinos/(cm^2 s), with a 1 GeV proton beam, 20 m away from the mercury target [67]. The concrete fill within the wall helps suppresses the beam related neutrons and the 8-meter-water-equivalent overburden at the top helps reduce cosmic backgrounds.

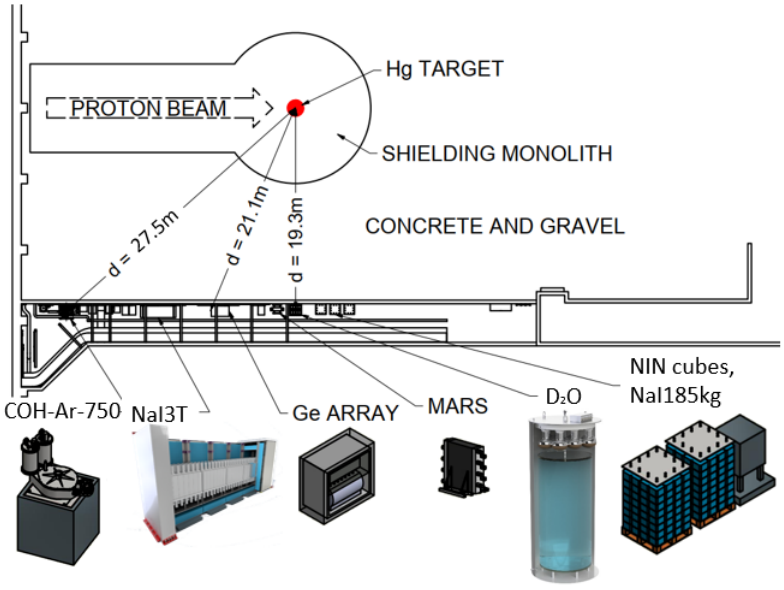

FIGURE 3.3: The layout of current and near-future detector subsystems in Neutrino Alley, courtesy of Dr. Rex Tayloe.

Table 3.1: Parameters of subsystems for CEvNS detection from reference [67].

Target	Technology	Mass (kg)	Distance (m)	E_{th} (keV_{nr})	Date
CsI[Na]	Scintillating crystal	14.6	20	5	2015-19
Ar	Single-phase LAr	24	29	20	2016-21
Ge	HPGe PPC	18	22	<5	2022
NaI[Tl]	Scintillating crystal	3500	18.74	13	2022
Ar	Single-phase LAr	750	29	20	2025
Ge	HPGe PPC	50	22	<5	2025
CsI	CsI+SiPM arrays at 40K	10-15	20	1.4	2025

Table 3.2: Description of additional detectors that broaden the physics reach of COHERENT from reference [67].

Name	Technology	Purpose	Date
NaIvE	185 kg NaI[Tl] crystals	Measure ν_e+I CC cross section & beam-related backgrounds	2016-present
MARS	Scintillation panels interleafed with Gd-painted foils	Measure beam-related neutrons in Neutrino Alley	2017-present
NIN cubes	Liquid scintillator cells in lead and iron shields	Measure neutrino-induced neutrons (NIN) in lead & iron	2015-present
D_2O	Heavy water Cherenkov detector	Measure neutrino flux precisely & ν_e+O inelastic cross section	2022
LAr	Liquid argon TPC	Measure ν_e+Ar inelastic cross section	2025

3.3 NaIνE-185 Detector Design

3.3.1 Overview

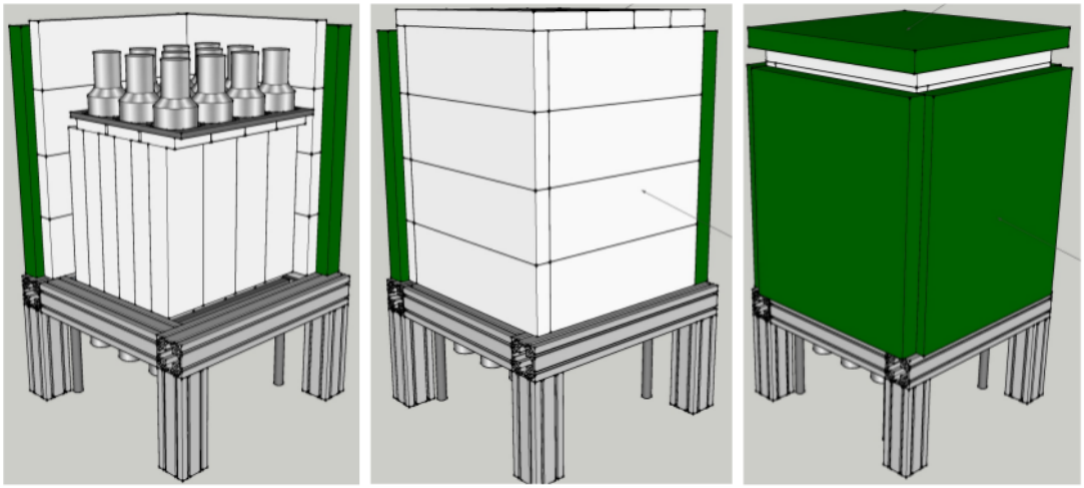

FIGURE 3.4: The schematic of NaIνE-185 after shielding upgrades, courtesy of Dr. Sam Hedges. The green panels are muon vetoes and the white panels are steel shielding.

The detector of interest in this work is the 185-kg NaI prototype detector called NaIνE-185. Its main purpose is to measure the inclusive cross section of electron neutrino charged-current interaction on ^{127}I. It also helps measure the in-situ backgrounds at the SNS for the ton scale NaI detector deployed during the summer of 2022, whose details are included in reference [38]. The early testing, deployment of NaIνE 185 were mainly done by Ben Suh [70] and Dr. Sam Hedges. The detector contains 24 NaI modules, each of which contains a 7.7-kg NaI[Tl] scintillating crystal and a 10-stage 3.5" diameter Burle S83013 PMT (or equivalent) [38]. The bases of the PMTs only have a high gain mode, which results in a threshold of 1 MeV. The detector was deployed with two different shielding conditions: water bricks only and muon veto + steel shielding. The studies of this work uses only the data taken with the later shielding configuration due to concerns about backgrounds.

3.3.2 Backgrounds

The backgrounds for the measurement of the inclusive cross section of electron neutrino charged-current interaction on ^{127}I using NaIνE 185 include:

- Steady-state cosmic muons: these muons generate signals in the NaI crystals resembling electrons from the charged-current interaction. They are the most dominant backgrounds.

- Beam Related Neutrons (BRN): these neutrons share the timing information with the prompt neutrinos and could directly trigger the detector or interact through secondary reactions in the shielding.

- 511 keV annihilation gammas caused by the positrons from the Hot Off-Gas Pipe[1]: these are present along with the beam and could persist for hours after beam is off.

- $^{23}\mathrm{Na}(\nu_e, e^-)^{23}\mathrm{Mg}$: the produced electrons generate indistinguishable signals from those resulted from $^{127}\mathrm{I}(\nu_e, e^-)^{127}\mathrm{Xe}$. Decay products of ^{23}Mg also produce similar signals at a later time.

- $^{56}\mathrm{Fe}(\nu_e, e^-)^{56}\mathrm{Co}$ from the steel shielding: the produced electrons and other de-excitation products generate indistinguishable signals from those resulted from $^{127}\mathrm{I}(\nu_e, e^-)^{127}\mathrm{Xe}$.

- $^{27}\mathrm{Al}(\nu_e, e^-)^{27}\mathrm{Si}$ from the aluminum housing of the NaI[Tl] crystals: the produced electrons and other de-excitation products generate indistinguishable signals from those resulted from $^{127}\mathrm{I}(\nu_e, e^-)^{127}\mathrm{Xe}$. However, the mass of the aluminum housing is much smaller than that of either the shielding or the

[1] The Hot Off-Gas Pipe is a pipe that runs through neutrino alley. It carries away radioactive gasses produced during beam operations.

crystals and the cross section is on par with $^{23}\mathrm{Na}(\nu_e, e^-)^{23}\mathrm{Mg}$. As a result, it is negligible for this work.

- Neutral-current neutrino-nucleus scattering: neutral-current interactions can produce indistinguishable signals but the energies are below 10 MeV from MARLEY predictions.

- Elastic-neutrino electron scattering off electron: these scattered electrons are only expected to contribute about 1.2% to the expected number of electron signals. As a result, they are not modeled in this work.

The water bricks in the phase one deployment were able to shield some of the BRNs but not steady-state muons. Using outer detectors as muon vetoes would result in a much lower sensitivity so the shielding was subsequently upgraded. The detector was first surrounded on four sides and on the top by 1.5" thick steel plates, which stops electrons produced by charged-current interactions from triggering the muon vetoes. Then the plates and the detector were surrounded by four 25 5/8" × 22"×2" plastic scintillators, called muon veotoes, on the sides and a 23" × 23"×2" panel on the top. These plastic scintillators are covered by reflective mylar first and then black plastic sheets. The corners and edges are sealed by light-tight tape and black silicone. There are two ET-9078B PMTs on each of the four side panels and four on the top panel. These muon vetoes plus the 8-meter water equivalent overburden on the top help remove the majority of the steady-state muons. The remaining four backgrounds are mostly addressed through data processing and Probability Density (PDF) fitting. Because we use cuts in the MeV range, the 511 keV gammas can be neglected.

Table 3.3: Expected number of events in the 10-55 MeV and 10-μs analysis window for both the signal and backgrounds along with their nominal cross sections if applicable. The numbers have efficiencies incorporated in them. Details of uncertainties and efficiencies of the counts can be found in chapter 7.

Name	Cross section ($\times 10^{-40}$cm^2)	Expected Counts	Source
$^{127}\mathrm{I}(\nu_e, e^-)^{127}\mathrm{Xe}$	22.49	1,320	MARLEY, B(GT) from [71]
$^{23}\mathrm{Na}(\nu_e, e^-)^{23}\mathrm{Mg}$	0.496785	31	MARLEY, B(GT) from [72]
$^{56}\mathrm{Fe}(\nu_e, e^-)^{56}\mathrm{Co}$	2.85834	31	MARLEY, B(GT) from [73, 74]
Muon	n/a	10,960	Data
BRN	n/a	3,939	Floating in the fit

3.3.3 Signal and Backgrounds Predictions

The predictions of charged-current interaction are based on a software package called MARLEY [41], which will be discussed in the simulation chapter. The predictions of muon counts come directly from the data, with a 10-μs region-of-interest window applied. All the expected counts are calculated with a beam exposure of 22.8 GWhr, from all available data passing the health checks.

3.3.4 Data Acquisition Systems

As described in reference [38], the NaI PMTs have a gain dependent operating voltage range between 780 V and 1000 V. They are powered by a CAEN A7030P 48-channel high voltage card while the muon veto PMTs are powered by a CAEN A7030N card. A CAEN SY4527 high voltage main frame holds both cards. Five Struck SIS3302 8-channel 100-MHz 16-bit digitizers were used to, with their built-in triggers, record:

- Signals from 24 NaI channels and all 12 PMTs on the muon vetoes.
- A 60 Hz signal called event 39 from the SNS, which synchronizes the extraction kicker magnets and the neutron choppers.

- Event 61 from the SNS, triggered by the beam-on condition, when protons are directed to the target.

Due to data storage limits and concern about event rates, the charge integration is recorded, as opposed to the full waveform for each event, which is shown in figure 3.5. For NaI channels, eight 1250-ns-long accumulator bins are saved in this process. The first two (2500 ns) are used used to calculate the baseline. The integral of the next three bins (3750 ns), subtracting the baseline, is used to define the energy deposition of an event in ADC unit. Additionally, the maximum height, the timing and a pile-up check flag of pulses are also recorded. The muon veto channels, however, only record 750-ns-long waveforms, with the pulse occurring roughly 100 ns into the event [38].

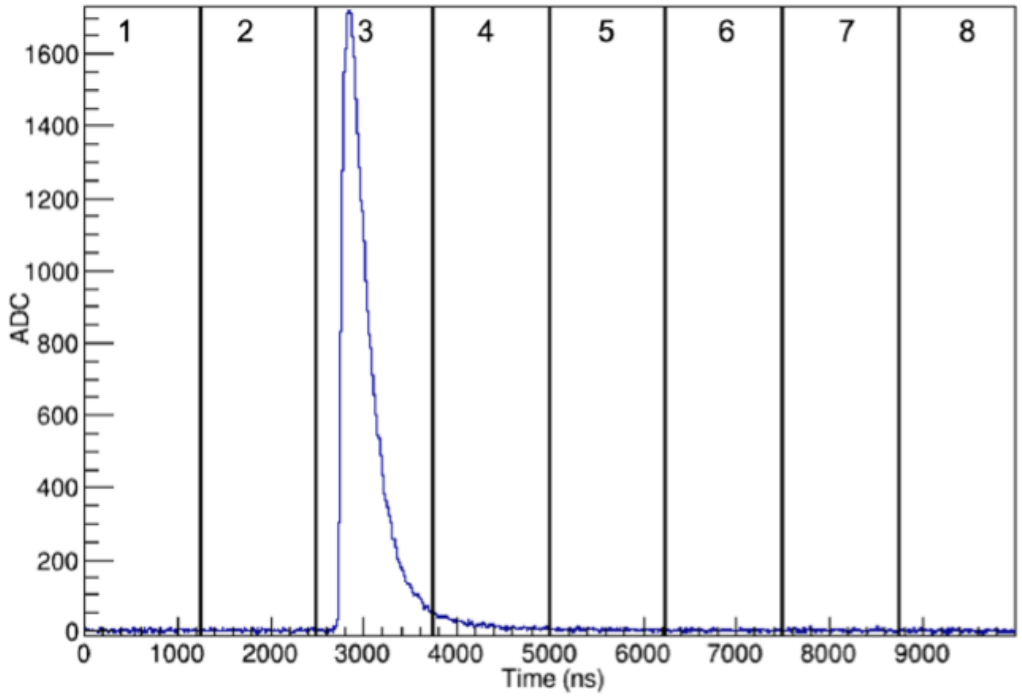

FIGURE 3.5: Waveform sample of NaIνE-185, courtesy of Dr. Sam Hedges [38]. The numbers on the top of each block represents the accumulator number.

3.4 Data Processing

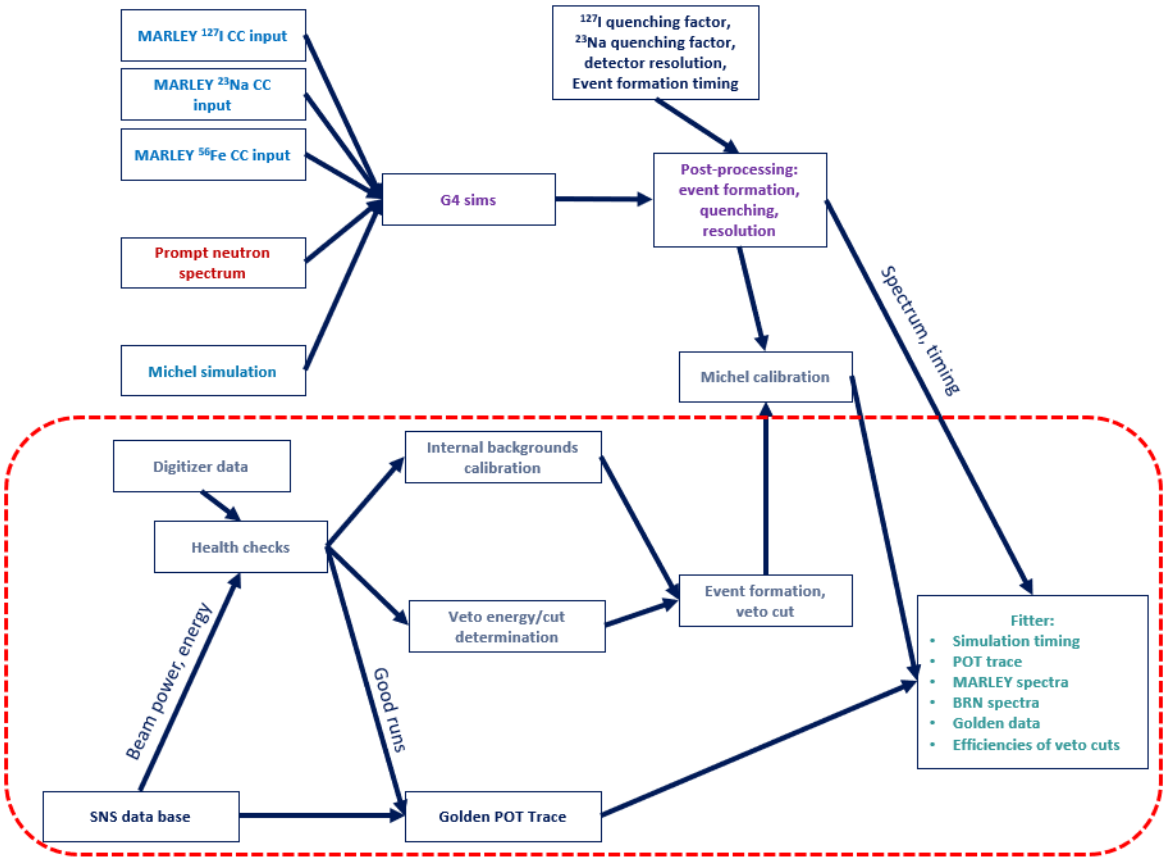

FIGURE 3.6: The flow chart of the NaIνE-185 analysis, courtesy of Dr. Sam Hedges. The tasks included in the red box were done by Dr. Sam Hedges, while the rest by Peibo An.

As shown in figure 3.6, the NaIνE-185 analysis contains two major tasks: PDF construction through simulations by this author and detector data processing performed by Dr. Sam Hedges. The former will be covered in later chapters while the later is the focus of this subsection.

3.4.1 Data Health Check

The output of digitizers are formatted into four ROOT trees based on the source: the NaI tree, the veto tree, the SNS tree and the header tree. The data then go through

calibrations and a series of health checks, which then generate three different flags for each data file/run. Only data passing all three checks will be given the name *golden run* and used for the cross section measurement. About half of the runs passed all three tests. 94% of the discarded runs are simply beam-off runs. NaI channel 14 is also disabled and treated as a passive volume due to its poor resolution and high noise. The first flag called snsStatus checks the status of the beam at the SNS and is set to 1 if all the below conditions are met:

- The beam power $\geq$ 800 kW.
- The beam energy $\geq$ 950 MeV.

The second flag called runStatus checks the health of the run and is set to 1 if all the below conditions are met:

- The run length $\geq$ 6 hours for enough statistics.
- The trigger rate of NaI channels $>$ 0 but $\leq$ 500 Hz for high frequency outlier removal.
- NaI channel baseline Root Mean Square $\leq$ 4 ADC for noisy run removal.
- The sum of muon veto trigger rate $>$ 0 for veto presence.

The last flag called calStatus checks the condition of the calibration and is set to 1 if none of the below conditions are met:

- A run cannot be calibrated due to either abundant presence of 511 keV gammas from the Hot Off-Gas Pipe or rapid gain changes.
- A run has high background rates. As shown in figure 3.7, the runs with order of magnitude larger background rates but lower than that of expected muon event rates would fail this check.

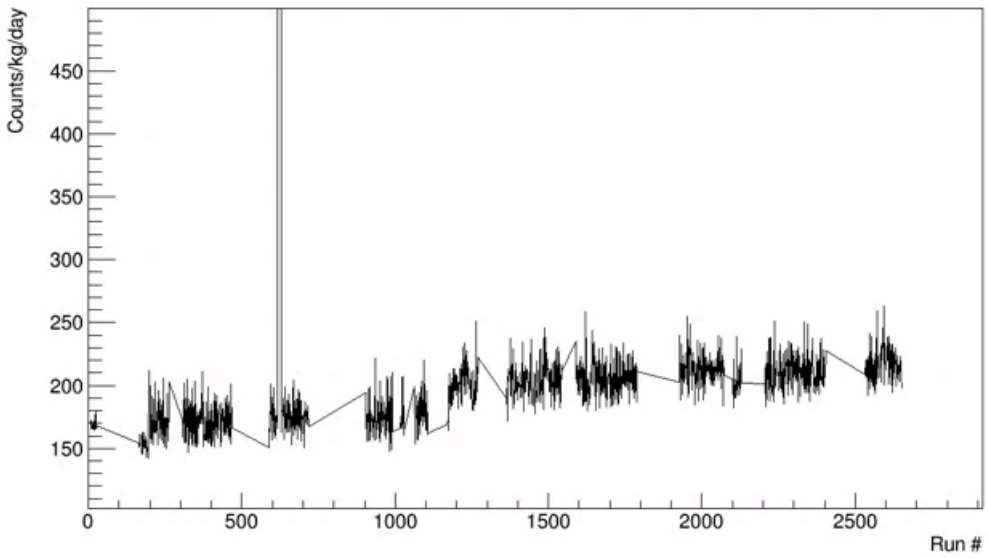

FIGURE 3.7: Background trigger rate of the blinded NaIνE-185 data between 10 and 55 MeV, courtesy of Dr. Sam Hedges.

3.4.2 Calibration

The calibration process happens after the first two health checks so that only data passing the first two checks would be used. It includes the following steps:

- The data is used to create energy spectra (in ADC units), in which pile-up and alpha events are removed for better calibration. Note that neither the pile-up nor alpha events were removed from the data.
- The 1460 keV ^{40}K and the 2615 keV ^{208}Tl peaks are located within the energy spectrum of each of the 24 NaI channels and a Gaussian + linear fit is applied.
- A two-parameter energy resolution function is used. The two parameters are then used in the simulations.

Alpha Identification

As shown in figure 3.8, the alphas are removed by a simple box cut because they have higher Amplitude/Energy (A/E) ratio than both the gamma backgrounds and

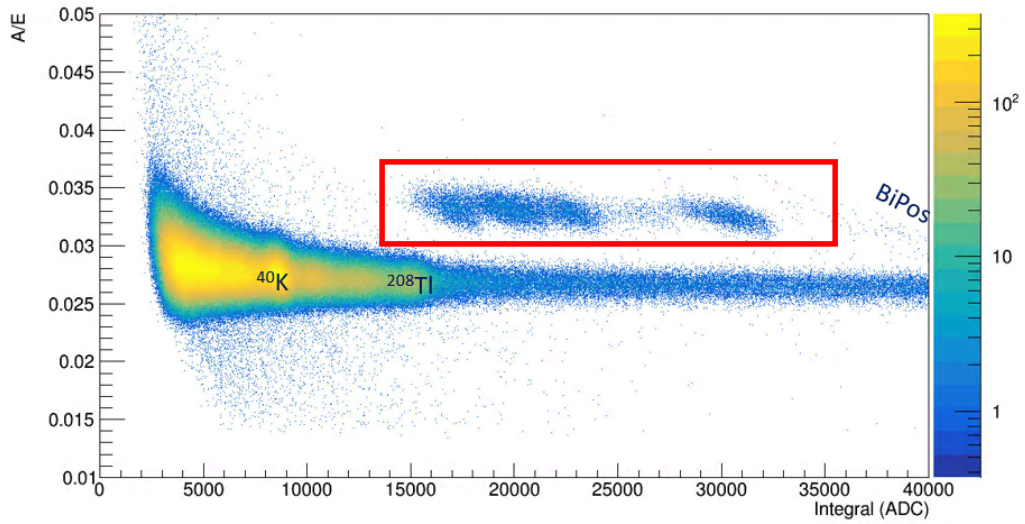

FIGURE 3.8: ADC integral vs. ADC peak height/integral, courtesy of Dr. Sam Hedges. Alphas appear with a higher A/E ratio than gamma backgrounds and the two intrinsic peaks and thus are removed with a box cut.

the two intrinsic peaks. Other higher energy backgrounds, like bismuth polonium decays, do not matter because they tend to be far away from the ^{208}Tl peak.

Fitting

As mentioned earlier, the ^{40}K and the ^{208}Tl peaks within the NaI crystals are used to convert the ADC units to keV. Linear backgrounds plus Gaussian are fitted around the two peaks. The fitting process starts with an autonomous sweeping fit for each channel and each run. Then these fit results are manually updated and corrected if necessary. The corrections are determined based on the fluctuation of the fitted means and sigmas over run numbers, illustrated by figure 3.10.

Unfortunately even after the calibrations there are still some discrepancies among individual detectors due to non-linearity from the NaI crystals [75], PMT bases and the digitizers. As shown in figure 3.11, the discrepancies mostly affect the > 20 MeV region, where the peak of $^{127}\mathrm{I}(\nu_e, e^-)^{127}\mathrm{Xe}$ sits. The approach to address this issue will be discussed in the high energy calibration chapter.

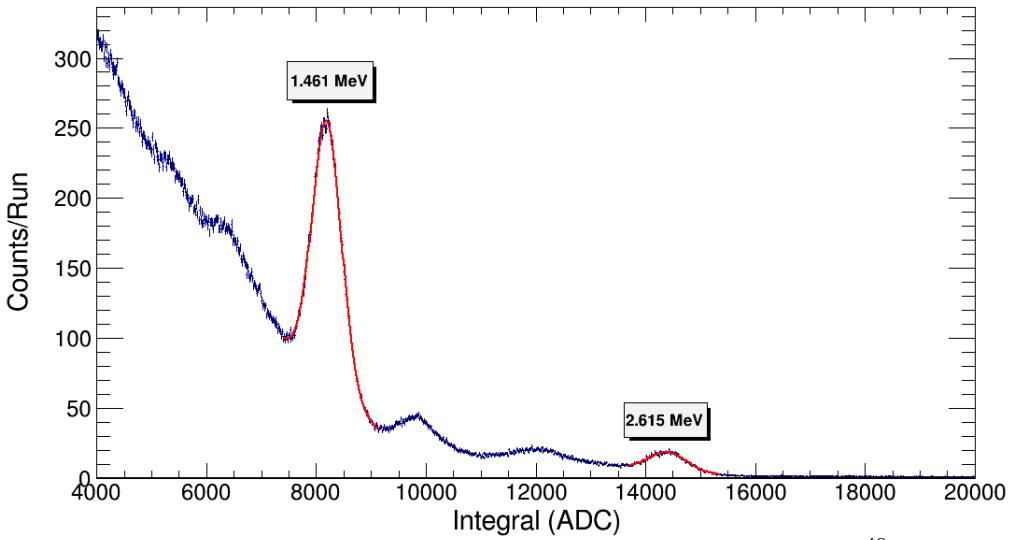

FIGURE 3.9: An example of good Gaussian + linear fits for the ^{40}K and the ^{208}Tl peak of a NaI channel, courtesy of Dr. Sam Hedges.

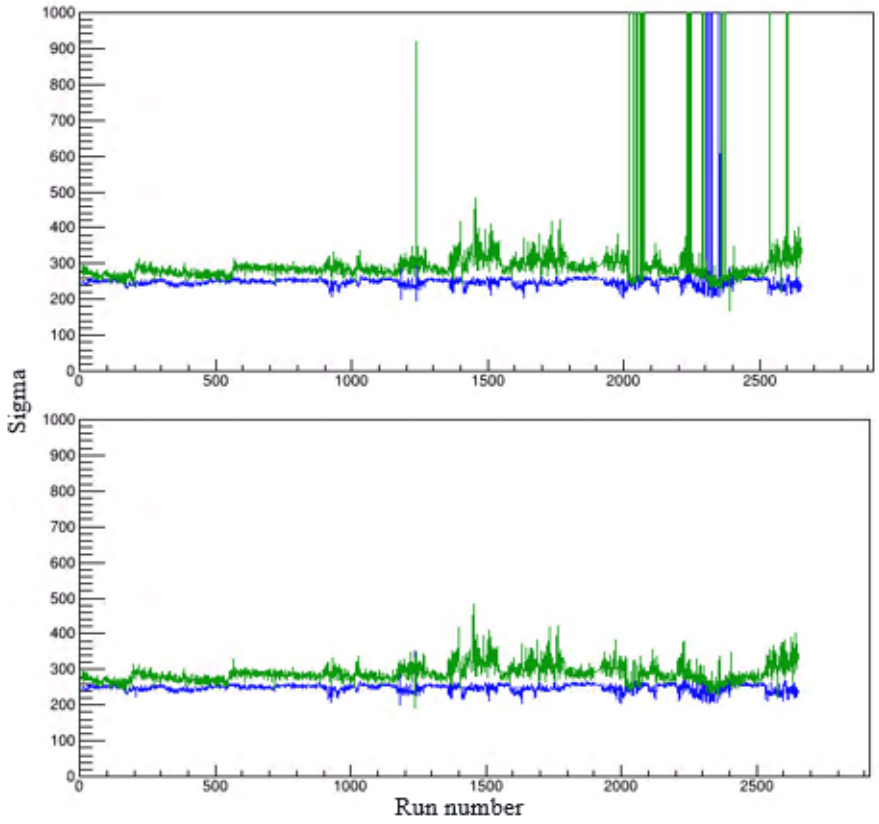

FIGURE 3.10: Top: fitted sigma values over run numbers before fit corrections; bottom: same chart after corrections. Both are courtesy of Dr. Sam Hedges.

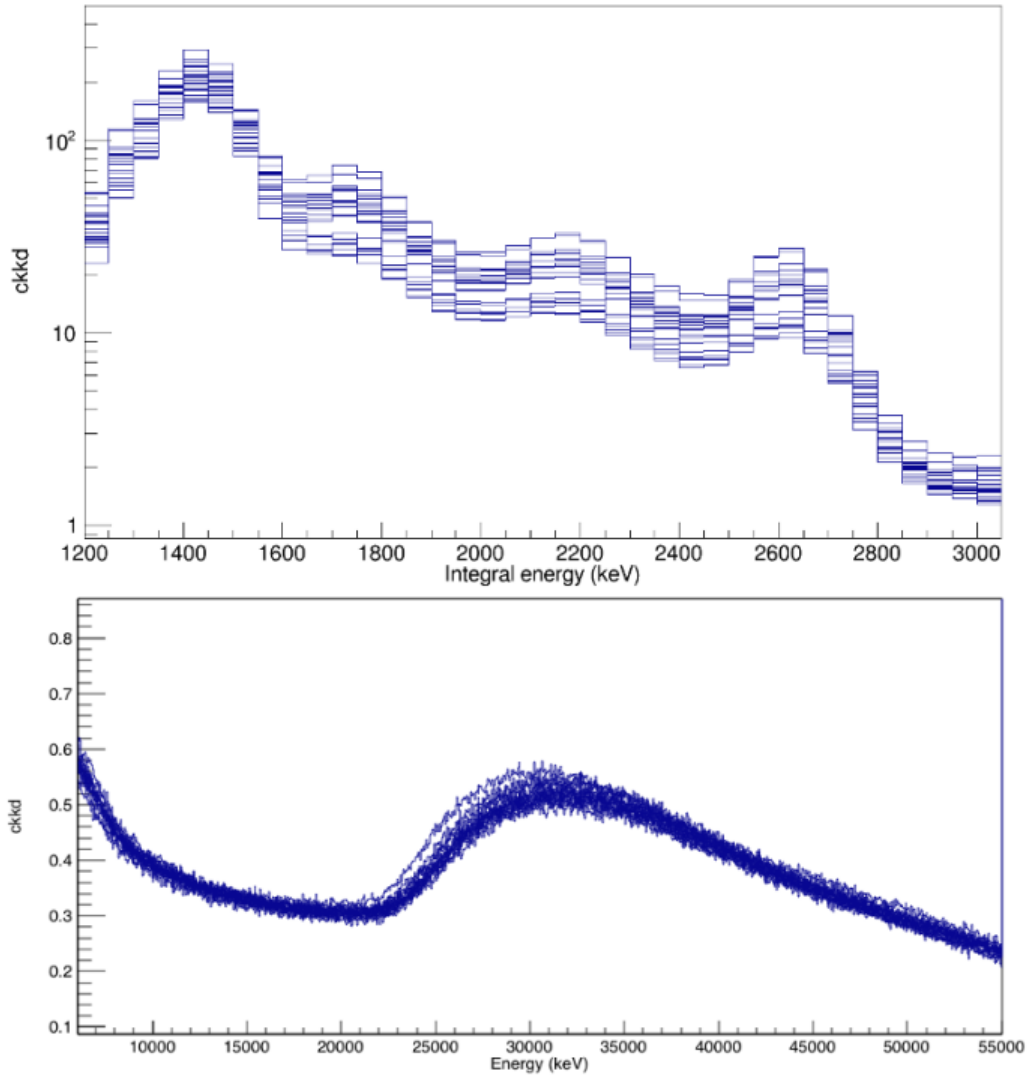

FIGURE 3.11: Calibrated internal background spectra in the 1.2 to 3 MeV region (top) and those in a broader energy ranges, courtesy of Dr. Sam Hedges [38]. The top chart shows excellent agreement while the bottom one shows disagreement at higher energies.

Energy Resolution

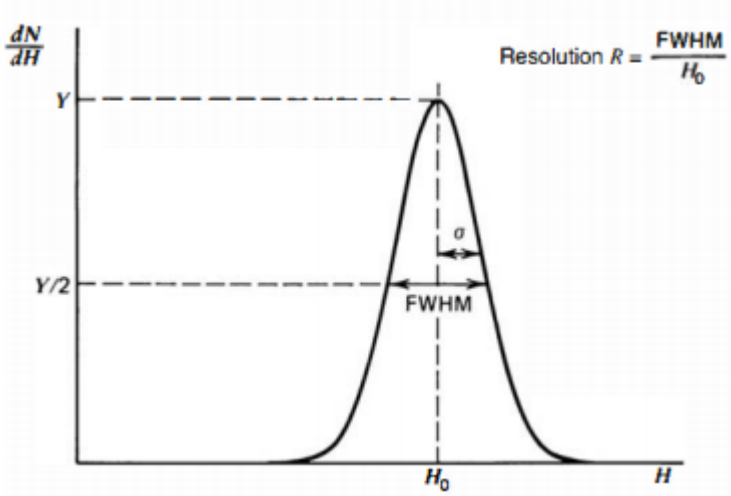

FIGURE 3.12: The definition of detector resolution from Knoll [76]. For peaks whose shape is Gaussian with standard deviation σ, the Full Width at Half Maximum (FWHM) is given by 2.35σ.

In many radiation detectors, the goal is to measure the energy distribution of the incident particle of interest. However, detector responses form a distribution for each event. As a result, a significant amount of fluctuations could be recorded from pulse to pulse even with the same energy deposited in the detector for each event. It is crucial to know the energy resolution R well, defined in figure 3.12, especially at keV level energies. A common NaI[Tl] 2-parameter formula of the standard deviation σ can be written as [77]:

$$\sigma = \frac{1}{2.355}(aE + b\sqrt{E}) \tag{3.1}$$

where a and b are fit parameters and E is the incident energy in keV. In the summer of 2018, Jesse Devaney, an REU student at TUNL, determined the energy resolution as a function of energy for some NaI[Tl] crystals using a variety of gamma sources that had peaks between 22 keV and 1460 keV [2]. He found that α is 0.023499 and β

[2] https://coherent.phy.duke.edu/wiki/NaI(Tl)_Energy_Resolution

is 1.20962. This does a good job describing the energy resolution as a function of energy to 500 keVee.

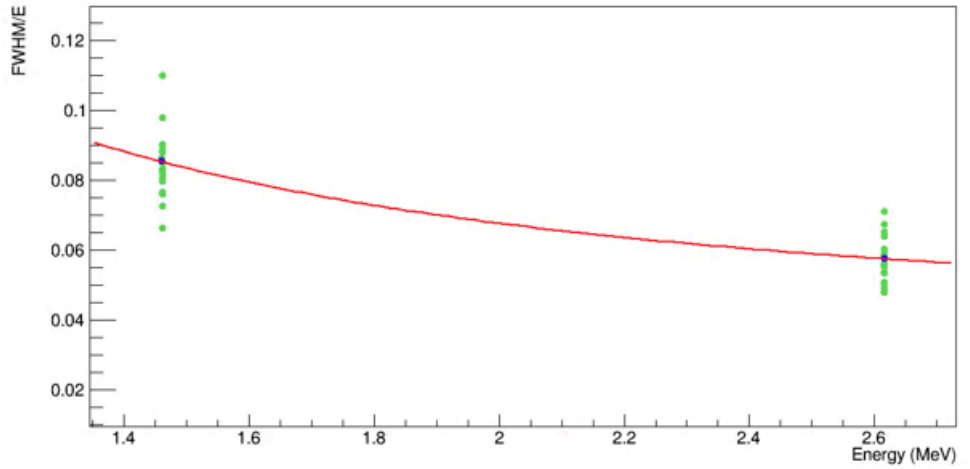

FIGURE 3.13: Fitted energy resolutions of each NaI channel (green) and the combined one (blue), courtesy of Dr. Sam Hedges.

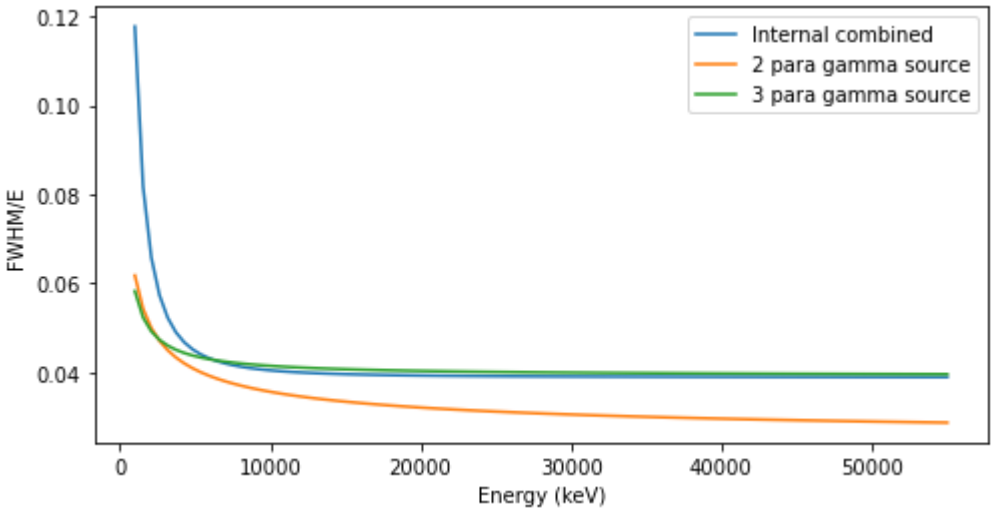

FIGURE 3.14: Comparison of three different energy resolution result over the same energy range. The internal combined label represents the one shown in figure 3.13.

To get a more accurate energy resolution, the calibration results of NaI channels

are used to fit a two-parameter function:

$$\sigma = \frac{1}{2.355}\sqrt{a^2 + b^2 E^2} \tag{3.2}$$

where $a = 0.11111 \pm 0.00002$ is a location-dependent term, $b = 0.03885 \pm 0.00002$ is the noise term and E is the incident energy in MeV. As shown in figure 3.13, each channel has its energy resolution fit. They are then combined using toy data sets into a unified energy resolution fit. Figure 3.14 shows the difference among three energy resolution results. The blue curve represents the unified energy resolution fit based on equation 3.2 and converges in the energy region of interest.

Muon Veto Event Building

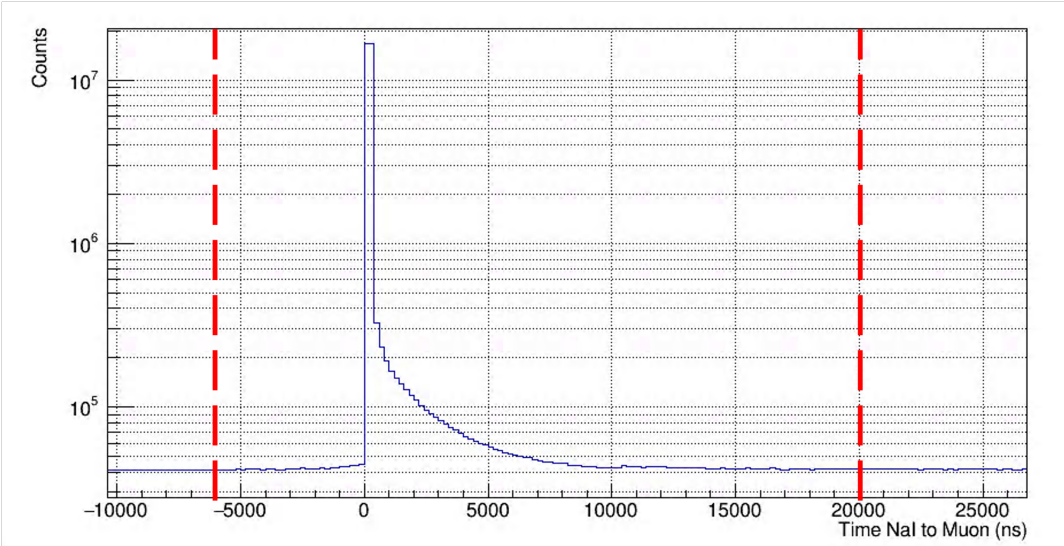

FIGURE 3.15: Timing window illustration of muon veto flags, courtesy of Dr. Sam Hedges.

The event building of muon vetoes depends on both energy and timing. Because muon vetoes see an excess of 511 keV gammas when the beam is on, a threshold is chosen such that 50% of the beam-on excess is rejected to address the concern of deadtime. This threshold is estimated to be between 300 keV and 700 keV. To

determine the muon veto flag, after the above threshold is applied, the time difference between the NaI event to the previous muon event is plotted in figure 3.15. The acceptable window is then defined as the region between -6 μs and 20 μs. Note that this window does not apply to Michel candidates, more details of which can be found in chapter 6. Figure 3.16 demonstrates the effectiveness of the muon veto flags. Figure 3.17 shows the efficiency of the vetoes on the blinded data in the energy region of interest.

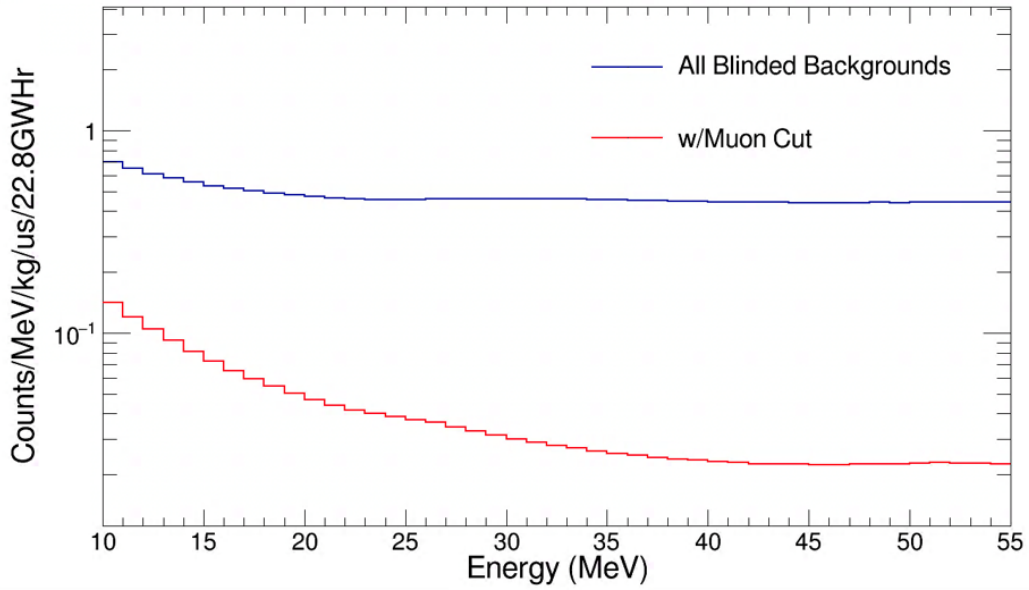

FIGURE 3.16: Energy spectra before and after muon veto cuts without beam-timing background rejections, courtesy of Dr. Sam Hedges.

NaI Event Building

After energy calibrations, integrated charges are grouped based on their timing information together to form events. A 400 ns coincidence window is chosen based on the PMT responses and cable lengths of the experiment setup. For each channel, there is also a 10 μs deadtime starting from charge integration, the implementation of which in the simulations can be found in chapter 4.

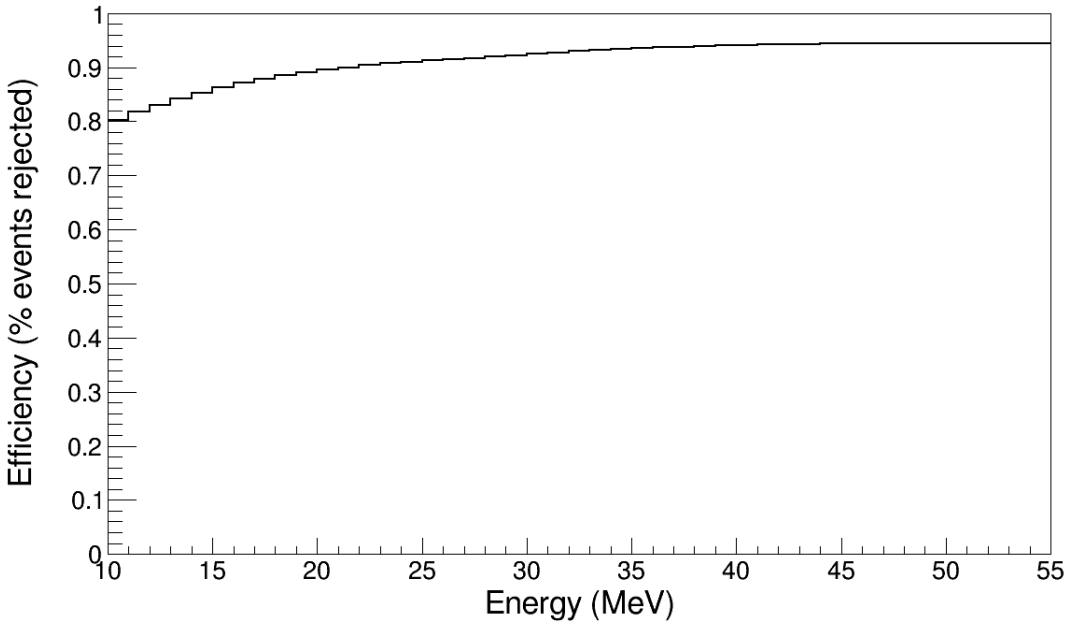

FIGURE 3.17: Percentage of events in the blinded data rejected by the muon veto in the energy region of interest, courtesy of Dr. Sam Hedges.

To deal with PMT saturation, the peak height vs integral plot is made as shown in figure 3.19, in which a 60 MeV saturation cut is chosen such that in the region below there exists a linear relationship between the peak height and the integral.

Finally to ensure the authenticity of the cross section measurement, the data are blinded before PDF fitting. To determine the timing window for blinding, muon veto timing to event 39 of high energy events with integrals above 10,000 ADC units is plotted, shown in figure 3.20. The center peak represents BRNs interacting with muon vetoes, which can be used as a proxy to the timing of neutrinos. Everything with a timing to event 39, defined in section 3.3.4, between -2 μs and 20 μs is blinded. This rather large window is chosen out of caution.

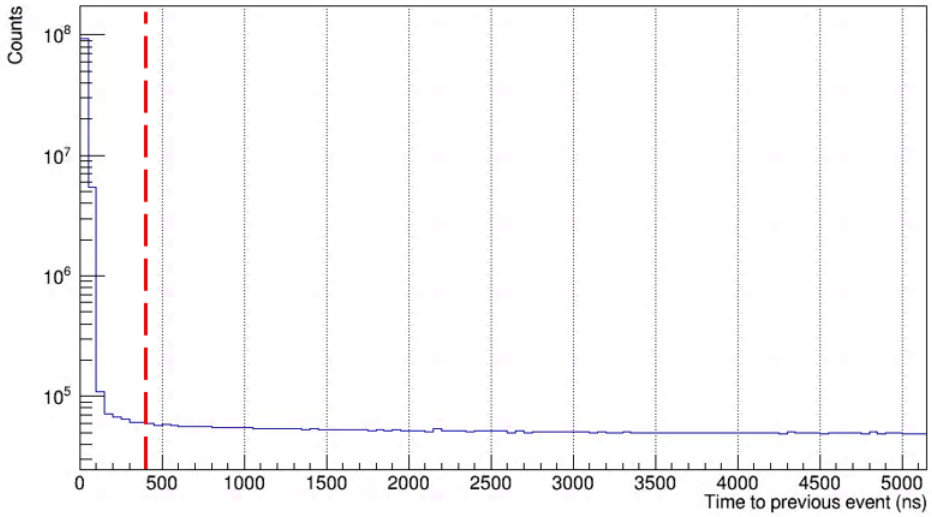

FIGURE 3.18: Illustration of NaI event grouping coincidence window, courtesy of Dr. Sam Hedges.

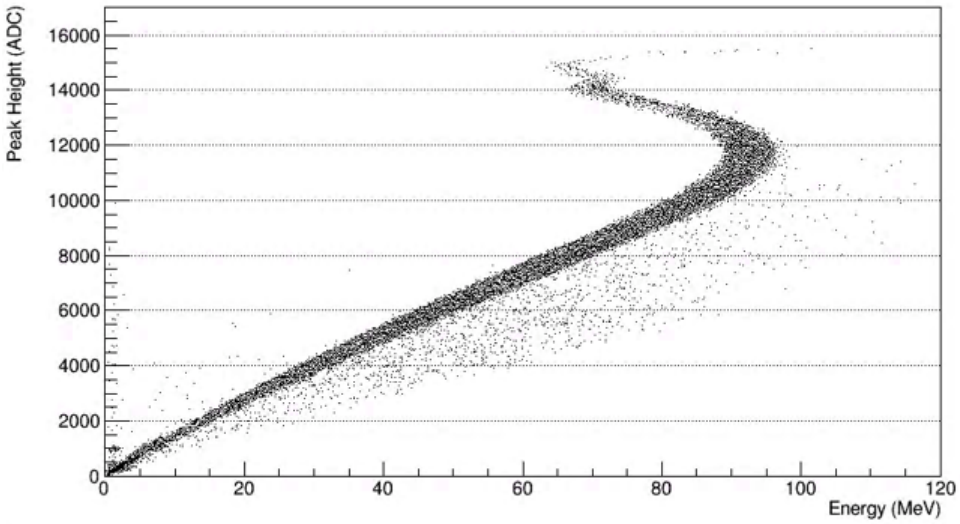

FIGURE 3.19: Illustration of NaI saturation using the peak height - integral plot, courtesy of Dr. Sam Hedges.

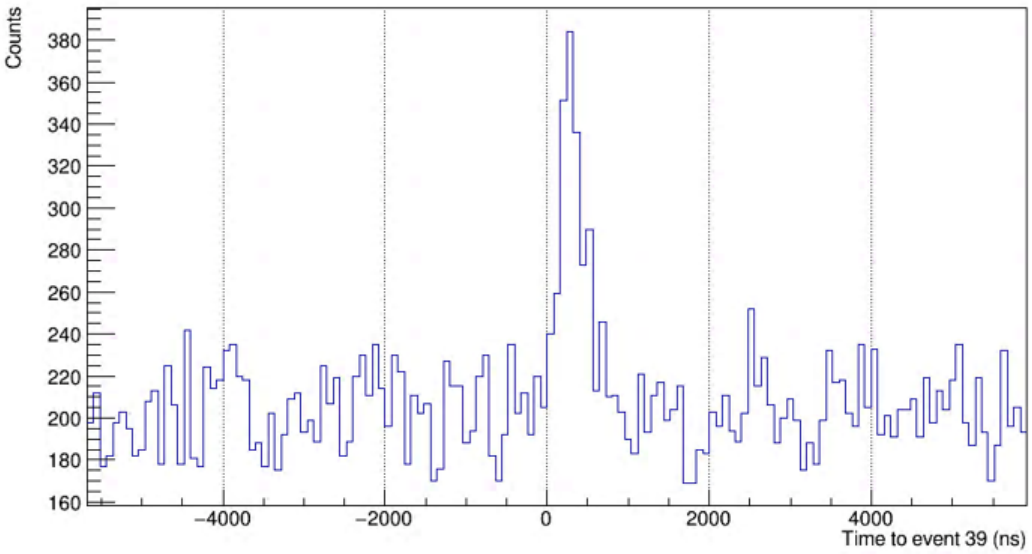

FIGURE 3.20: Muon veto timing to event 39, courtesy of Dr. Sam Hedges.

4

Simulations

4.1 Workflow

4.1.1 Overview

Five types of Geant4[1] simulations were performed to study the electron neutrino charged-current interaction on ^{127}I. These include beam related neutrons, cosmic muons and electron neutrino charged-current interaction on ^{127}I, ^{56}Fe and ^{23}Na. These simulations are important for several reasons:

- There exist only theoretical spectra of charged-current interaction on ^{127}I, ^{56}Fe and ^{23}Na and one cannot perform cross section analysis without these spectra.
- Simulations are more efficient than data gathering, especially in the case of beam related neutrons, and therefore can produce a large number of events for studies that require high statistics in a reasonable amount of time, like machine learning classifier development.
- Simulations can be used to study detector response. For example, in the case of the 185 kg prototype NaI[Tl] detector, simulations can give estimates of the

[1] https://geant4.web.cern.ch/

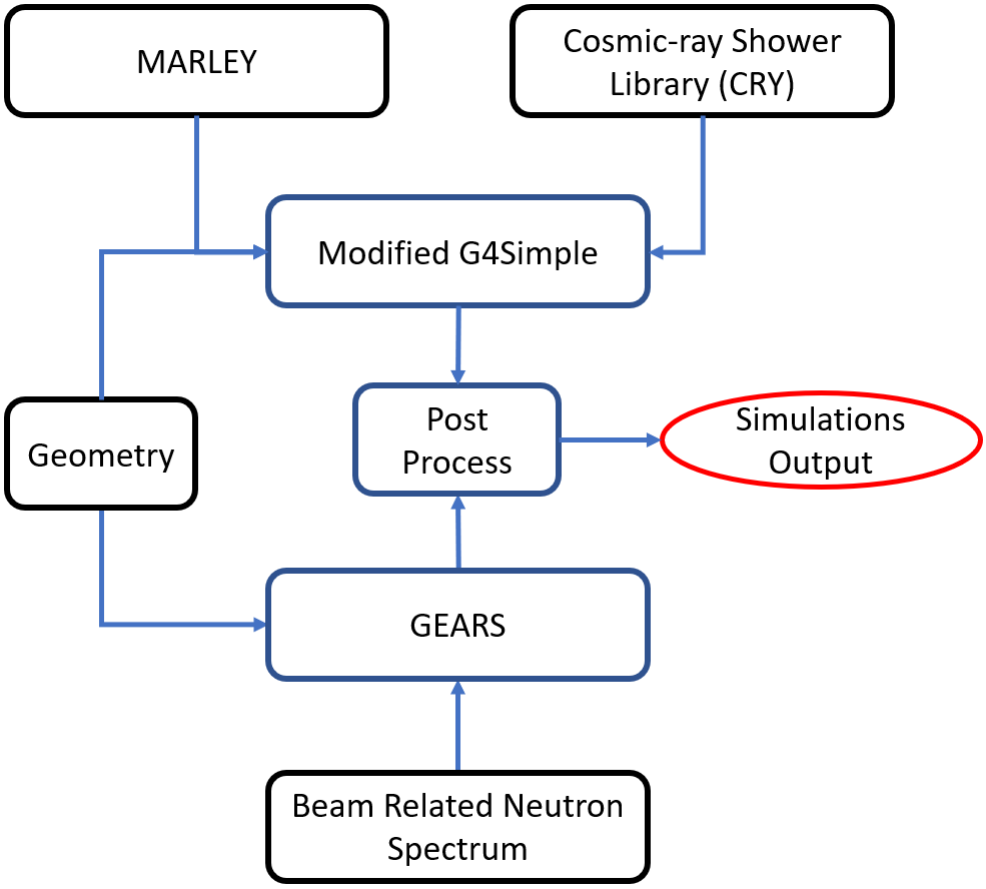

FIGURE 4.1: The flowchart of simulation productions for the 185 kg prototype detector.

portion of charged-current events that trigger the muon vetoes.

Figure 4.1 demonstrates the workflow of simulation productions. Two Geant4 based applications were used: modified G4Simple[2] by Dr. Daniel Salvat from Indiana University Bloomington and Dr. Jason Detwiler from University of Washington and GEARS[3] by Dr. Jing Liu from University of South Dakota. The major difference between the two is the user interface, as they both offer user defined features, like physics lists, detector geometry, particle input information, etc. Both applications

[2] https://code.ornl.gov/salvat/g4simple-naive

[3] https://github.com/jintonic/gears

require two major inputs: particle input and the geometry of interest. Simulations of beam related neutrons or Michel positrons have well studied spectra so they can be handled by GEARS, which takes input parameters like the spectrum, the particle name and initialization status and uses Geant4 to generate particles. However, for charged-current interactions, there are no simple spectra since they produce multiple types of particles. As a result, a Monte Carlo event generator, Model of Argon Reaction Low Energy Yields (MARLEY) [41] was used instead. The throws, particle information, generated by MARLEY were then passed on to Geant4 for interaction processes. Unlike the charged-current throws, cosmic muons were generated by Cosmic-ray Shower Library (CRY) [78] and were passed on to Geant4. Both applications use the same physics list: *shielding*, which is well suited for underground physics. After Geant4, the simulations were all post-processed by the same algorithm and made ready for analysis.

4.1.2 MARLEY

Model of Argon Reaction Low Energy Yields (MARLEY) is a Monte Carlo event generator originally developed to study the charged-current interaction on argon for the Deep Underground Neutrino Experiment (DUNE) by Dr. Steven Gardiner [41, 79]. As shown in figure 4.2, MARLEY offers multiple neutrino source and reaction options. The "2 2" scattering loop applies the formalism of charged-current/neutral-current interactions described in the Theory chapter in this work in the cross section calculation. As a result, forbidden transitions are not supported. Scattering products are then generated based on the calculated cross section and the supplied $B(\mathrm{GT})$ values via rejection sampling. The nuclear de-excitations are described by a combination of measured gamma ray decay schemes and the Hauser-Feshbach statistical model [79]. The final output contains multiple pieces of information, including but not limited to: particle identification number in the Monte Carlo particle numbering

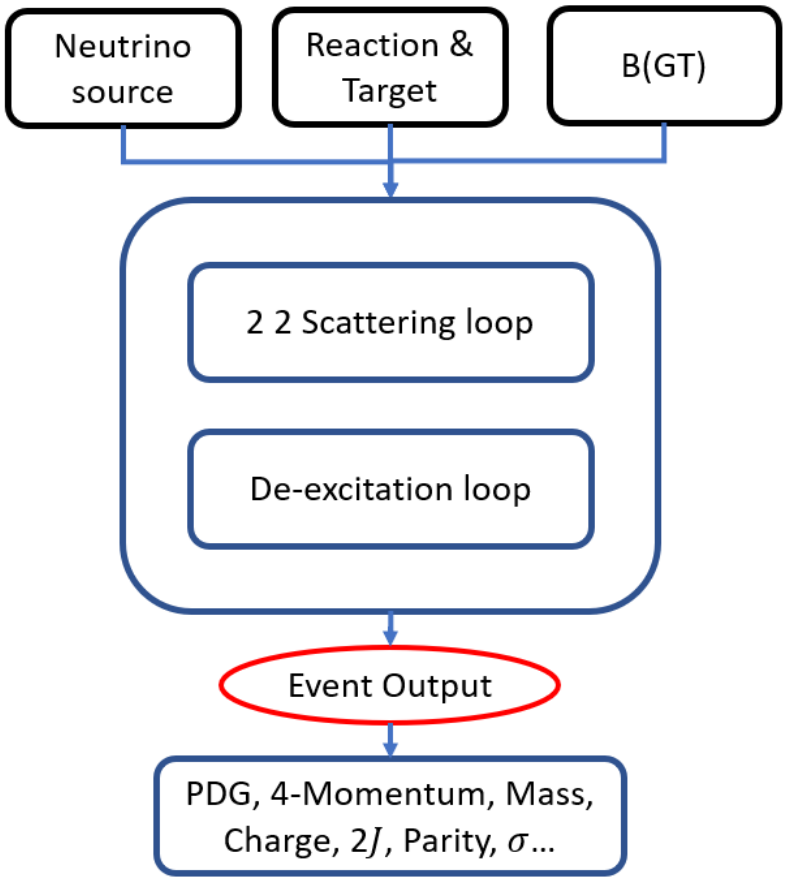

FIGURE 4.2: Simplified MARLEY workflow chart.

scheme [80], the four momentum, the inclusive cross section. These outputs can then be imported into Geant4, for example, to perform simulations.

The three types of charged-current simulations described in this work all used the same neutrino source: electron neutrinos from anti-muon decay-at-rest. More of the physics that is involved in muon decay is described in the High Energy Calibration chapter in this work. The electron neutrino source spectrum is approximated by:

$$\phi(E_\nu) = 96 E_\nu^2 m_\mu^{-4} (m_\mu - 2E_\nu) \qquad 0 < E_\nu < m_\mu/2 \tag{4.1}$$

where E_ν is the neutrino energy and m_μ is the muon rest mass. MARLEY then, by default, samples neutrino energies using the spectrum above weighted by the cross

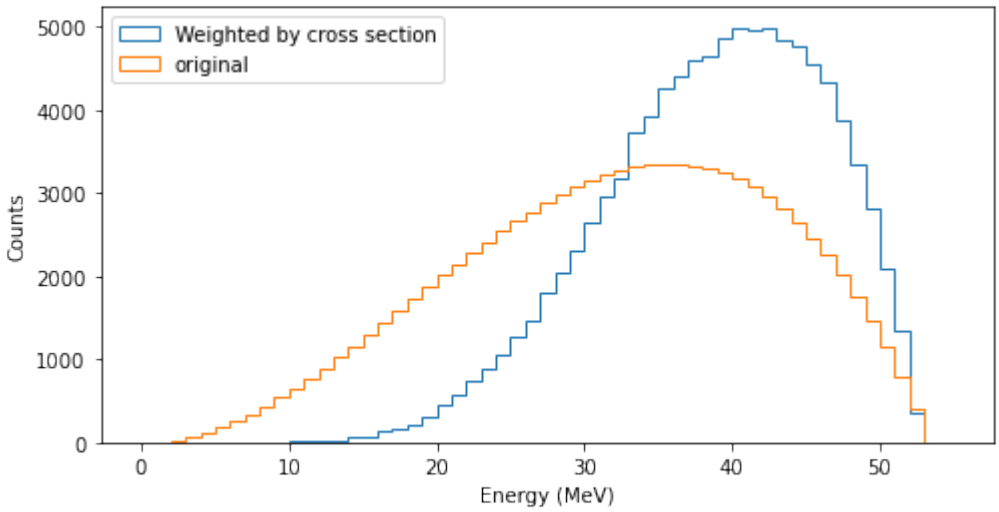

FIGURE 4.3: The weighted and original neutrino energy spectra.

section $\sigma(E_\nu)$. The energy PDF of the reacting neutrinos is then:

$$P(E_\nu) = \frac{\phi(E_\nu)\sigma(E_\nu)}{\int_{E_\nu^{min}}^{E_\nu^{max}} \phi(E_\nu)\sigma(E_\nu)dE_\nu} \tag{4.2}$$

Figure 4.3 shows the neutrino energy spectra before and after weighting. The remaining two inputs required for MARLEY, the target and B(GT) values, depend on the specific reaction.

4.1.3 Geometry

Table 4.1: Major components and materials in the geometry.

Part name	Material	Density (g/cm^3)	Sensitive
Sodium Iodine crystal	NaI	3.667	T
Steel plate shielding	G4_StainlessSteel	8	F
Hot Off-Gas pipe	G4_StainlessSteel	8	F
Muon veto	G4_Polystyrene	1.06	F
Overburden	G4_Water	1	F
Hallway	G4_Concrete	2.3	F
Crystal housing	G4_Al	2.699	F

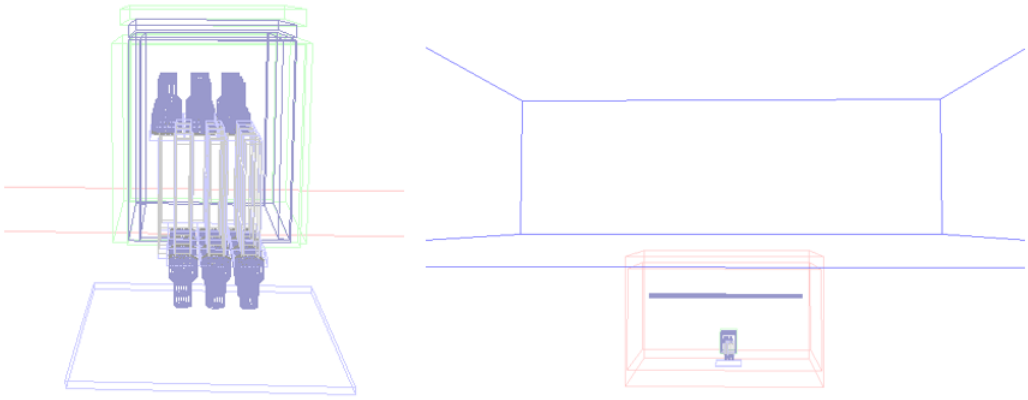

FIGURE 4.4: Left: the zoomed in view of the geometry of the 185 kg NaI[Tl] prototype detector, NaIνE-185 used in the simulations. 24 NaI[Tl] crystals are wrapped inside the aluminum casing with photomultiplier tubes attached on one end. The NaI[Tl] arrays are surrounded by 5 steel plates (blue) and 5 plastic muon veto panels (green). Right: the zoomed out perspective. The blue box on the top represents the 25 by 25 by 8 meter water-equivalent overburden and the red box represents the SNS hallway or the neutrino alley.

To perform the simulations, a GDML geometry was created, shown in figure 4.4. 24 NaI arrays, covered by 5 steel plates (blue) and 5 muon vetoes (green) was placed in a simplified SNS hallway (red) with the Hot Off-Gas pipe, which carries away radioactive gasses produced during beam operations as explained in chapter 3. The detector holder was not included as it would not contribute much, so the detector arrays appeared to be levitating. On the very top a 25 by 25 by 8 meter water equivalent overburden was included, mainly for the cosmic muon simulation, as other types of simulated events would not pass the overburden. Details of major components used in the geometry are listed in table 4.1. Only the NaI crystals were selected as sensitive volumes, where energy depositions were recorded in the production simulations. For exploratory studies, such as veto triggers, sensitive volumes were selected based on volumes of interest.

4.1.4 Post-Processing

Overview

The post-processing algorithm is described above in algorithm 1, which contains four modules:

- Attributes assignment, like the number of events, and ROOT to Pandas conversion through root_pandas or uproot.
- Time window and deadtime treatment to mimic digitizer behaviour.
- Nuclear recoil quenching models[4].
- Channel wise total energy smearing per event.

The algorithm takes in ROOT files as input and produces pandas dataframes[5] saved in the format of pickle files for more efficient revisits and analyses. A pkl to ROOT conversion script was also developed for people in need. All the data processing were achieved through pandas dataframe built-in functions and user customized python functions. All the attributes could be easily reassigned to suit different detector setups. Only energies within certain global time intervals were integrated due to the time window and deadtime from the digitizer used. Since most energy depositions happened within 100 ns, this treatment did not have a huge effect. Because of the time treatment, each throw from the simulation input could end up producing multiple events in the output. The particle types were encoded in the Monte Carlo particle numbering scheme [80]. Note that channel 14 in the simulation is treated as a passive volume as the real data processing due to its large amount of noises. The nuclear recoil quenching was treated based on the nucleus of interest. Both

[4] Depending on the sensitive volume ID and the particle ID, quenching would done through either equation 4.5 or 4.11 for eligible neutron induced energy depositions.

[5] https://pandas.pydata.org/docs/user_guide/10min.html

the quenching and the smearing modules could be easily adjusted. The production code supports multithreading. The final output contains several features or columns: saturation flag (if there exists energy sum in a single channel larger than 60 MeV); N by 24 energy arrays in MeV; N by 24 t_0 time arrays in ns, which are re-zeroed at the lowest value (channels with no energy deposition will have negative time values, equal to the minimal value times -1); total Energy; Multiplicity; other features for machine learning.

Energies of nuclear recoils measured by scintillators are often smaller than their theoretical values, due to a lower than expected amount of light yield. Quenching factors are used to describe this loss of energies. They are often defined as the scintillation light yield for nuclear recoils relative to those for gamma rays or electron-induced radiation of the same energy. Quenching factors are energy dependent. In the case of charged-current interactions, they do not contribute much to the total energy spectra, as electron interactions dominate. However, combined with the effects of detector thresholds, they can affect detection multiplicities. For example, a 600 keV proton recoil would trigger the NaI detector if the threshold is 520 keV and quenching (about 10%) is not applied. There are two commonly used models for quenching factors. In the simulation, the most suited one of the two was applied to each sensitive volume.

Algorithm 1 Post-processing algorithm

Input: .ROOT simulations.
Output: .pkl dataframe.
Initialization:
$N \leftarrow 100000$ ▷ Number of throws per simulation
$V \leftarrow 24$ ▷ Number of channels
$T_{group} \leftarrow 400$ ns ▷ Time window for event grouping
$T_{window} \leftarrow 3.75\mu s$ ▷ Integration window
$T_{dead} \leftarrow 10\mu s$ ▷ Hold off time since pulse
$E_{threshold} \leftarrow 1$ MeV ▷ PMT threshold
Main:
for $i = 0, 1, 2, \ldots, N-1$ **do**
  for $j = 0, 1, 2, \ldots, V-1$ **do**
    if j != 14 **then** ▷ Channel 14 discarded due to high noise
      1. Find the timestamp of the first energy deposition:
         $k \leftarrow 0$
         $T_{0,j,k} \leftarrow \text{Min}\{t_j \mid dE_{t_j} > 0\}$
      2. Add up the energy depositions in the integration window:
         $E_{T_{0,j},pid} \leftarrow \sum_t dE_{t_j,pid} \times \mathbb{1}_{T_{0,j,k} \leq t_j \leq T_{0,j}+T_{window}}$
      3. Update $T_{0,j,k}$:
         $k \leftarrow k+1$
         $T_{0,j,k} \leftarrow \text{Min}\{t_j \mid dE_{t_j} > 0,\ t > T_{0,j,k-1} + T_{dead}\}$
      4. Repeat step 2 and 3 until $T_{0,j,k}$ returns Null
      5. Apply Quenching functions to $E_{T_{0,j,k},pid}$ based on particle IDs (pid):
         $E_{T_{0,j,k},pid} \leftarrow \text{Quench}\{E_{T_{0,j,k},pid} \mid \text{Parent ID} = 2112\}$
      6. Add up energy depositions by $T_{0,j}$ and apply smearing to the sums:
         $E_{T_{0,j,k}} \leftarrow \text{Gaussian}(\mu \leftarrow \sum_t E_{T_{0,j,k},pid}, \sigma \leftarrow \text{Eq. 3.2})$
      7. Apply thresholds:
         $E_{T_{0,j,k}} \leftarrow E_{T_{0,j,k}} \times \mathbb{1}_{E_{T_{0,j,k}} > E_{threshold}}$
    end if
  end for
  8. Group E_{T_0} into each event based on T_0:
     $|T_{0,f,k} - T_{0,h,k}| \leq T_{group}$
  9. Assign $\text{Min}\{E_{T_{0,f,k},p}\}$ as the T_0 for each event p
  10. Produce other columns such as the < 60 MeV Saturation flag
end for

Quenching in Polystyrene

One model that describes quenching factors by ionization quenching is the Birk's saturation law [81]:

$$\frac{dL}{dr} = \frac{\frac{SdE}{dr}}{1 + kB\frac{dE}{dr}} \tag{4.3}$$

where dL/dr is the scintillation yield per unit path length r, S is the scintillation efficiency, kB is the first order constant related to quenching and dE/dr is absolute value of the energy loss per unit path length r in the medium which can be written as using the Bethe Formula [82]:

$$\frac{dE}{dr} = \frac{4\pi k_0^2 z^2 e^4 n}{mc^2\beta^2}\left(\ln\frac{2mc^2\beta^2}{I(1-\beta^2)} - \beta^2\right) \tag{4.4}$$

where k_0 is the Boltzman constant, z is the atomic number of the particle of interest, e is the magnitude of the electron charge, n is the number of electrons per unit volume in the medium or the electron density of the medium, m is the electron rest mass, c is the speed of light in vacuum, β is the speed of the particle of interest relative to c and I is the mean excitation energy of the medium. Then doing the integral yields:

$$E_{vis} = \int_0^{E_{true}} \frac{dE}{1 + kB\frac{dE}{dr}} \tag{4.5}$$

where E_{vis} is the recoil energy observed, E_{true} is the true recoil energy. In the post-processing script, equation 4.5 was used to calculate the observed energies of proton recoils and carbon recoils caused by neutrons in the plastic muon vetoes. The value of kB for energies below 850 eV (0.014 g MeV^{-1} cm^{-2}) was extracted from Reichhart *et al.* [83] and that for energies above 850 eV (0.009 g MeV^{-1} cm^{-2}) was extracted from Tretyak [84]. These kB values were then converted to cm MeV^{-1}. Any quenching factors applied to the vetoes only served exploratory studies, such

as veto triggers by charged-current interaction. Because these vetoes do not directly contribute to the energy integration of events within the NaI[Tl] arrays, there were no energy calibration studies performed for them. To numerically model the Birk's law, equation 4.4 can be written as with all constants combined:

$$\frac{dE}{dr} = \frac{5.08 \times 10^{-31} z^2 n}{\beta^2} \left(\ln \frac{1.02 \times 10^6 \beta^2}{1 - \beta^2} - \beta^2 - \ln I \right) \tag{4.6}$$

where the unit is MeV cm^{-1}. β can be calculated as:

$$\beta = \sqrt{1 - (\frac{E_{rest}}{E_{total}})^2} \tag{4.7}$$

where E_{rest} is the rest energy and where E_{total} is the total energy. The mean excitation energy of the medium I of an atom can be estimated using [85, 86]:

$$\begin{aligned} I &\approx 19\,\text{eV}; Z = 1 \\ I &\approx 11.2\,\text{eV} + 11.7Z\ \text{eV}; 2 \geq Z \leq 13 \\ I &\approx 52.8\,\text{eV} + 8.71Z\ \text{eV}; Z > 13 \end{aligned} \tag{4.8}$$

where Z is the atomic number. Then the I value of a molecule can be calculated using [85]:

$$n \ln I = \sum_i N_i Z_i I_i \tag{4.9}$$

where n is the total number of electrons in a molecule and N_i is the number of ith atom in the molecule. Note that the integral in equation 4.5 would not converge as the stopping power in equation 4.6 goes to negative infinity at extremely low kinetic energies. To address this, the stopping power was kept constant for energies smaller than the estimated critical energy (0.1 MeV for proton and 0.4 MeV for carbon). This estimation was backed up by the calculations of stopping power by Turner [87]. Putting everything together, in polystyrene or plastic detectors, at the energy region

of interest (< 1 MeV), the quenching factor of protons is in the order of 0.1 and that of carbon is in the order of 0.01.

Quenching in NaI[Tl]

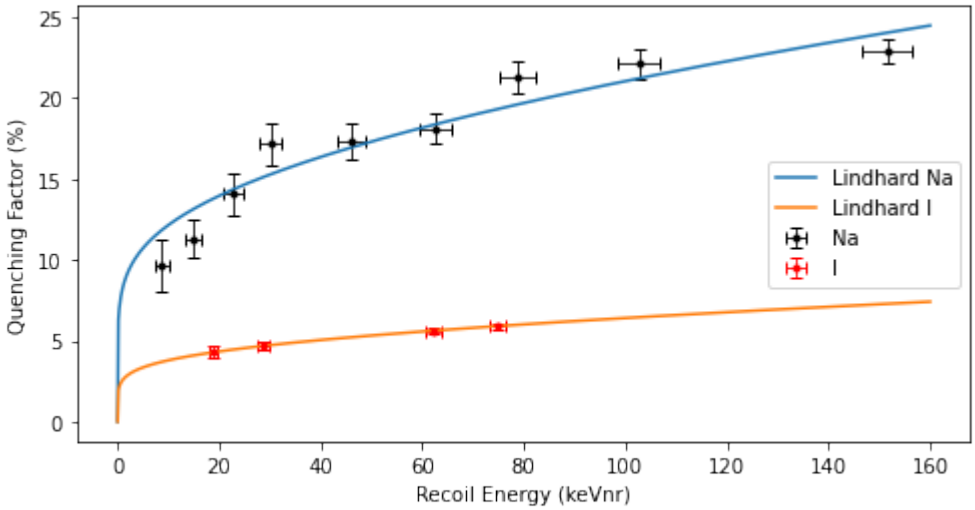

FIGURE 4.5: Quenching factor measurements of Sodium (black) and Iodine (red) from Joo et al.[88], with Lindhard model plotted using the parameters from Ko et al.[89].

Another model that describes quenching factors by nuclear collisions is the Lindhard theory [90]:

$$f(E_R) = \frac{kg(\epsilon)}{1 + kg(\epsilon)} \tag{4.10}$$

where $\epsilon = 11.5Z^{-7/3}E_R$, $k = 0.133Z^{2/3}A^{1/2}$, Z is the number of protons, and A is the number of nucleons. The function $g(\epsilon)$ is given by [91] to be:

$$g(\epsilon) = 3\epsilon^{0.15} + 0.7\epsilon^{0.6} + \epsilon \tag{4.11}$$

However, direct applications of the Lindhard model to the NaI[Tl] crystals match poorly to the recently measured QF values [89]. Ko, *et al*. provide a modified Lind-

hard model [89]:

$$\begin{aligned} k &= p_0 \\ \epsilon &= p_1 E_R \end{aligned} \tag{4.12}$$

where p_0 and p_1 are fit parameters. Figure 4.5 demonstrates the modified Lindhard models for sodium (blue) and iodine (orange) using the data from Joo *et al.*[88]. Iodine recoils are at least two times more quenched compared to sodium recoils. This model was used in the post-processing script to handle recoils of sodium and iodine and their daughter nuclei caused by neutrons in the NaI[Tl] arrays. For light nuclei such as hydrogen and helium isotopes, the Birk's saturation law is used with kB equal to 0.0038 g MeV^{-1} cm^{-2} from Tretyak [84].

Energy Resolution

To apply smearing, or energy resolution, for each channel, the total accumulated energy was randomly sampled from a normal distribution, with the total energy as the mean, and σ from equation 3.2 as the standard deviation. More details of how σ is calculated can be found in section 3.4.2 from chapter 3.

4.2 Charged-current Interaction on ^{127}I

4.2.1 Setup

The most important step for simulating the electron neutrino charged-current interaction on iodine, $^{127}\mathrm{I}(\nu_e, e^-)^{127}\mathrm{Xe}$, with MARLEY was the $B(\mathrm{GT})$ data selection. There were three possible candidates: Yu. S. Lutostansky and N. B. Shul'gina [92], M. Palarczyk et al. [71] and J. Engel, S. Pittel, and P. Vogel [93]. The second one came from experiments while the other two were theoretical calculations. To incorporate these $B(\mathrm{GT})$ values to MARLEY, a Fermi strength value corresponding to the isobaric analog state (IAS) was added using $N - Z$ by this author. All $B(\mathrm{GT})$ values were scaled up by 1.26^2 to undo the applied quenching. The scaling on $B(\mathrm{GT})$

data affects cross section calculation but does not affect MARLEY simulations, as all B(GT) are scaled up by the same factor. In other models, B(GT) quenching could affect energy spectra, as MARLEY does not currently handle forbidden transitions. Then the MARLEY outputs using these three different sources of B(GT) values were compared. As mentioned in earlier chapters, charged-current interactions could produce neutrons, protons, gamma rays or alphas besides electrons, from de-excitations of ^{127}Xe. Table 4.2 lists the % of all MARLEY events that emitted the specific type of particles in the final state besides an electron. The three B(GT) sources produced similar results from which it was clear that neutrons, gamma rays and electrons were the dominant products in the final state. Then the electromagnetic (electrons plus gamma rays) and neutron energy spectra were compared, as shown in figure 4.6. There was no significant difference either. As a result, the MARLEY output using the B(GT) values from M. Palarczyk et al. [71] was chosen to be passed on to Geant4, as they were measured from experiment.

Table 4.2: % of the 100,000 MARLEY events that emit the above particles along with an electron in the final state for each of B(GT) sources. Each B(GT) sources have its own normalization (100,000 events simulated).

Emitted Particles	Target	B(GT) source	% of all events
One neutron	^{127}I	Lutostansky and Shul'gina [92]	87.764%
One neutron	^{127}I	M. Palarczyk et al. [71]	83.685%
One neutron	^{127}I	J. Engel et al. [93]	82.744%
Two neutrons	^{127}I	Lutostansky and Shul'gina [92]	2.122%
Two neutrons	^{127}I	M. Palarczyk et al. [71]	3.393%
Two neutrons	^{127}I	J. Engel et al. [93]	1.943%
Proton	^{127}I	Lutostansky and Shul'gina [92]	1.813%
Proton	^{127}I	M. Palarczyk et al. [71]	2.429%
Proton	^{127}I	J. Engel et al. [93]	1.643%
Alpha	^{127}I	Lutostansky and Shul'gina [92]	0.064%
Alpha	^{127}I	M. Palarczyk et al. [71]	0.101%
Alpha	^{127}I	J. Engel et al. [93]	0.066%

The output from MARLEY, using the chosen B(GT) values with modification mentioned above, was passed on to Geant4 for simulation productions. Particles that carried the energy, like the electron, neutron(s), gamma rays and proton(s) in the final state of the each MARLEY event were initialized in a random location within one of the 24 NaI crystals in the geometry used, based on their four momentum. The alphas were ignored given their low rate. Then the 24 NaI crystals were flagged as the sensitive volumes, in which the energy depositions were recorded.

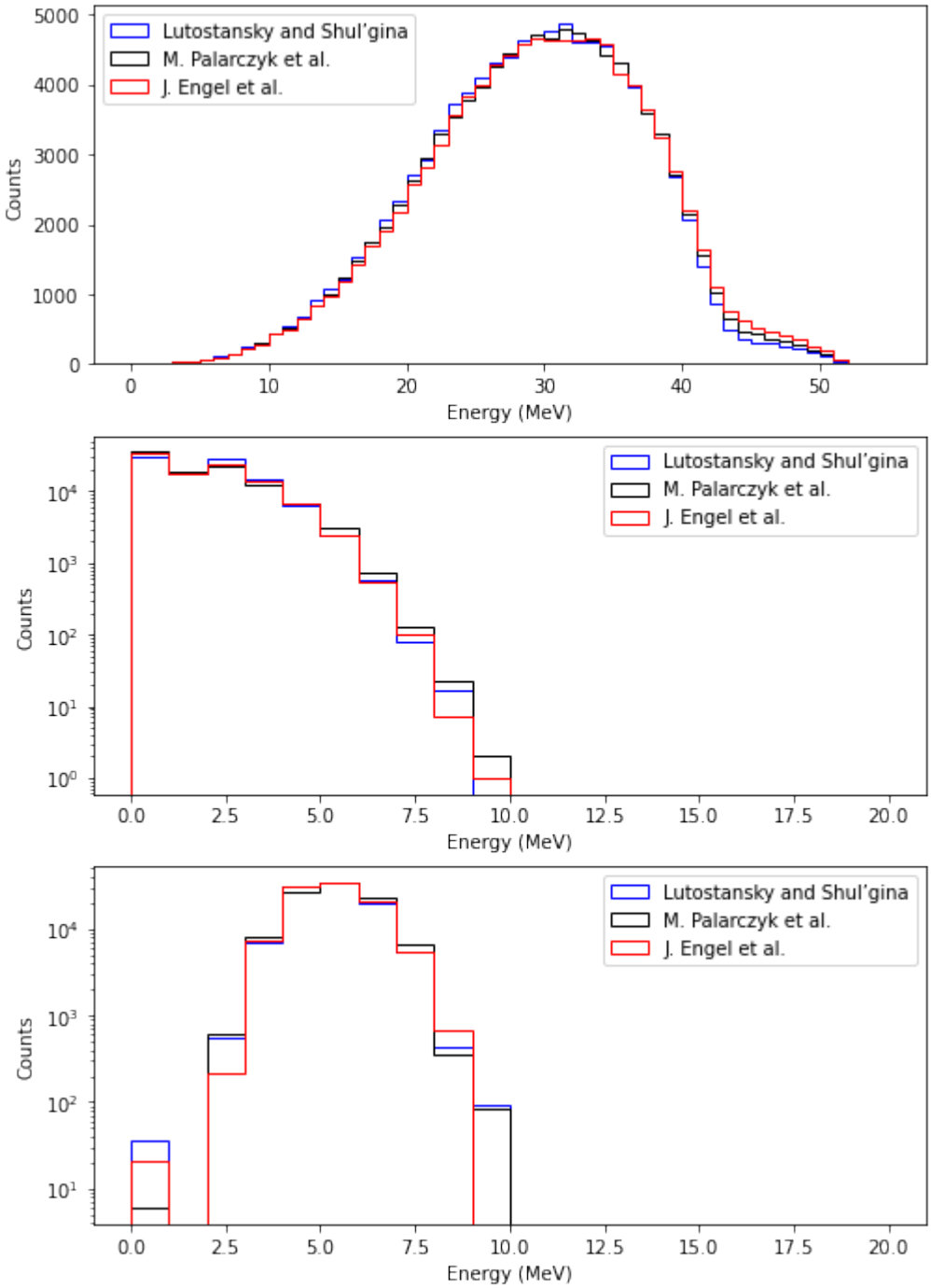

FIGURE 4.6: Top: the electromagnetic energy spectra of $^{127}\mathrm{I}(\nu_e, e^-)^{127}\mathrm{Xe}$ events generated by MARLEY using different $B(\mathrm{GT})$ values. Middle: the neutron energy spectra of $^{127}\mathrm{I}(\nu_e, e^-)^{127}\mathrm{Xe}$ events generated by MARLEY using different $B(\mathrm{GT})$ values. Bottom: the proton energy spectra of $^{127}\mathrm{I}(\nu_e, e^-)^{127}\mathrm{Xe}$ events generated by MARLEY using different $B(\mathrm{GT})$ values.

4.2.2 Result

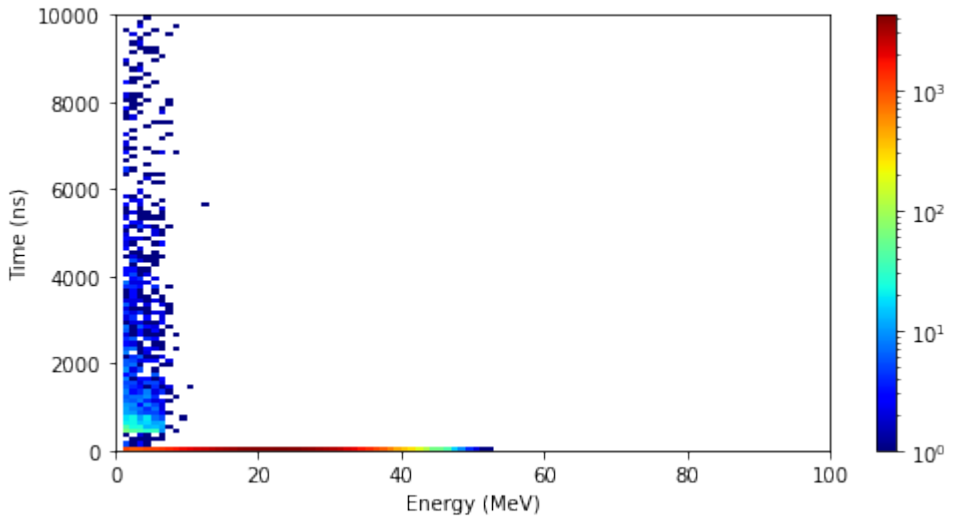

FIGURE 4.7: The 2D simulated ν_e charged-current interaction on ^{127}I energy vs t_0 histogram with log color scale.

Nuclear recoil quenchings were applied as described in the post-processing section, so the unit here MeV is equivalent to MeVee. As shown in figure 4.7, most simulated $^{127}\mathrm{I}(\nu_e, e^-)^{127}\mathrm{Xe}$ events started their energy depositions within the first 100 ns bin. The bin size was chosen due to the hundreds of nanosecond timing resolution of the detector. This was as expected because electrons are charged particles that suffer from the stopping power within the crystals. Given the energy peak around 23 MeV as shown in figure 4.8, it was also expected that a large portion of the electrons would not make it to a third crystal, verified by the multiplicity histogram. Note that the cut off in the energy spectrum near the low end (0 MeV) was caused by the 1 MeV threshold in the PMT bases used. It is easy to see that $^{127}\mathrm{I}(\nu_e, e^-)^{127}\mathrm{Xe}$ would produce events that overlap with steady state background events in terms of energies and multiplicity, especially in the 15 - 30 MeV and 2-4 multiplicity region. This result further justified the deployment of muon vetoes and led to a machine learning classifier exploration, which would be described in the ML chapter.

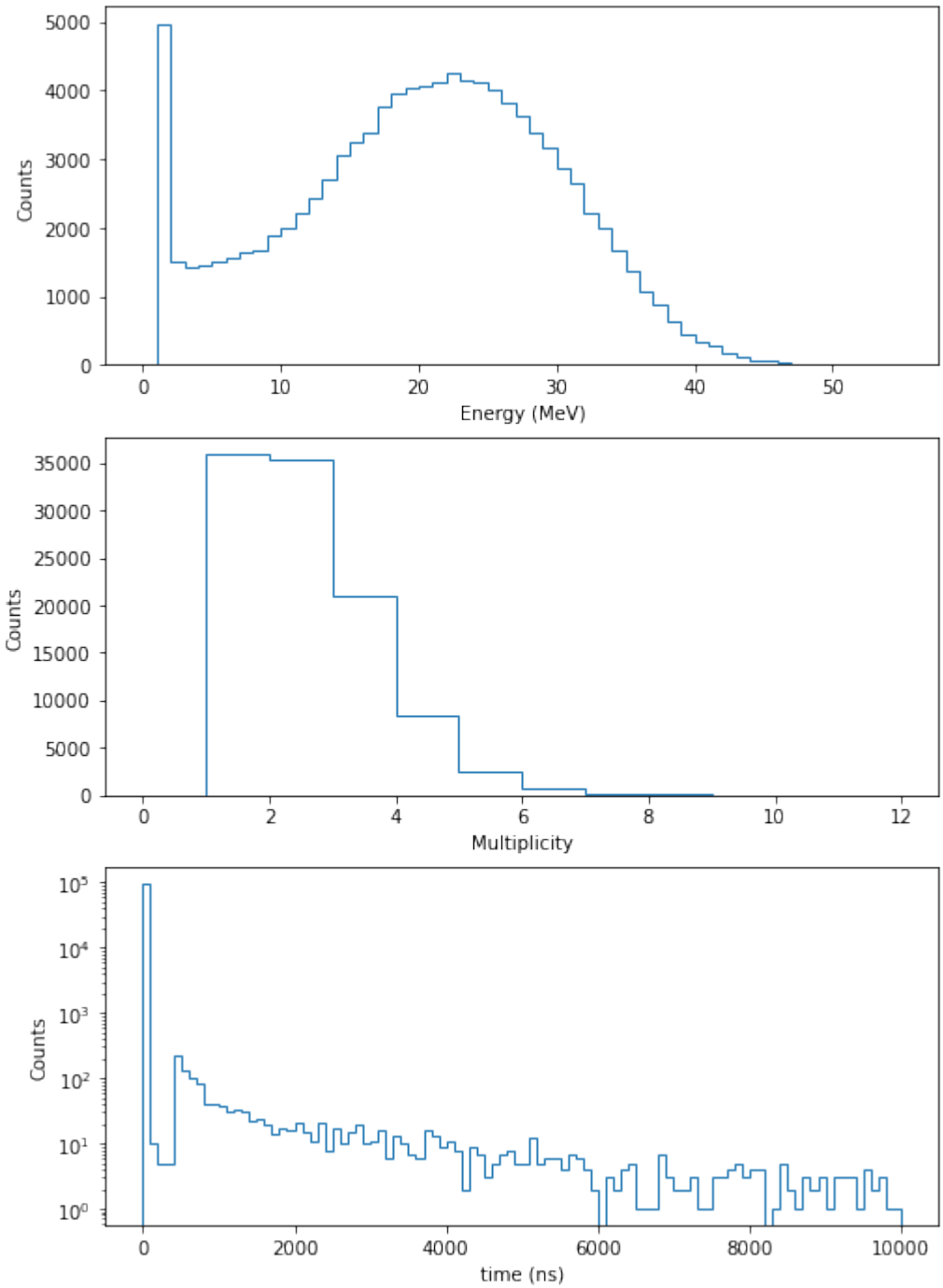

FIGURE 4.8: From top to bottom: simulated ν_e charged-current interaction on ^{127}I energy spectrum, multiplicity, t_0 histograms in log scale.

4.3 Charged-current Interaction on ^{23}Na

4.3.1 Setup

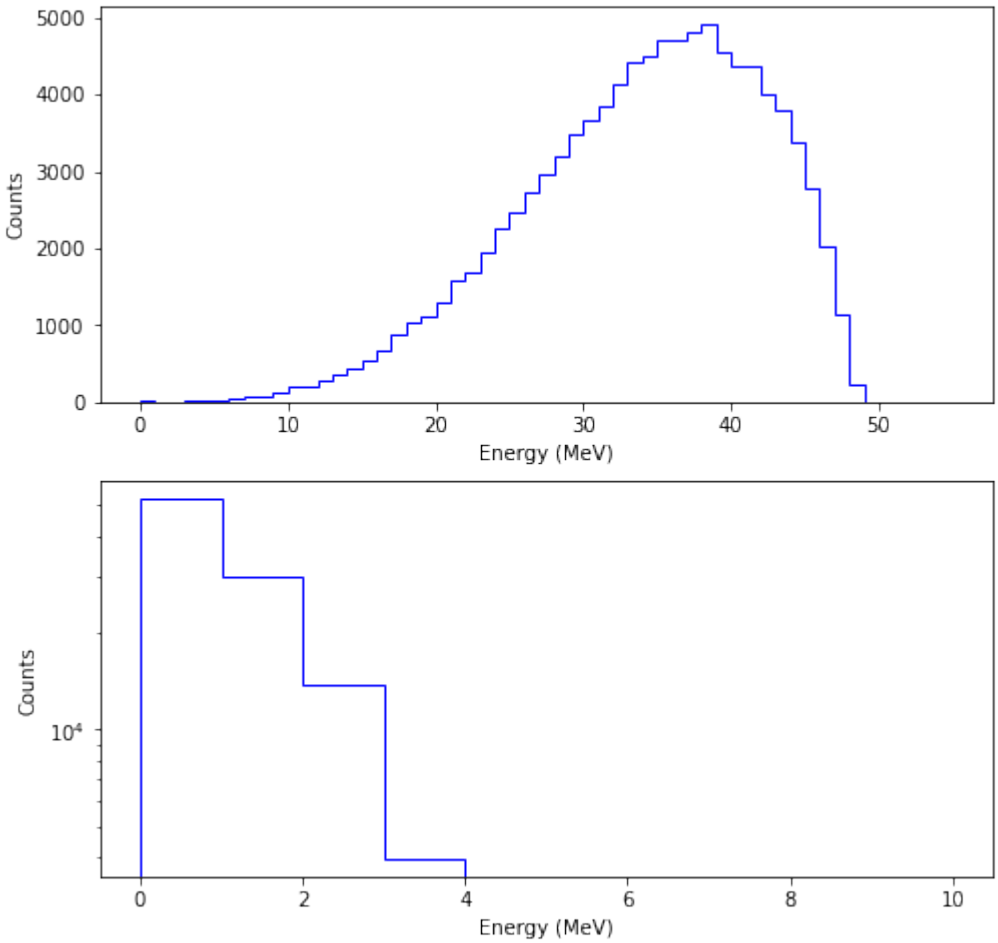

FIGURE 4.9: Top: the electromagnetic energy spectra of ^{23}Na$(\nu_e, e^-)^{23}$Mg events generated by MARLEY. Bottom: the proton energy spectra of ^{23}Na$(\nu_e, e^-)^{23}$Mg events generated by MARLEY.

The B(GT) data used here was from Y. Fujita et al. [72], the only available one from studies. Before serving as the input to MARLEY, these data points then went through similar treatments as the iodine B(GT) data, which included the addition of IAS but no scaling up. This is because Y. Fujita et al. [72] used the ^{23}Na(^{3}He,τ) charge exchange reaction, which were normalized by beta-decay strengths, to measure

the strengths as a function of energy instead of (p, n) reactions. There were however some differences between $^{127}\mathrm{I}(\nu_e, e^-)^{127}\mathrm{Xe}$ and $^{23}\mathrm{Na}(\nu_e, e^-)^{23}\mathrm{Mg}$ that needed to be handled. First, $^{23}\mathrm{Na}(\nu_e, e^-)^{23}\mathrm{Mg}$ did not produce any neutrons or alphas. About 7% of the $^{23}\mathrm{Na}(\nu_e, e^-)^{23}\mathrm{Mg}$ produced a proton besides an electron. The energy spectrum of protons and electrons plus gamma rays are shown in figure 4.9. Second, the resulting $^{23}\mathrm{Mg}$ in the ground state would go through a β^+ decay with a 11.317 second half-life:

$$^{23}_{12}\mathrm{Mg} \longrightarrow ^{23}_{11}\mathrm{Na} + \mathrm{e}^+ + \nu_\mathrm{e} \tag{4.13}$$

This decay signature did not have a huge effect on the energy spectrum in our 10 μs analysis window, but could be useful in background rejection with machine learning methods. To add the decay process to the equation, $^{23}\mathrm{Mg}$ atoms were also included in the input to Geant4.

4.3.2 Result

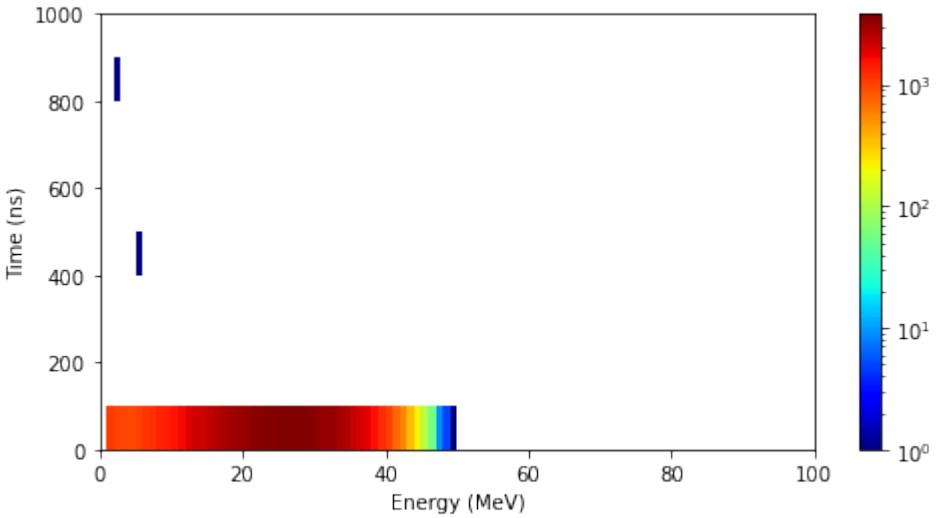

FIGURE 4.10: The 2D simulated ν_e charged-current interaction on $^{23}\mathrm{Na}$ energy vs t_0 histogram with log color scale.

Similar to $^{127}\mathrm{I}(\nu_e, e^-)^{127}\mathrm{Xe}$, as shown in figure 4.10, most simulated $^{23}\mathrm{Na}(\nu_e, e^-)^{23}\mathrm{Mg}$ events started their energy depositions within the first 100 ns bin. Since there was no neutron produced, there were almost no delayed events within the first 10 μs. However, due to the decay described in equation 4.13, as shown in figure 4.11, a significant amount of delay events would happen much later, outside the analysis window. Given the energy peak around 28 MeV as shown in figure 4.11, it was also expected that a large portion of the electrons would not make it to a third crystal, verified by the multiplicity histogram just as $^{127}\mathrm{I}(\nu_e, e^-)^{127}\mathrm{Xe}$. As a result, $^{23}\mathrm{Na}(\nu_e, e^-)^{23}\mathrm{Mg}$ would be indistinguishable from the $^{127}\mathrm{I}(\nu_e, e^-)^{127}\mathrm{Xe}$ signal in NaIνE-185. Luckily as shown in chapter 3, its cross section is only about 2% of that of $^{127}\mathrm{I}(\nu_e, e^-)^{127}\mathrm{Xe}$, assuming nomial values.

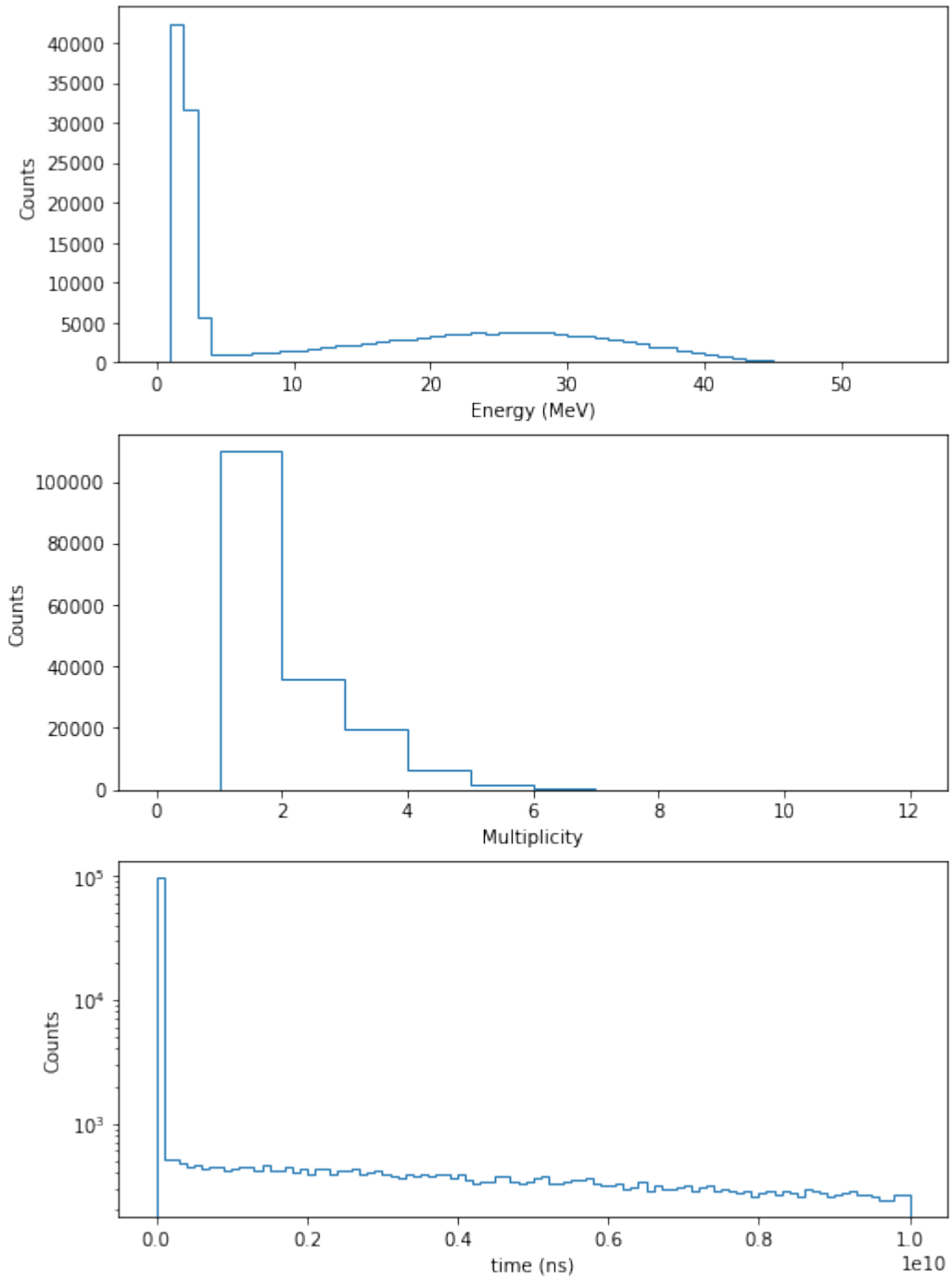

FIGURE 4.11: From top to bottom: simulated ν_e charged-current interaction on ^{23}Na energy spectrum, multiplicity, t_0 histograms in log scale.

4.4 Charged-current Interaction on ^{56}Fe

4.4.1 Setup

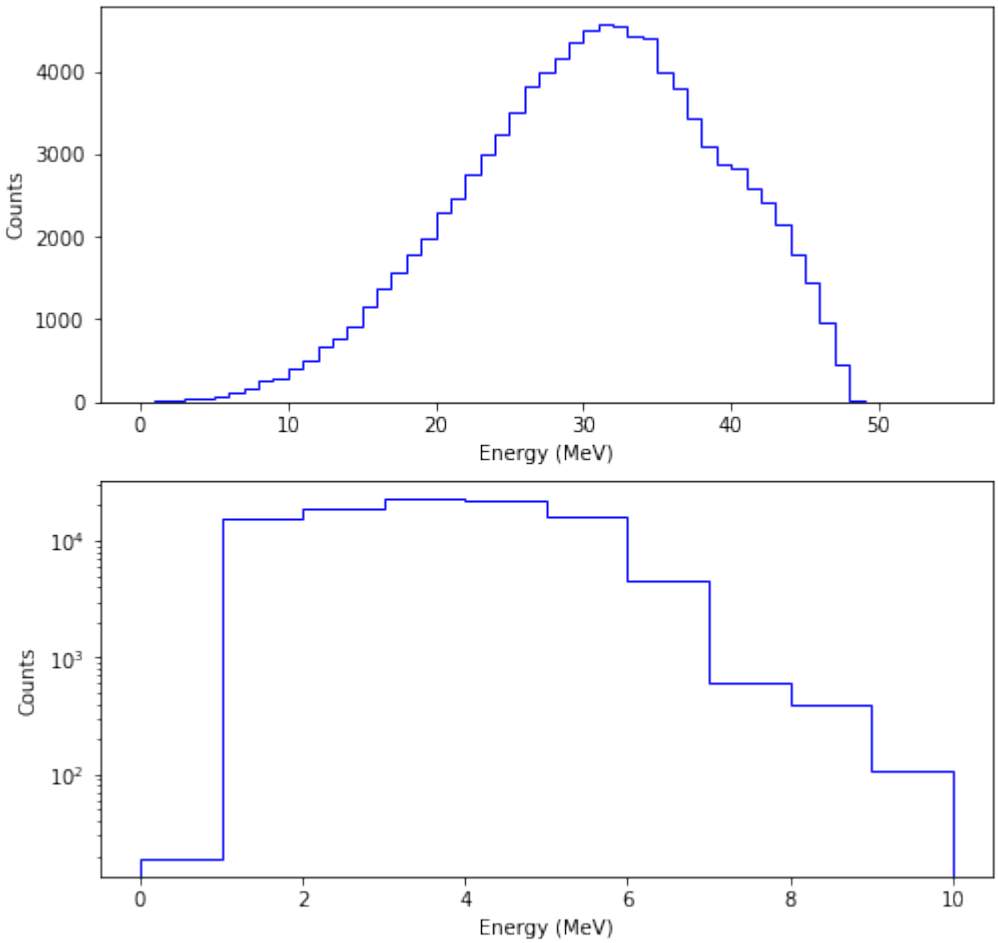

FIGURE 4.12: Top: the electromagnetic energy spectra of $^{56}\mathrm{Fe}(\nu_e, e^-)^{56}\mathrm{Co}$ events generated by MARLEY. Bottom: the proton energy spectra of $^{56}\mathrm{Fe}(\nu_e, e^-)^{56}\mathrm{Co}$ events generated by MARLEY.

The B(GT) data for CC on iron was from N. Paar et al. [73, 74]. These B(GT) values were scaled up with the IAS inserted before use in Geant4. Unlike the other two types of charged-current interactions, $^{56}\mathrm{Fe}(\nu_e, e^-)^{56}\mathrm{Co}$ throws were initialized inside the steel shielding rather than the NaI[Tl] crystals. This configuration was expected to significantly drop the number of events captured by the NaI[Tl] crystals

in the simulation, as electrons would lose energies outside the NaI[Tl] crystals. For example, a 25 MeV electron would only travel for about 1 cm before it is stopped within a steel plate[6]. Like $^{23}\mathrm{Na}(\nu_e, e^-)^{23}\mathrm{Mg}$, $^{56}\mathrm{Fe}(\nu_e, e^-)^{56}\mathrm{Co}$ produced mainly protons along side the electrons as 42% simulated throws produced protons. The energies of these protons were higher and peaked around 4 MeV as shown in figure 4.12. This also indicated that the deposited energies of $^{56}\mathrm{Fe}(\nu_e, e^-)^{56}\mathrm{Co}$ would be lower compared to the other two types of charged-current interactions.

4.4.2 Result

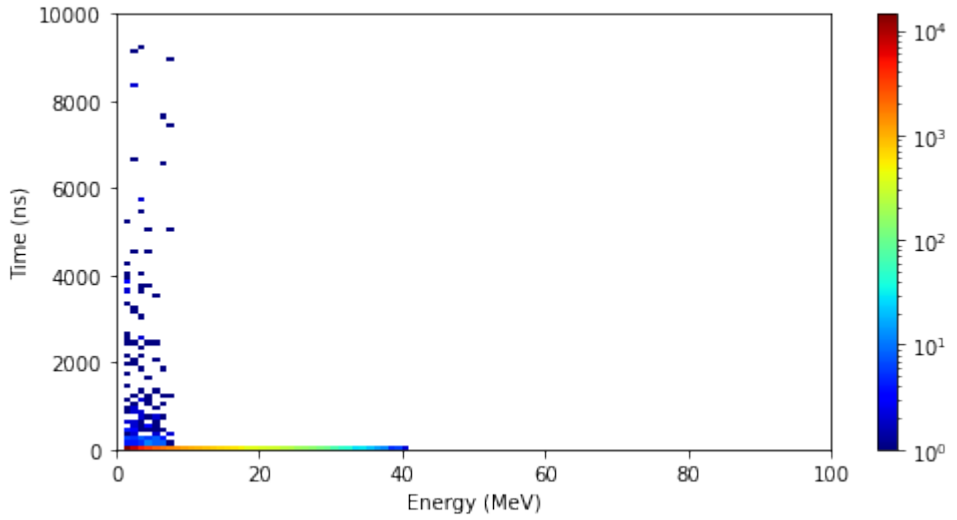

FIGURE 4.13: The 2D simulated ν_e charged-current interaction on ^{56}Fe energy vs t_0 histogram with log color scale.

As shown in figure 4.13, the deposited energies of $^{56}\mathrm{Fe}(\nu_e, e^-)^{56}\mathrm{Co}$ were much lower than the other two types of charged-current interactions. The delayed events were mostly caused by electrons entering the NaI[Tl] crystals late. About 11.74% of throws convert to events. A 10 MeV cut on the total energy would drop the majority of the $^{56}\mathrm{Fe}(\nu_e, e^-)^{56}\mathrm{Co}$ prompt events and all its delayed events so it is insignificant.

[6] The distance is estimated using the data provided by NIST, https://physics.nist.gov/cgi-bin/Star/e_table.pl

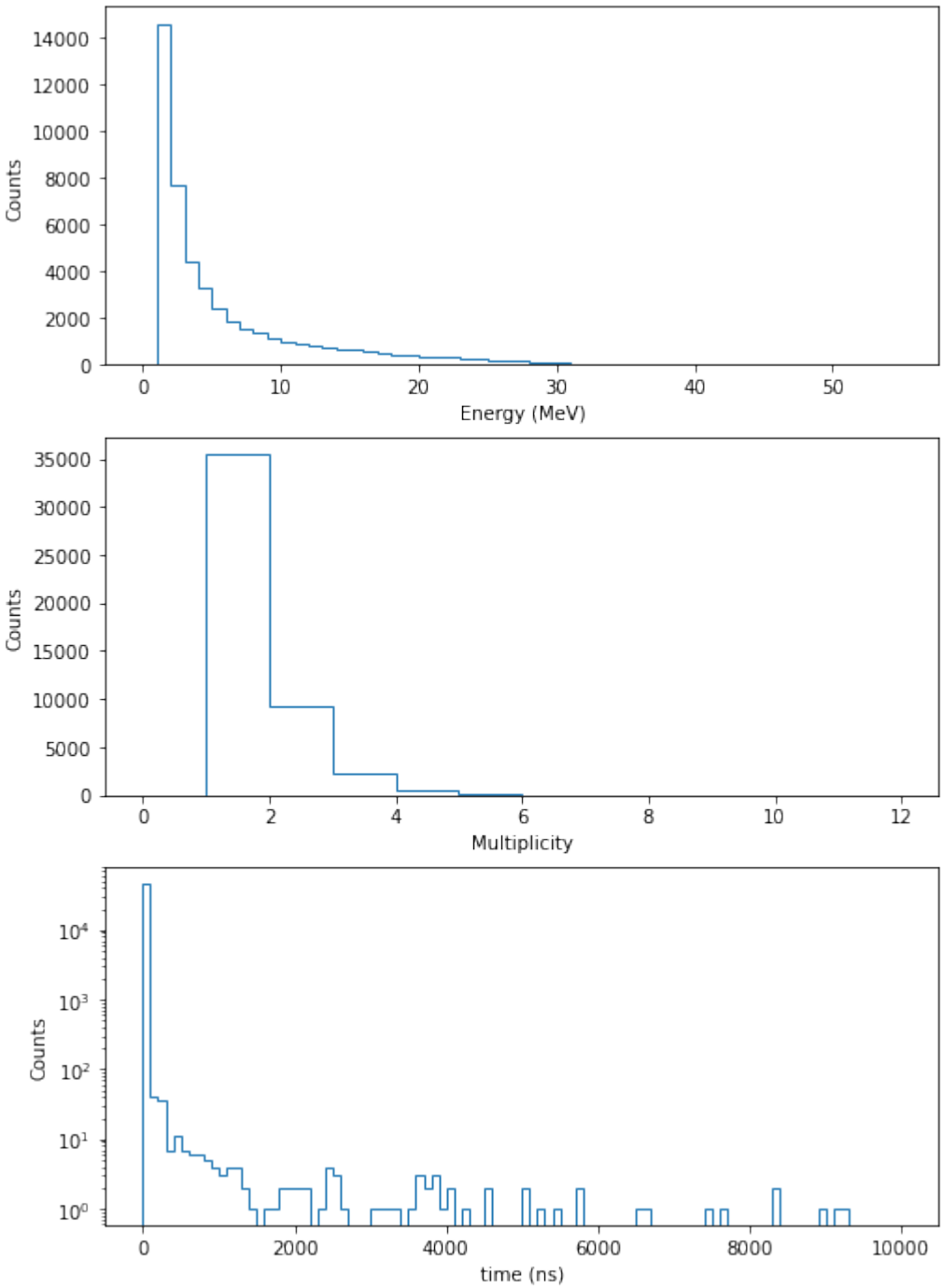

FIGURE 4.14: From top to bottom: simulated ν_e charged-current interaction on ^{56}Fe energy spectrum, multiplicity, t_0 histograms in log scale.

4.5 Muons

4.5.1 Setup

The motivation for the muon simulation was to produce simulated events for machine learning classifier development and to test detector responses. It would not be used in the cross section measurement directly, as state steady background events from the data were chosen instead. As mentioned earlier, the cosmic muon simulations used the Cosmic-ray Shower Library (CRY) [78] for event generation and Geant4 for the rest. A chosen amount of cosmic muons were initialized within the top side of the overburden, a 25 by 25 meter plane. The detector response of these muons largely depended on the size of the overburden. The 8 meter thick water-equivalent overburden, that resembled the overburden in the SNS hallway was derived by Dr. Yuri Efremenko from the University of Tennessee, Knoxville. The length and width were chosen after a variety of tests. Due to the attenuation within the overburden, the majority of the muons would never reach the detector, so it required lots of computational power to generate 100,000 events in the detector. To address this issue, all the muon simulations were packaged into a singularity image to be run on the Duke cluster with the finalized 25 by 25 by 8 meter overburden.

4.5.2 Result

All simulated muons went through a 10 MeV total energy cut, above which events in the beam-off data were believed to be steady state muons. To visualize the similarities between simulated muons and muons from the beam-off data, energy spectra and multiplicity histograms were plotted. To match the total number of counts, the count of each of the 1 MeV bins in the beam-off data was scaled down based on that in the muon simulations. Figure 4.15 shows the energy spectra and multiplicity histograms of the simulations and data whose energies are between 10 and 300 MeV.

The simulations produced more low multiplicity events, which were muons that went through one or two detector channels vertically and deposited sub-50-MeV energies. This is very likely due to the overburden estimation. The overburden across the actual SNS hallway is not uniform and muons come from the whole sky whose surface area is a lot larger than 625 m^2. Unfortunately it was neither feasible nor motivating to maximize the overburden and muon source plane coverage. As briefly mentioned earlier, muon simulations require a huge amount of computational power, as muons start from the top surface of the box shape overburden and the simulated muon flux is associated with its surface area. For example, less than 5% of one million muons simulated would even make it to the detector if a 150 by 150 by 8 meter overburden was used. Moreover, since the charged-current interactions have a upper energy limit of about 52.8 MeV, muons with energies higher than that could be easily filtered out. Figure 4.16 shows the energy spectra and multiplicity histograms of the simulations and data whose energies are between 10 and 55 MeV. Here the two match pretty well. The detector responses were therefore verified.

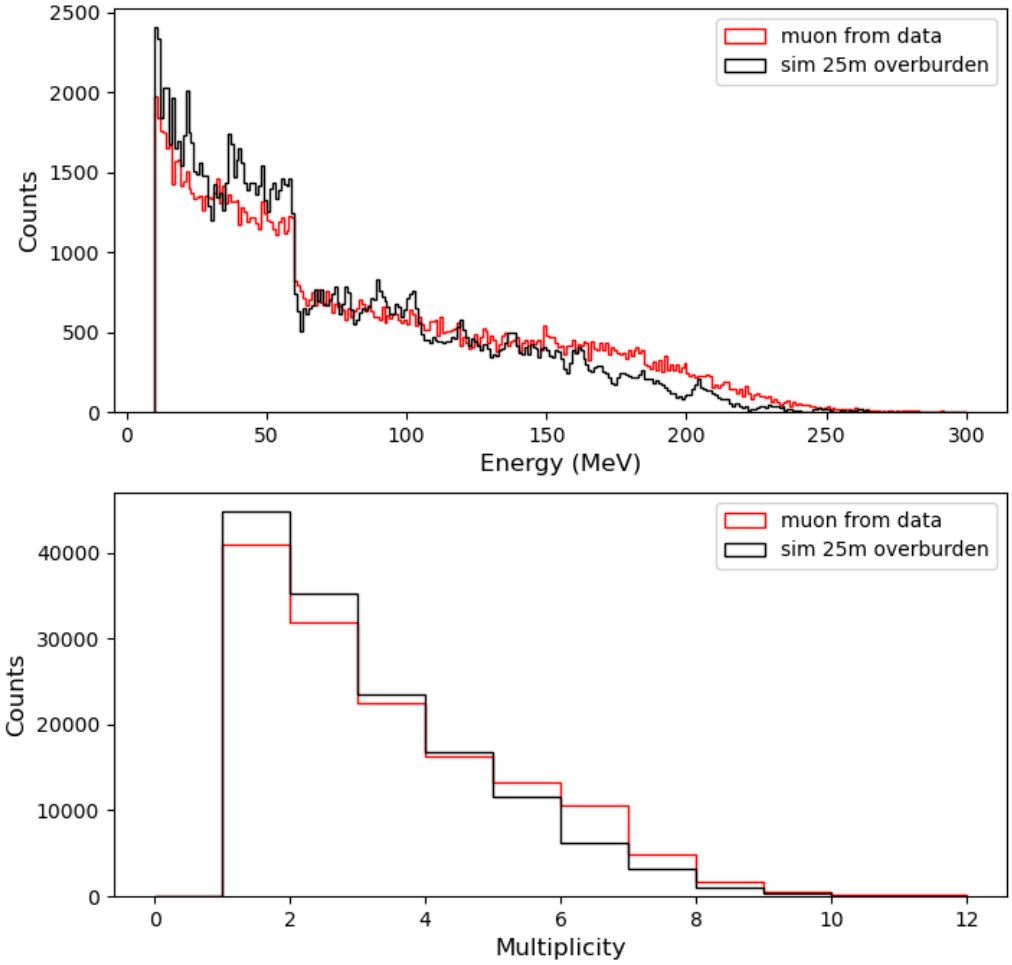

FIGURE 4.15: Top: muon sim vs muon from beam-off data spectra (10-300 MeV) with Michel corrections applied. Bottom: sim vs beam-off multiplicity.

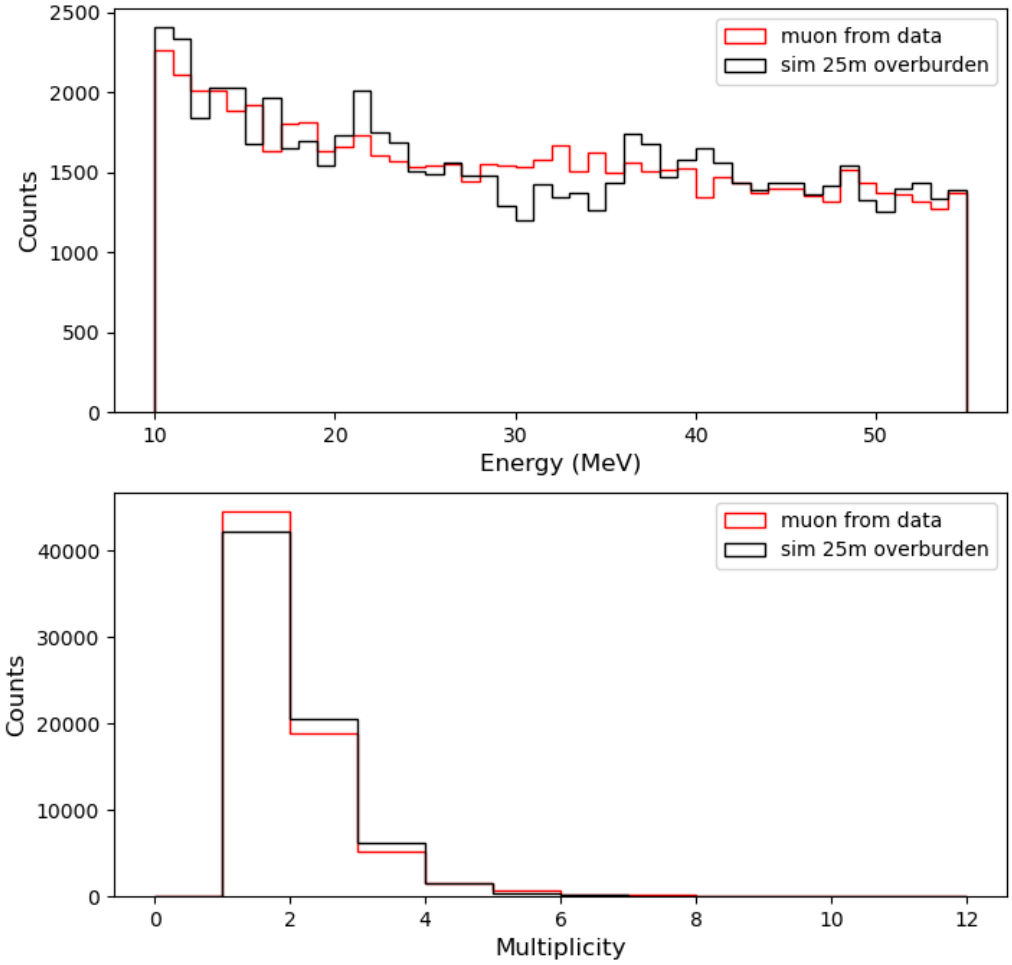

FIGURE 4.16: Top: muon sim vs muon from beam-off data spectra (10-55 MeV) with Michel corrections applied. Bottom: sim vs beam-off multiplicity.

4.6 Beam Related Neutrons

4.6.1 Setup

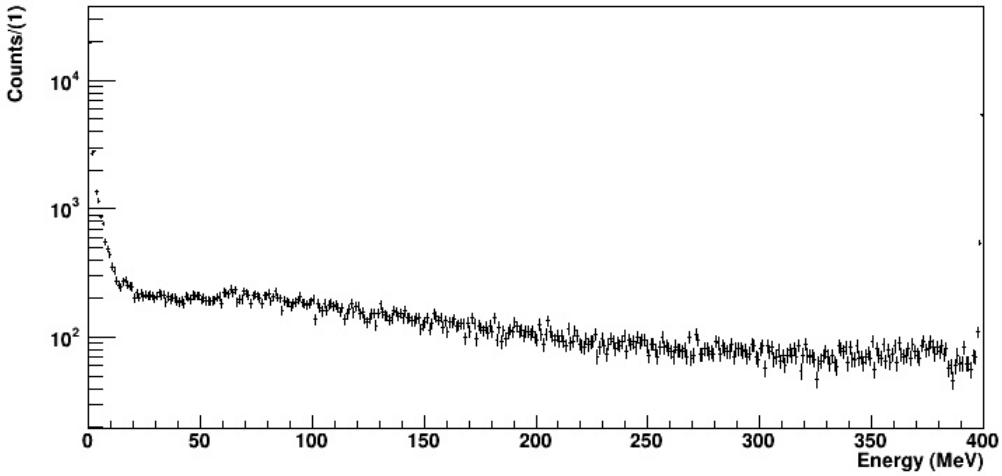

FIGURE 4.17: The energy spectrum of the simulated beam related neutron in the SNS hallway by Brandon Becker from the University of Tennessee-Knoxville.

The beam related neutron (BRN) simulation presented in this work was based on the spectrum shown in figure 4.17. This spectrum, by Dr. Brandon Becker, described energies of simulated neutrons in the SNS hallway. These neutrons were initialized 100 cm within the wall, adjacent to the NaI[Tl] prototype detector. The peak at 400 MeV represented the fast beam related neutrons that went through the concrete and the lower end peak represented the secondary neutrons produced roughly in the past 100 cm within the concrete. This spectrum was fed into Gears and Geant4 as a 7 by 4.5 meter plane neutron source, attached on the wall adjacent to the detector. The simulations were done on the ORNL cluster, with Geant4 photo evaporation set to 1 to prioritize energy conservation.

4.6.2 Result

Because of the pulsed neutrino source, timing of events contributes largely to background studies and rejections. Figure 4.18 shows the 2D energy vs t_0 histogram in log scale for post-processed BRN simulations. t_0 is defined as the Geant4 global time when the first energy deposition of an event happens. In the simulation, the majority of BRN energy depositions happened in the first 100 ns, and as expected the total energy deposited peak at sub 10 MeV after quenching. Less than 3% of the BRN events that had none zero energy depositions in the detector deposited at least 10 MeV, 1000 ns after the global time 0. These events were likely caused by high energy neutrons bouncing around shielding materials and entering the detector later. Additionally, the 1 MeV total energy per channel threshold used in the post-processing script could eliminate energy depositions with small t_0 in an event. Figure 4.19 confirms the dominance of low energy and low multiplicity events, made of gamma and nuclear recoils caused by BRNs. A simple cut on total energy, for example 10 MeV, would remove about 77% of the BRNs. However, from merely the perspective of the topology in the energy space, some BRN events are indeed hard to distinguish from charged-current signals. A maximum likelihood fit in the energy and time space could resolve this issue.

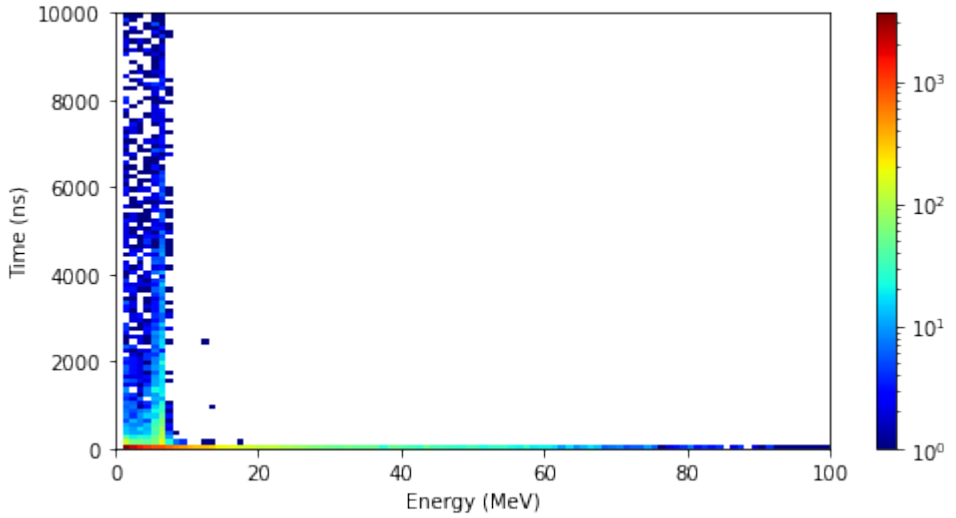

FIGURE 4.18: The 2D simulated visible BRN energy vs t_0 histogram with log color scale.

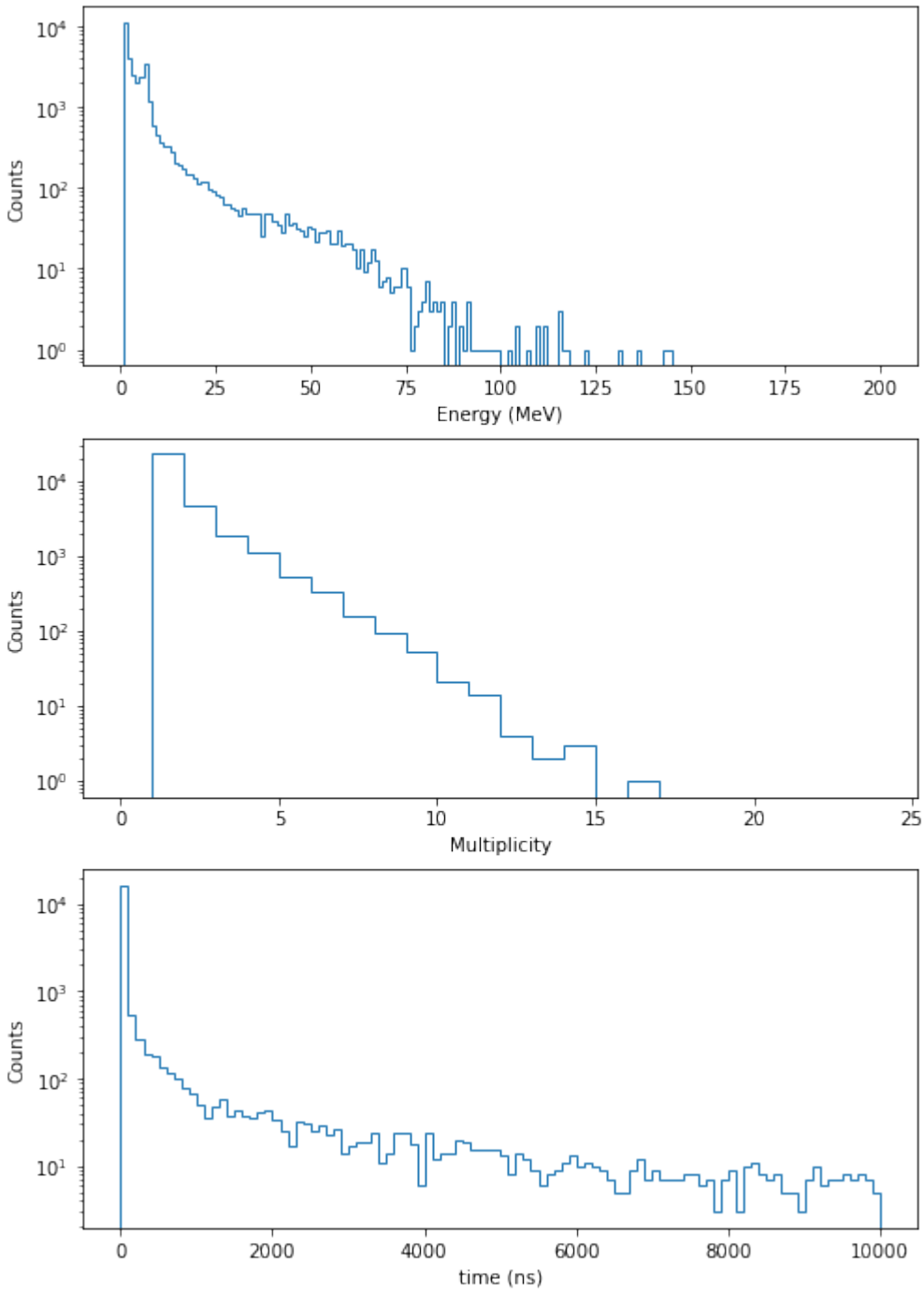

FIGURE 4.19: From top to bottom: simulated visible BRN energy spectrum, multiplicity, t_0 histograms in log scale.

4.7 Veto Trigger Check

It is important to know the trigger rate by the three types of charged-current interactions of the plastic muon vetoes because: first, they could be mistakenly flagged as steady state backgrounds and filtered out; second, this helps better estimate the normalization factors used for PDF fitting. To estimate this rate, modified charged-current simulations on ^{127}I, ^{23}Na and ^{56}Fe were performed. In addition to the 24 NaI[Tl] crystals, all 5 steel plates and 5 muon vetoes were set as sensitive volumes. No energy resolution was applied for these additional sensitive volumes. Quenching described in the post-processing section was applied to proton, other hydrogen isotopes, helium isotopes and carbon nuclei recoils caused by neutrons in the muon vetoes. It was estimated that the energy threshold in use within the muon vetoes was between 300 keV and 700 keV because they were not triggered by the background 511 keV gamma rays. Details of energy depositions within the muon vetoes were studied through track tracing and particle identifications. Major causes of these non-trivial energy depositions include:

- Electrons within muon vetoes scattered by gamma rays (Compton scattering). These gamma rays could come from the charged-current interactions directly, sudden slowing down or deflection of electrons in the vicinity of strong magnetic fields of Iodine nuclei (bremsstrahlung) or inelastic neutron interactions.
- Electrons that escaped from the NaI[Tl] crystals and later bounced into the muon vetoes.
- Nuclear recoils caused by neutrons.
- Gamma rays or positrons that contribute little.

In the case of $^{127}\mathrm{I}(\nu_e, e^-)^{127}\mathrm{Xe}$ and $^{23}\mathrm{Na}(\nu_e, e^-)^{23}\mathrm{Mg}$, out of the 4 causes listed above, the first one dominated, whose process is demonstrated in figure 4.20, while

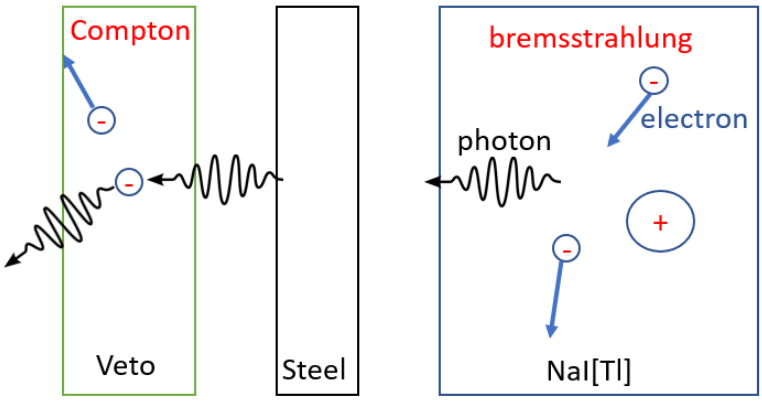

FIGURE 4.20: An example of the muon veto trigger by charged-current interactions. An electron produced by the signal caused bremsstrahlung, which in turn produced gamma rays. The gamma rays penetrated the steel shielding and produced Compton scattering within the muon veto.

for $^{56}\mathrm{Fe}(\nu_e, e^-)^{56}\mathrm{Co}$, electrons triggered the veto panels directly. As shown in figure 4.21, out of 100,000 simulated $^{127}\mathrm{I}(\nu_e, e^-)^{127}\mathrm{Xe}$ throws, about 25,924 throws triggered at least one of the 5 muon vetoes through electrons if no threshold applied. More than 99% of these triggers were caused by Compton scattering. With a 520 keV threshold, only 11,431 throws would trigger at least one of the 5 muon vetoes, and within these events, 8,712 triggers were caused by electrons. Since most contributions from gamma rays, positrons and neutron induced nuclear recoils were smaller than 1 MeV, the number of triggers dropped significantly with the introduction of the threshold as expected. Additionally, the side vetoes were triggered more often than the top one, due to their larger surface area. All these numbers would vary a little from simulations to simulations.

To convert the throw-wise trigger rate[7] to event-wise survival rate, the modified simulations were post-processed two times for each of the three veto thresholds: 300 keV, 500 keV and 700 keV. The three thresholds were chosen to get the lower and

[7] As mentioned in the post-processing section, one throw can end up multiple events due to event grouping.

upper limits. In the first pass, information from NaI[Tl] crystals, the analysis table, were extracted while in the second pass, that from the veto panels, the veto trigger table, were extracted. The two tables shared the same throw number column. Then the throw-to-event ratios, after simulation efficiency and veto trigger considerations, were extracted from the analysis table left joined[8] by the veto trigger table. Here the veto efficiency was due to either the passive volume channel 14 or the electrons that never entered the NaI[Tl] crystals. To address this efficiency, the raw throw count, 100,000, was used as the denominator in the ratio calculation. As shown in table 4.3, with a 500 keV veto threshold applied, in the 10-50 MeV region, 2.071% of the $^{56}\mathrm{Fe}(\nu_e, e^-)^{56}\mathrm{Co}$ simulated throws would be converted into events that do not trigger any of the veto panels, while the other two types have about a throw-to-event ratio of about 80%. This again proves that in the analysis window $^{56}\mathrm{Fe}(\nu_e, e^-)^{56}\mathrm{Co}$ would not be dominant despite the mass advantage of the steel plates over the NaI[Tl] crystals.

These muon veto triggers by charged-current interactions do depend on the kinetic energies of the electrons and gamma rays (electromagnetic energies) emitted. As shown in figure 4.22, the peaks of the electromagnetic energies of the events that trigger the veto center around 40 MeV for $^{23}\mathrm{Na}(\nu_e, e^-)^{23}\mathrm{Mg}$ and $^{56}\mathrm{Fe}(\nu_e, e^-)^{56}\mathrm{Co}$. But for $^{127}\mathrm{I}(\nu_e, e^-)^{127}\mathrm{Xe}$, the peak sits around 30 MeV, due to neutron emissions.

[8] A left join returns all rows and columns from the left table and the matching parts from the right table.

Table 4.3: The table that summaries the NaIνE-185 veto trigger studies of $^{127}\mathrm{I}(\nu_e, e^-)^{127}\mathrm{Xe}$,$^{23}\mathrm{Na}(\nu_e, e^-)^{23}\mathrm{Mg}$ and $^{56}\mathrm{Fe}(\nu_e, e^-)^{56}\mathrm{Co}$ with 300 keV, 500 keV and 700 keV veto thresholds.

Target	Veto Threshold (keV)	Event# between 10 and 55 MeV without veto trigger	Throw-to-Event ratio in %
^{127}I	300	74898	74.898%
^{127}I	500	78895	78.895%
^{127}I	700	81087	81.087%
^{23}Na	300	81043	81.043%
^{23}Na	500	82683	82.683%
^{23}Na	700	83571	83.571%
^{56}Fe	300	1994	1.994%
^{56}Fe	500	2071	2.071%
^{56}Fe	700	2112	2.112%

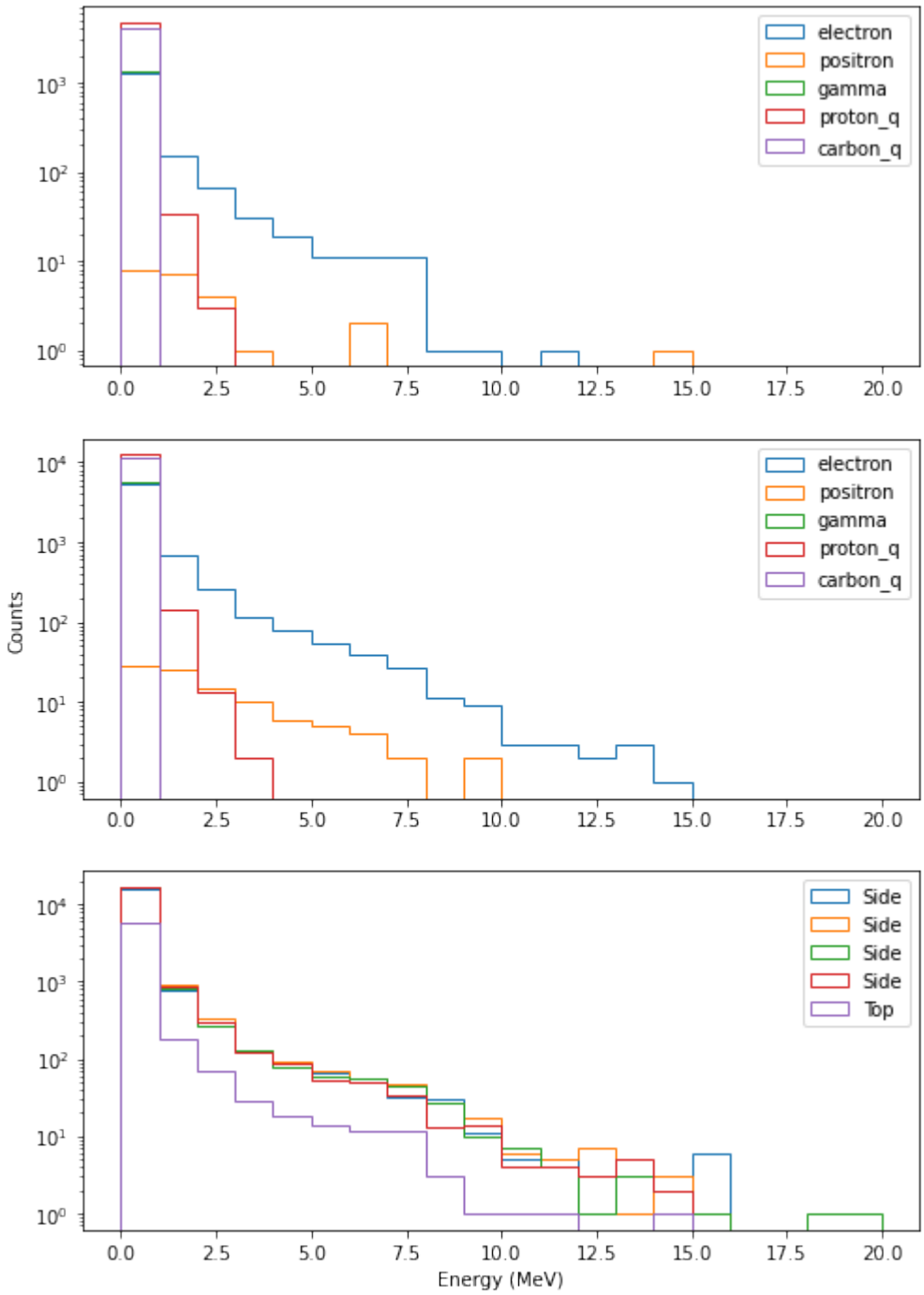

FIGURE 4.21: Top: the amount of triggers of the top muon veto by different types of particles from $^{127}\mathrm{I}(\nu_e, e^-)^{127}\mathrm{Xe}$. Middle: that of one of the side muon veto. Bottom: the total amount of triggers caused by $^{127}\mathrm{I}(\nu_e, e^-)^{127}\mathrm{Xe}$ in each of the five muon vetoes.

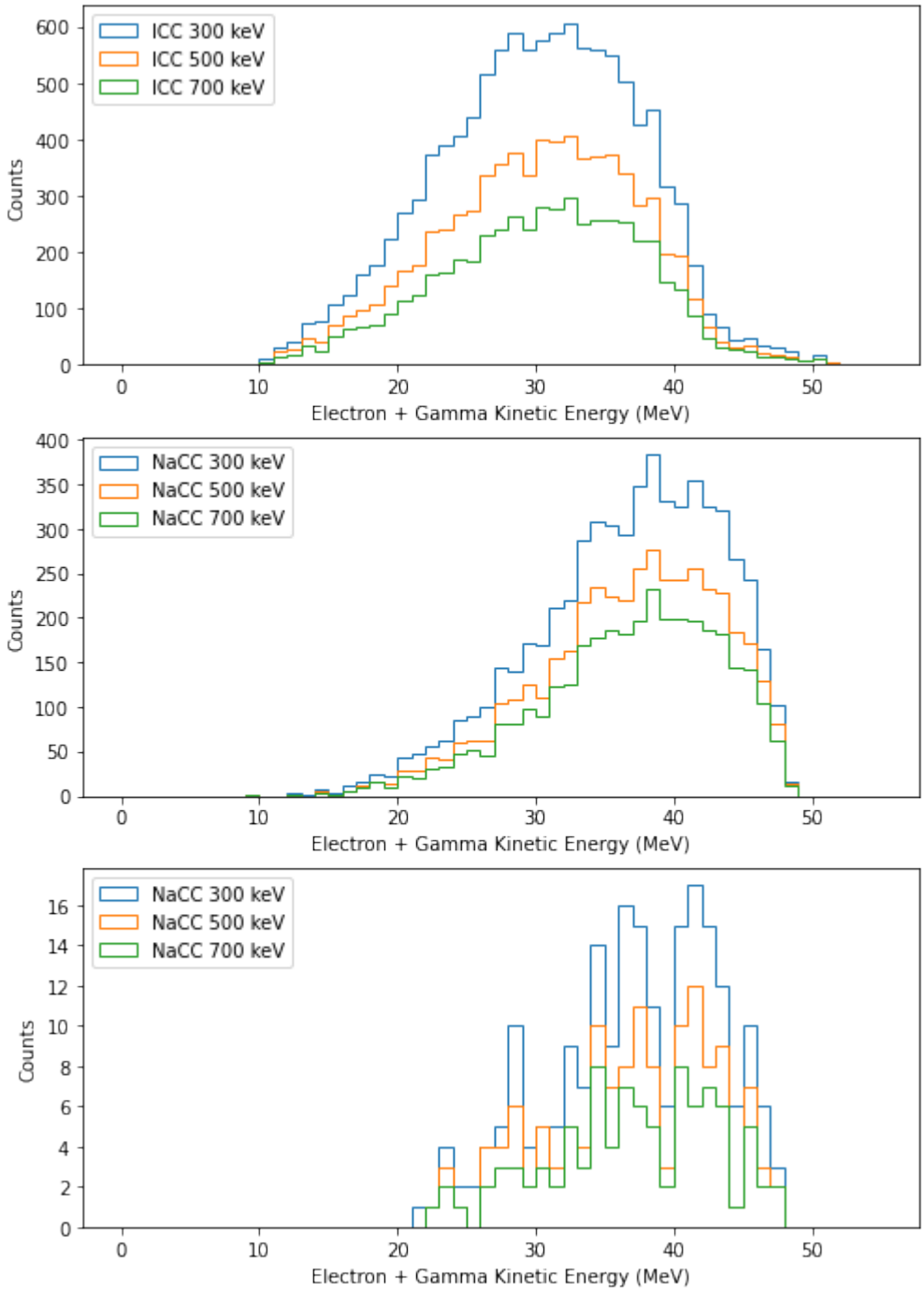

FIGURE 4.22: The number of veto triggers by $^{127}\mathrm{I}(\nu_e, e^-)^{127}\mathrm{Xe}$ (top), $^{23}\mathrm{Na}(\nu_e, e^-)^{23}\mathrm{Mg}$ (mid) and $^{56}\mathrm{Fe}(\nu_e, e^-)^{56}\mathrm{Co}$ (bot) vs the corresponding kinetic energies of electrons and gamma rays emitted with 300 keV, 500 keV and 700 keV muon veto thresholds. A 10 MeV cut was applied to the total energy deposited in the NaI crystals.

5

Machine Learning Classifier

5.1 Motivations

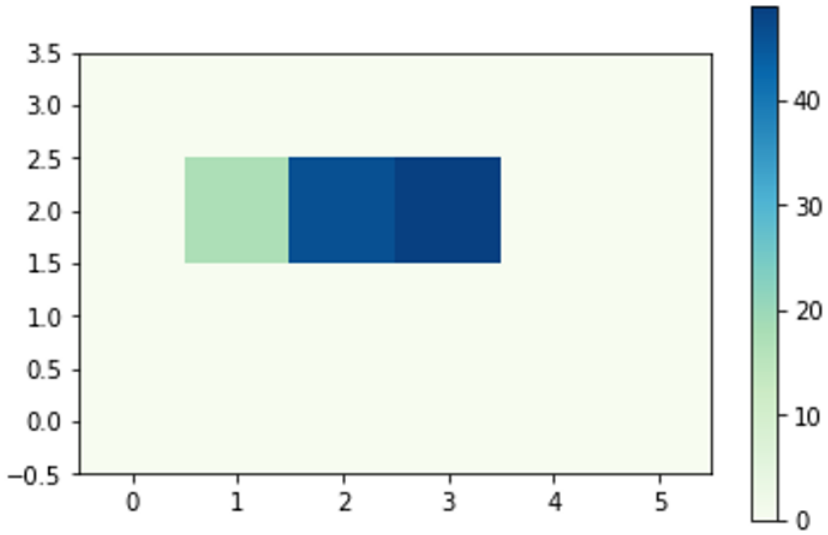

FIGURE 5.1: An example of a simulated muon event energy display (top view).

The original concept to use machine learning to classify NaIνE-185 data came from particle tracking. As shown in figure 5.1, a simulated muon leaves a linear track inside the NaIνE-185 detector. It was suspected that different types of particle

interactions inside the detector would result in different topological patterns. Two immediate benefits emerge if these patterns do exist and can be captured:

- A machine learning based muon veto system that can be easily scaled in size without extra costs would be really useful to both NaIνE-185 and the future ton scale NaI detectors. Currently NaIνE-185 uses plastic scintillators as muon vetoes, which are heavy and difficult to scale up.

- A machine learning classifier that can perform counting statistics and generate signal spectra would be attractive. The cross section measured this way could serve as a cross check to that with a more traditional methods, such as PDF fitting.

There are also examples from other collaborations of machine learning applications in physics. One good example is the KamNet, a customized Spherical Convolutional Neural Network used for a rare event search in KamLAND-Zen [94]. As machine learning and deep learning attracts more attention every day in both industries and academia, many physicists are seeking ways to incorporate them into their research. The National Science Foundation (NSF) also provided funding to early career scientists and students to support AI workforce development, such as the DANCEEdu fellowship.

5.2 Convolutional Neural Network

5.2.1 Introduction

Convolutional Neural Networks (CNN) are the most commonly applied class of Artificial Neural Network (ANN) for image classifications. It is a feed forward neural network trained with the backpropagation algorithm. The first idea of a 2D CNN was published by Wei Zhang et al. in 1988 [95]. Then in 1989, LeCun et al. published their CNN model designed to classify hand-written numbers [96], which paved

the way for the most famous CNN, LeNet5 [97], which was first introduced in 1998. Since then, there have been many different CNNs developed.

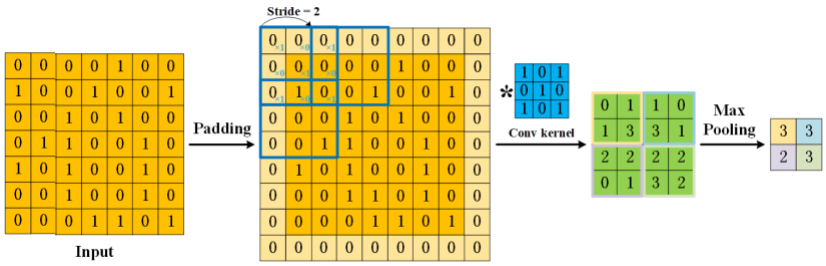

FIGURE 5.2: Illustration of the workflow of a convolutional layer and a pooling layer from ref [98].

A generic CNN contains the layers described below:

- Convolutional layers, the main building block of any CNN.
- Pooling layers for downsampling.
- Dense layers or fully-connected layers for classification.

The convolutional layers make CNN different than other types of ANNs. As shown in figure 5.2, a convolutional layer performs convolution on the input images with filters. A filter can be thought of as a matrix, which performs element-wise multiplication with a subset of the input matrix that shares the same size and then adds up the products into a single value. As a filter covers the entire input image matrix, the output will be the convoluted image. A n by m input, if convoluted by a d by f filter, will have a $(n - d + 1)$ by $(m - f + 1)$ output assuming a stride, the filter movement, of 1. The optimal weights of the filters are essentially obtained through backpropagation. This process essentially extracts the most important features from input images. Then after convolution, if the input is still too complex, pooling layers are used for downsampling. Finally after enough convolution and pooling, the extracted features are fed into dense layers for classification.

5.2.2 *Design and Discussion*

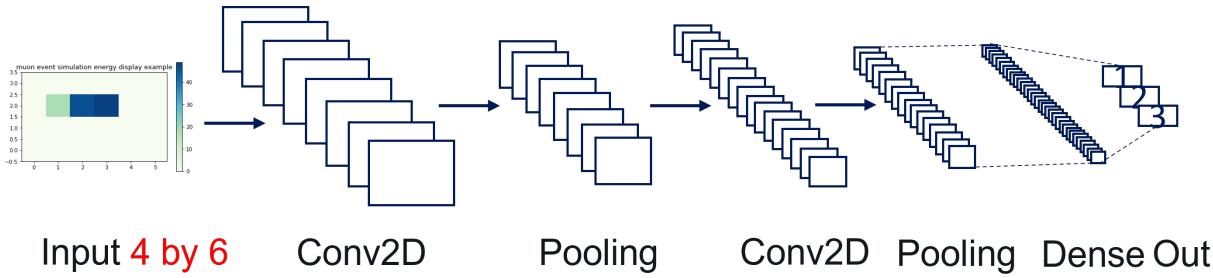

FIGURE 5.3: Demonstration of the CNN designed for NaIνE-185.

The first model developed for particle classification using NaIνE-185 data is a CNN, as it is straightforward to use the event energy displays shown in figure 5.1 as input. The structure, that contains two convolutional layers, two max pooling layers and one final dense layer, is rather simple as the input are 4 by 6 images. The three-class model, trained and tested with old generation[1] $^{127}\mathrm{I}(\nu_e, e^-)^{127}\mathrm{Xe}$, cosmic muon and cosmic neutron simulations, achieved a 77% recall, true positive rate, on the $^{127}\mathrm{I}(\nu_e, e^-)^{127}\mathrm{Xe}$ signal. The recall is mainly capped by the low multiplicity muon events that share the exact topology as the signals. Different data augmentation techniques such as rotations and zooming were found to be of no use. As the input images contain only 24 pixels, CNNs become too complex and unnecessary for the task. Therefore, this model was later deprecated. For larger detectors, such as the ton-scale NaI detector with hundreds of channels, this model however should be the go-to choice.

5.3 XGBoost

5.3.1 *Introduction*

XGBoost, Extreme Gradient Boosting, is an optimized, scalable and distributed gradient boosting library that provides a parallel tree boosting that solve many data

[1] These simulations do not have the event forming mechanism as those described in chapter 4.

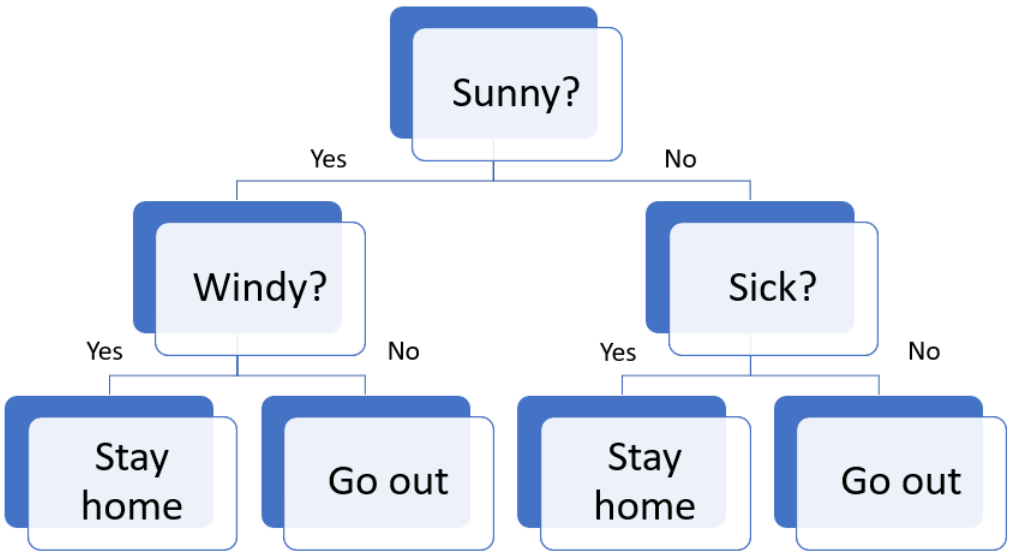

FIGURE 5.4: Illustration of a decision tree.

science problems in a fast and accurate way [99]. It has been widely used by people either on their own PCs or on major distributed environment such as Hadoop and Spark since its release on 2014. By its definition, XGBoost is an improved gradient boosting tree learner [100], which is an additive model that evolved from decision trees.

Decision Trees are a non-parametric supervised learning model that can be used for both classification and regression [101]. The main concept behind it is to make splits and generate branches, each of which lead to multiple decision nodes called leaf nodes, from the given data features based on certain rules. Figure 5.4 demonstrates a simple decision tree. Decision trees have many advantages, some of the most important ones include its ability to handle non-linear data structures, little requirement for data preparations and its interpretability through visualizations. However, decision trees tend to overfit and have high variance, as they often split too much on the training data and end up being too complicated to be generalized to new data. Pruning, or complexity reduction, could help in this case, but doing so would

also limit a decision tree's ability to learn and increases bias as a result. To address this issue, gradient boosting trees were introduced. Gradient boosting trees add up shallow decision trees called decision stumps with different weights, determined by the gradient of the loss function. The training process is then to minimize the loss function by adding one decision stump with its optimal weight a time. This way, the final output has lower variance than a extremely deep decision tree and lower bias than the decision stumps.

Compared to other gradient boosting tree learners, XGBoost has multiple advantages, such as:

- It introduces a regularization term in its objective function to address overfitting.
- It uses second order approximation of its objective function for faster convergence.
- It allows parallel processing by enumerating the features before the leaf nodes.

The first two advantages mentioned above can be visualized in the objective function of XGBoost, which can be written as after simplification with a mean squared error (MSE) loss function [99]:

$$\text{obj}^{(t)} = \sum_{i=1}^{n} \left[l\left(y_i, \hat{y}_i^{(t-1)}\right) + g_i f_t\left(x_i\right) + \frac{1}{2} h_i f_t^2\left(x_i\right) \right] + \omega\left(f_t\right) + \text{ constant} \tag{5.1}$$

where f represents the tree, i is the data index, t is the step index, l is the loss function, g_i and h_i are the first order and the second order derivatives defined as:

$$\begin{aligned} g_i &= \partial_{\hat{y}_i^{(t-1)}} l\left(y_i, \hat{y}_i^{(t-1)}\right) \\ h_i &= \partial^2_{\hat{y}_i^{(t-1)}} l\left(y_i, \hat{y}_i^{(t-1)}\right) \end{aligned} \tag{5.2}$$

Finally the ω term represents the model complexity defined as:

$$\omega(f) = \gamma T + \frac{1}{2}\lambda \sum_{j=1}^{T} w_j^2 \tag{5.3}$$

where T is the number of leaves and w is the vector of scores on leaves. If the trees have too many splits, the model complexity term will be large. So minimizing the objective function would punish those deep trees and overfitting would be addressed in the process.

5.3.2 Design

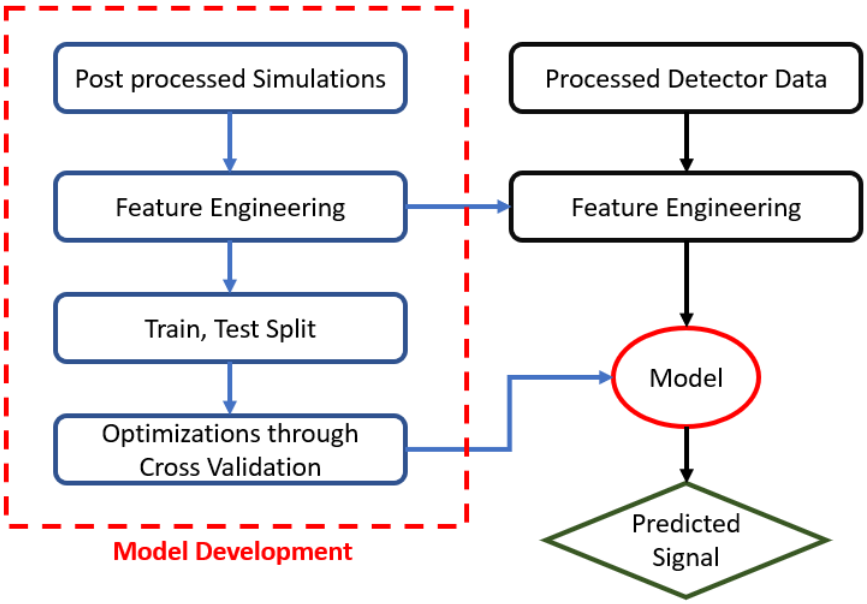

FIGURE 5.5: The workflow of the XGBoost based particle identifier.

In particle physics, it's extremely difficult to build an end-to-end machine learning pipeline for classifications and deploy it online for several reasons:

- The majority of computation resources for physicists in the US belongs to the federal government or private institutions. As a result, individuals do not have root access to either the clusters or the workstations.

- Detector data usually are recorded in binary form to save space and thus will require multiple processing before analyses.

- Detector data can be noisy particularly because of common hardware failures from time to time, such as beam upgrades or broken photomultiplier tubes. What's more, the data health check can only be conducted offline as it requires detailed analyses.

Therefore, the XGBoost based particle classifier [102] described in this work functions offline only. As shown in figure 5.5, the model is trained with post processed simulations described in the previous chapter. The model is designed to identify four different classes: $^{127}\mathrm{I}(\nu_e, e^-)^{127}\mathrm{Xe}$, $^{23}\mathrm{Na}(\nu_e, e^-)^{23}\mathrm{Mg}$, $^{56}\mathrm{Fe}(\nu_e, e^-)^{56}\mathrm{Co}$ and cosmic muons. The beam related neutrons are not included because they can be filtered out by timing cuts and their normalization is not well studied. The training data and the validation data in turn both contain equal share of each of the four classes to avoid class imbalance. However, in the real data, as shown in earlier chapters, the classes are not balanced. So at the model evaluation stage after training, the test data are made up based on the expected counts of each class. The training parameters of XGBoost such as the maximum depth per tree, the regularization strength term γ and the minimum child weight are determined through cross validations with the training data. To speed up this process, a RTX 3080 is used. Once the best parameters are determined, the model is trained with the training data and the determined parameters. After that the model is first tested with the validation set to get an estimate of its performance.

Then the model is evaluated with the test set. The recall and precision matrices are plotted as benchmarks of the model's performance. To estimate the error bars of the precision and recall for each class, 100 test sets are generated using the expected counts and random sampling. A confusion matrix is generated for each test set.

Then the matrix will be normalized by true label counts to produce the recall matrix and by predicted label counts to produce the precision matrix. The error of recall for a class is then just the standard deviation of all 100 recall values of that class. The same goes for the error of the precision. Once fully trained and tested, the model will take processed detector data as input. Then the predicted signals can either be used to plot the signal spectrum or to calculate the cross section using the below equation:

$$\text{Actual count} = \text{count of predicted signal} \times \frac{\text{Precision}}{\text{Recall}} \tag{5.4}$$

5.3.3 Feature Engineering

As mentioned earlier, the raw detector data is in binary form. After processing, it would involve features like energy depositions per channel and event multiplicities. It's important to select only the features that coexist in both the simulations and the detector data for model consistency. In the case of NaIνE-185, there are 24 NaI channels, one of which, channel 14, is treated as a passive volume due to its poor resolution. So the final input array contains the following features:

- The energy readings from all 23 working channels (sparse).
- The total energy of an event, which is just the sum of the above (dense).
- The multiplicity, the number of channels with non-zero energy depositions (dense).
- The variance of the energy depositions per event (dense).

To ensure better class separation, only data points with a total energy between 10 and 55 MeV are used. The above features are derived from physical intuitions and later verified by the feature importance output from the trained model. There

are also other features tested which however were abandoned due to low significance. Some examples are the encoded energy deposition order and total energy squared.

5.3.4 Result and Discussion

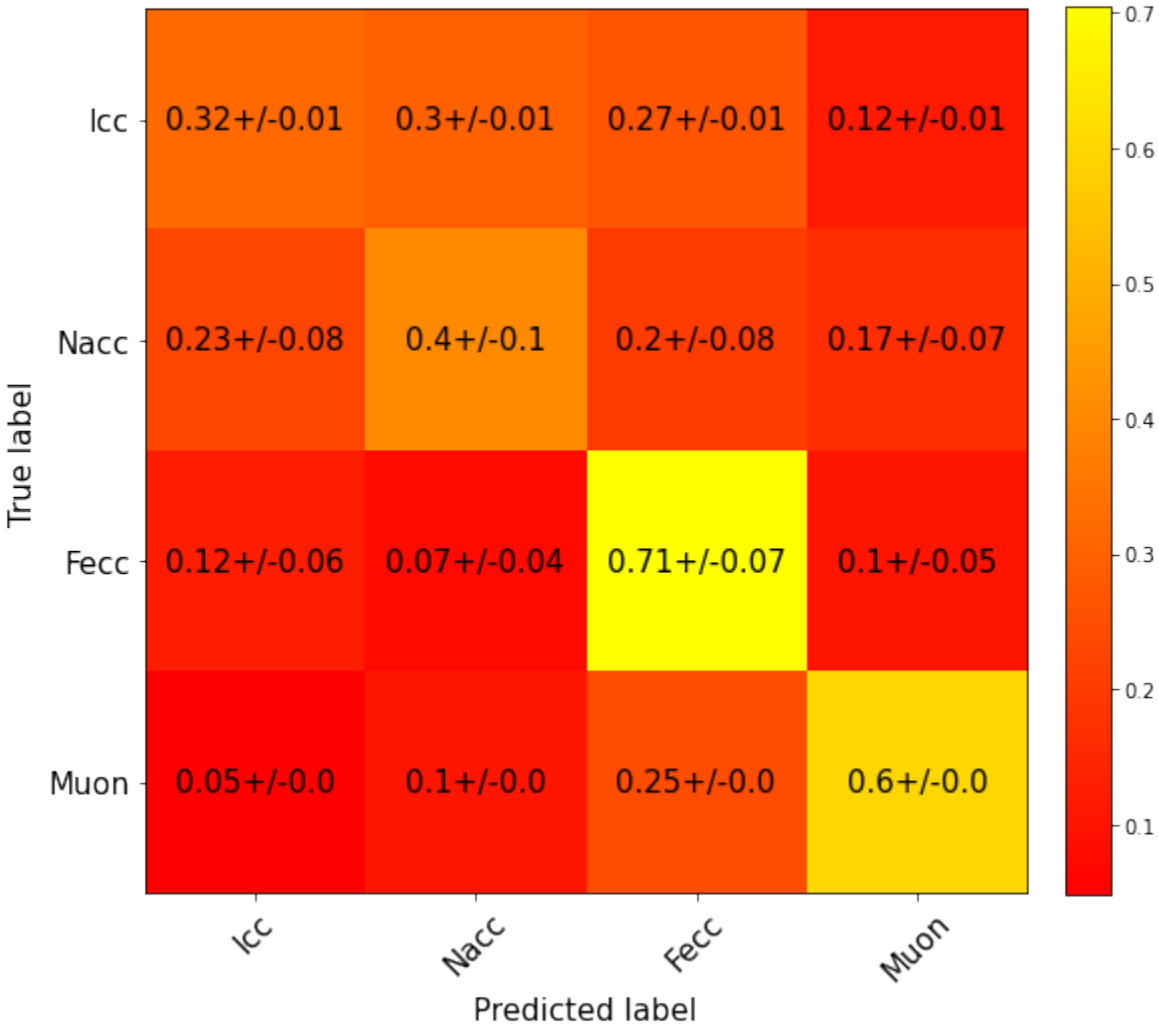

FIGURE 5.6: The confusion matrix of the XGBoost classifier normalized by the true label counts to represent recall with errors.

The model achieved a training accuracy of 53.7% and a validation accuracy of 50.2%. These numbers are low because there exist many low multiplicity events from each of the four classes that are extremely difficult to distinguish with available features. Lowering the number of classes included could improve the performance

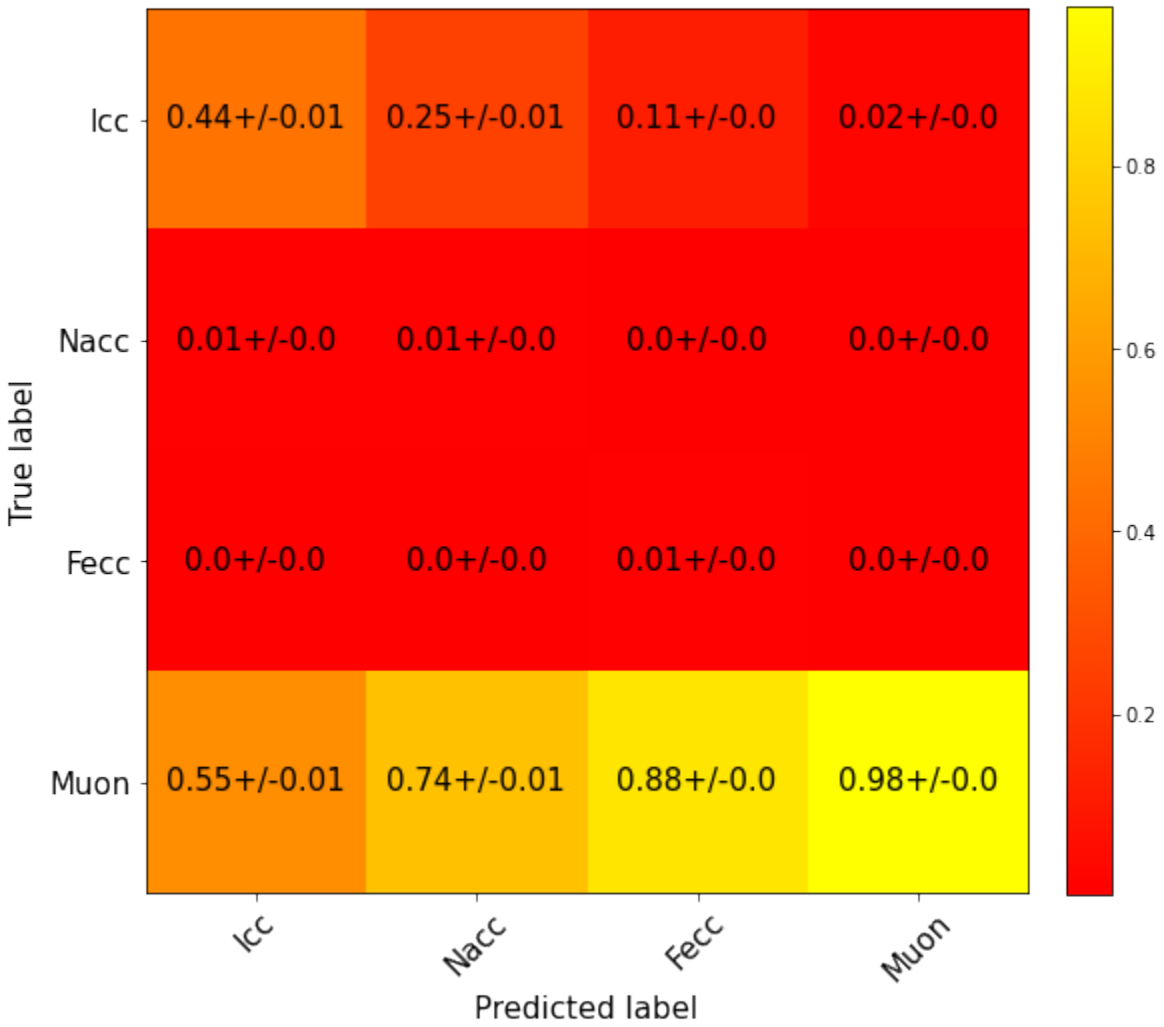

FIGURE 5.7: The confusion matrix of the XGBoost classifier normalized by the predicted label counts to represent precision with errors.

but it's important to include as many classes as possible because in future analyses we would be interested in potentially $^{23}\mathrm{Na}(\nu_e, e^-)^{23}\mathrm{Mg}$.

To get a better understanding of the model performance, we plotted the recall and precision matrices using 100 test sets, each of which contain the 4 classes with expected numbers shown in table 3.3, as shown in figure 5.6 and figure 5.7. From both figures, we can see that $^{127}\mathrm{I}(\nu_e, e^-)^{127}\mathrm{Xe}$ and $^{23}\mathrm{Na}(\nu_e, e^-)^{23}\mathrm{Mg}$ form a "cluster" and $^{56}\mathrm{Fe}(\nu_e, e^-)^{56}\mathrm{Co}$ and muons form another one. This makes sense from the topology

as the first two originated from within the NaI crystals while the other two from outside. As expected, muons have extremely high precision because they are the dominate class in the test set. Because the recall of muons is only about 60% for four classes with a 5% leak into the signal, the classifier failed to beat muon vetoes, whose performance are more consistent. However, combined with the muon veto, the classifier can further boost the signal-to-noise ratio, as the classifier correctly tags 32% of the signals while incorrectly tagging only 5% of the most dominant backgrounds as the signals. As a result, it would be interesting to see what the spectrum of the predicted signals look like from the data. Additionally, combining the precision and the recall of the signal and the counts of the predicted signal from the data could lead to a cross section measurement using machine learning.

6

High Energy Calibration

6.1 Motivation

To produce accurate measurements of the cross section of ν_e ^{127}I (p,n) ^{127}Xe, the low energy (keV) and high energy calibrations were performed separately. The high energy calibration was performed to account for the spectral non-linearity from the NaI crystals [75] and PMT saturation and errors that arise from extrapolating the low-energy calibrations to tens of MeV. The non-linearity was highlighted in figure 3.11 and 6.1. Since the high energy range (10-55 MeV) is way above the energy spectrum of any radioactive source accessible in a lab environment, another approach had to be explored. One concept was to construct a muon hodoscope spanning the prototype detector to compare the recorded muon energy to a muon simulation. However, because of Covid-19, most studies had to be done remotely. The Michel spectrum from stopped muon decays is a quality alternative for several reasons. Firstly the spectrum has been long studied and has well defined formulas, so it is easy to simulate. Also, the prototype detector is exposed to a large quantity of steady state muons each day and some of them will be stopped inside the detector. As a

result it is highly likely we will be able to observe their decay products. Lastly, this method does not incur additional costs, as it only requires algorithm developments.

The general calibration process involves:

- Search for Michel events in the blinded data.
- Generate simulations from the known Michel spectrum.
- Propose a theoretical mapping function.
- Use Markov Chains Monte Carlo to reconstruct the distribution of the scaling factor(s).
- Sanity checks on fitting and parameter choices.
- Locate the median, 16th and 84th percentiles of the distribution for each detector channel.

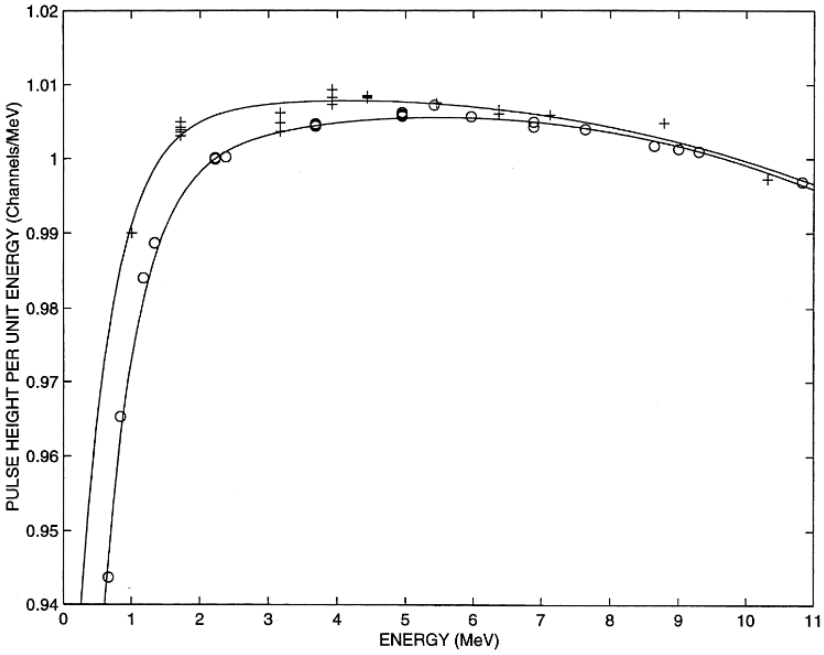

FIGURE 6.1: Measured NaI nonlinearity [75].

6.2 Michel Spectrum

Muons and anti-muons are unstable elementary particles with a mean lifetime of 2.1969811 ± 0.0000022 μs [103]. Due to the negative charge muons possess, they are more likely to be captured by heavy nuclei and could have a smaller lifetime in certain materials compared to anti-muons. Muons/anti-muons decay via the weak interaction into electrons/positrons, anti-electron neutrinos/electron neutrinos and muon neutrinos/anti-muon neutrinos. The muon decay process is shown in figure 6.2. The decay distribution of the electron/positron per unit energy is described in equation 6.1 [104, 105], neglecting $\frac{m_e^2}{m_\mu^2}$ and $\mathcal{O}(\alpha^2)$ terms [106]:

$$\frac{dP}{dE} = \frac{1}{N}\left(3x^2 - 2x^3 + \frac{\alpha}{2\pi}f(x)\right)$$
$$x = \frac{2E_e}{m_\mu} \qquad 0 < x \leq 1 \tag{6.1}$$

where N is the normalization factor, α is the fine-structure constant and $\frac{\alpha}{2\pi}f(x)$ represents a $\mathcal{O}(\alpha)$ radiative correction. The function $f(x)$ is described in equation 6.2 where $\mathrm{Li}_2(x)$ is the polylogarithm function [104, 107]:

$$\begin{aligned} f(x) = &\left[\frac{5}{3x^2} + \frac{16x}{3} + \frac{4}{x} + (12 - 8x)\ln\left(\frac{1-x}{x}\right) - 8\right] \\ &\times \ln\left(\frac{m_\mu}{m_e}\right) + (6 - 4x)\left[2\mathrm{Li}_2(x) - 2\ln^2(x) + \ln(x)\right. \\ &\left. + \ln(1-x)\left(3\ln(x) - \frac{1}{x} - 1\right) - \frac{\pi^2}{3} - 2\right] \\ &+ \frac{(1-x)[34x^2 + (5 - 34x^2 + 17x)\ln(x) - 22x]}{3x^2} \\ &+ 6(1-x)\ln(x) \end{aligned} \tag{6.2}$$

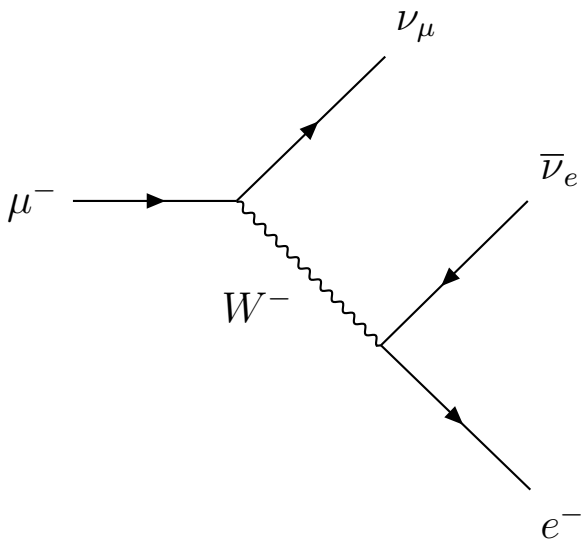

FIGURE 6.2: Feynman diagram of mu- decay.

As shown in figure 6.3, the radiative correction modifies mainly the region where $E_e > 40$MeV in the spectrum. The first term in equation 6.2 dominates because the $\ln\left(\frac{m_\mu}{m_e}\right)$ multiplication is large and $0 < x \leq 1$. However, these terms vanish after the energy integration due to the Kinoshita-Lee-Nauenberg (KLN) theorem [108, 109]. This is also reflected in figure 6.3, as the normalization constants are extremely close for the blue and black curves (they are not identical due to python float precision).

If steady state muons or anti-muons lose all their energies in our prototype detector, in theory, they could be stopped within the detector and start the decay process, from which electrons or positrons produced can be detected. However, the rate of such events will be low. More details of a searching approach within the blinded data will be described in the next section.

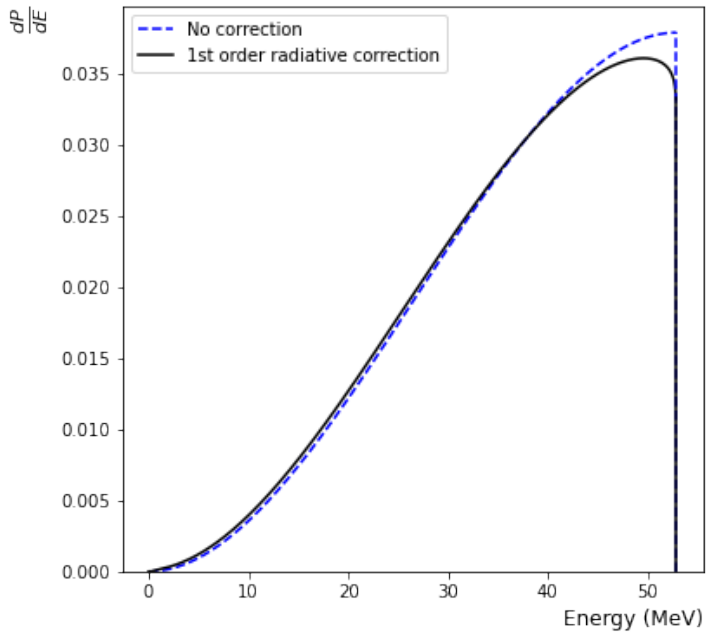

FIGURE 6.3: Michel spectrum with and w/o the first order radiative correction, neglecting $\frac{m_e^2}{m_\mu^2}$ and $\mathcal{O}(\alpha^2)$ terms.

6.3 Search Process

The Michel event search is crucial because if we are not able to record them in our detector, it will be impossible for us to implement this calibration technique. As mentioned in earlier chapters, muon flags from muon vetoes are available in the data. Hence, all we have to do is to select events with certain time offset after each muon event. The selection criteria used are listed below:

- The event has no PMT saturation.
- The particle event has a multiplicity of one.
- The event has an energy in between the low end cut, 10 MeV and the PMT saturation level, 55 MeV.
- The event has no muon veto flag coincidence.

- The detector cell that contains the energy of such event was part of a muon event.
- The event has a time to previous muon of 10 μs or larger.

The idea is to calibrate each detector cell individually so we only care about single detector events, which by definition deposit all their energies in a single detector cell. The 10 MeV low end cut is chosen to remove backgrounds below 10 MeV such as alphas and 511 keV gammas. To make sure that we are selecting Michel events, the electrons or positrons of interest must not be muons that trigger the muon vetoes to begin with. Additionally, the Michel electron or positron has to deposit its energy in one of the detector cells that are triggered by the previous muon. Finally, due to the 10 μs channel deadtime mentioned in earlier chapters, we only look at events that are at least 10 μs away from the previous muon. Given the 10 μs delay, we expect most muons to be already captured by iodine nuclei and anti-muons to dominate.

As shown in figure 6.4, the selection rules above result in putative Michel events (red) whose fitted mean lifetime is 2.201±0.015 μs plus backgrounds (blue). Since the mean lifetime of a muon is within the range of the fitted errors, these events are highly likely to be Michel events. From the 22.8 GWhr blinded data set taken by the prototype detector NaIνE-185, there are about 78,367±339 Michel events and 17,301±205 background events from 23 channels combined. As mentioned in chapter 3, channel 14 was treated as a passive volume due to the large amount of noise present in it. Figure 6.5 shows the same events as figure 6.4 but with a wider time range (10 μs to 100 μs). It is clear that the backgrounds are rather constant within this time range. Based on the fit result, the background events are defined as the events with a time to previous muon larger than 30 μs. In the actual calibration analysis, each channel will be treated individually. Figure 6.4 and 6.5 are only for demonstrations.

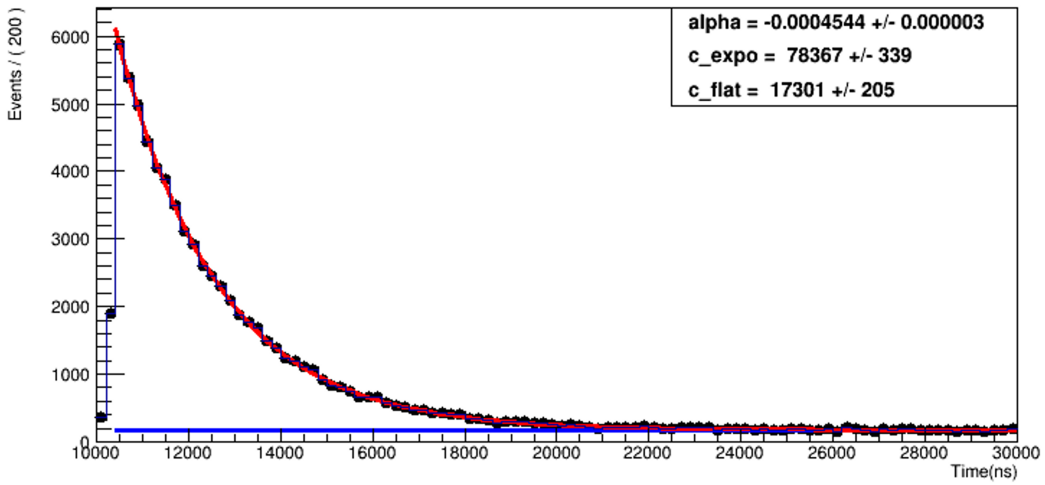

FIGURE 6.4: Putative Michel events plus backgrounds selected from 22.8 GWhr blinded data set taken by the prototype detector (23 channels aggregated). The red decay curve represents putative Michel events plus backgrounds and the blue flat curve represents just backgrounds.The corresponding mean lifetime of the decay constant alpha is 2.201±0.015 μs.

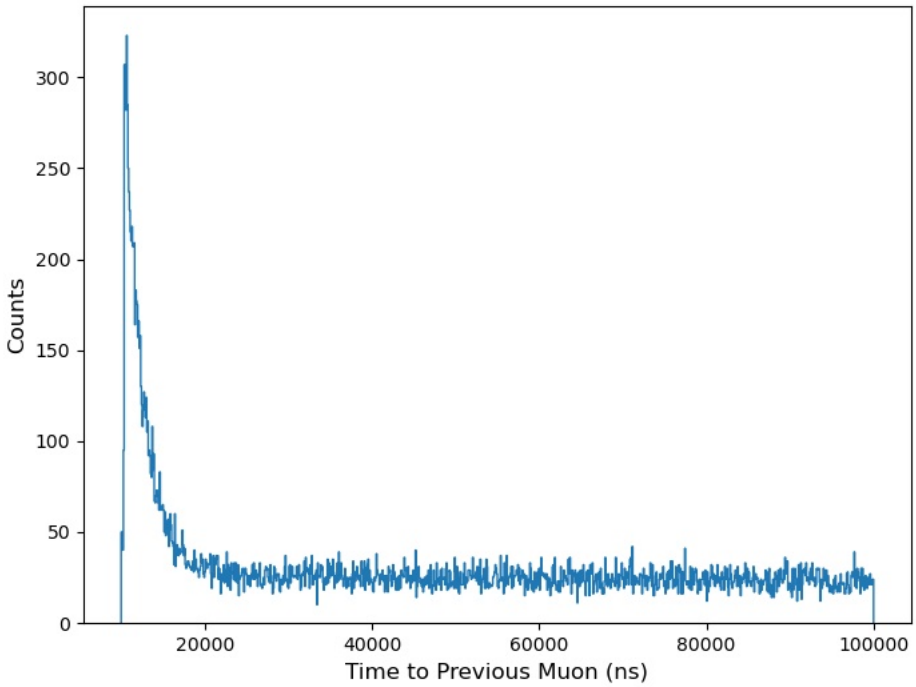

FIGURE 6.5: Putative Michel events plus backgrounds with a wider time range (10μs to 100μs).

6.4 Simulation

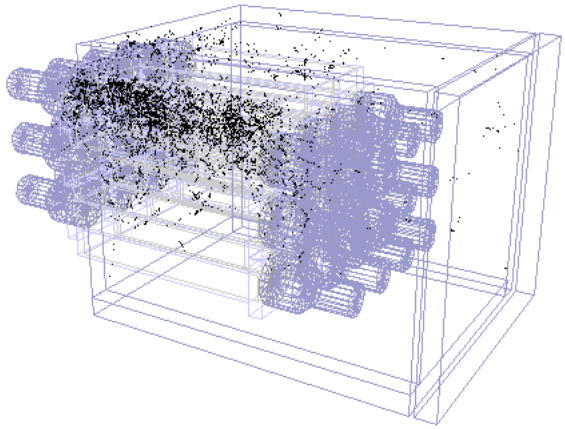

FIGURE 6.6: Simplified geometry of the NaIνe detector excluding muon vetoes and the neutrino alley. The black dots represent simulated Michel events.

The simulation of Michel events is performed with GEARS[1], a Geant4 based application developed by Dr. Jing Liu from University of South Dakota. The underlying concept is to provide a spectrum to the Geant4 particle source and choose the physics list (shielding) and detector geometry for the interactions. The spectrum is based on equation 6.1 with the radiative corrections. The simulation is done channel-wise and all Michel electrons/positrons are initialized in a random position within each channel. The chosen physics list is the $QGSP\_BERT$[2] physics list. Because there are only leptons in the simulation input and this list has good efficiency in computational power and storage. The detector geometry used is a simplified version of the prototype detector, in which only 24 detector channels and the steel

[1] https://github.com/jintonic/gears

[2] https://geant4.web.cern.ch/node/155

plates are present, as shown in figure 6.6. The justification is that the effects of the muon vetoes or the rest of the background objects like the hallway do not play significant roles in such a simulation setup. A less complicated geometry also reduces the computational load of post-processing and Markov Chain Monte Carlo (MCMC) fitting.

6.4.1 μ Capture

In NaI crystals, muons can be captured by the protons within the iodine or sodium nuclei (the former has a much higher probability). The capture process can described as:

$$\mu^- + p \rightarrow n + \nu_\mu \tag{6.3}$$

Since as described in the previous section the Michel events we can observe will be at least 10 μs away from the corresponding muon trigger, it is crucial to check if the source of the Michel events are muons, or anti-muons or both. This information determines if it is the electron that needs to be simulated or the positron.

To check the capture rate of muons and anti-muons, two simulations were performed. In the simulations, the only variable is the particle type, muon or anti-muon, and everything else is the same. A fixed number of muons/anti-muons are initialized in a random position within one detector channel with 0 MeV kinetic energy. Then for muons, the capture rate can be extracted from the distribution of the Geant4 global emerging time of produced nuclei. For anti-muons, the decay constant can be extracted from the distribution of the Geant4 global emerging time of anti-muon neutrino. To extract both numbers, RooFit[3] was used. Since the only parameter of interest is global time, no post processing on energies was applied, such as smearing or quenching. As shown in figure 6.7, the mean lifetime of anti-muons in a NaI

[3] https://root.cern/manual/roofit/

channel sits in the range of the fit result while due to capturing, the mean lifetime of muons is much smaller than the theoretical/vacuum value. The decay constant of muon capture from the fit matches the decay constant of muon capture on iodine from T. Suzuki et al. [110]. As shown by the simulation result, most muons will be captured by iodine nuclei (some by sodium) so after 10 μs anti-muon decay will dominate.

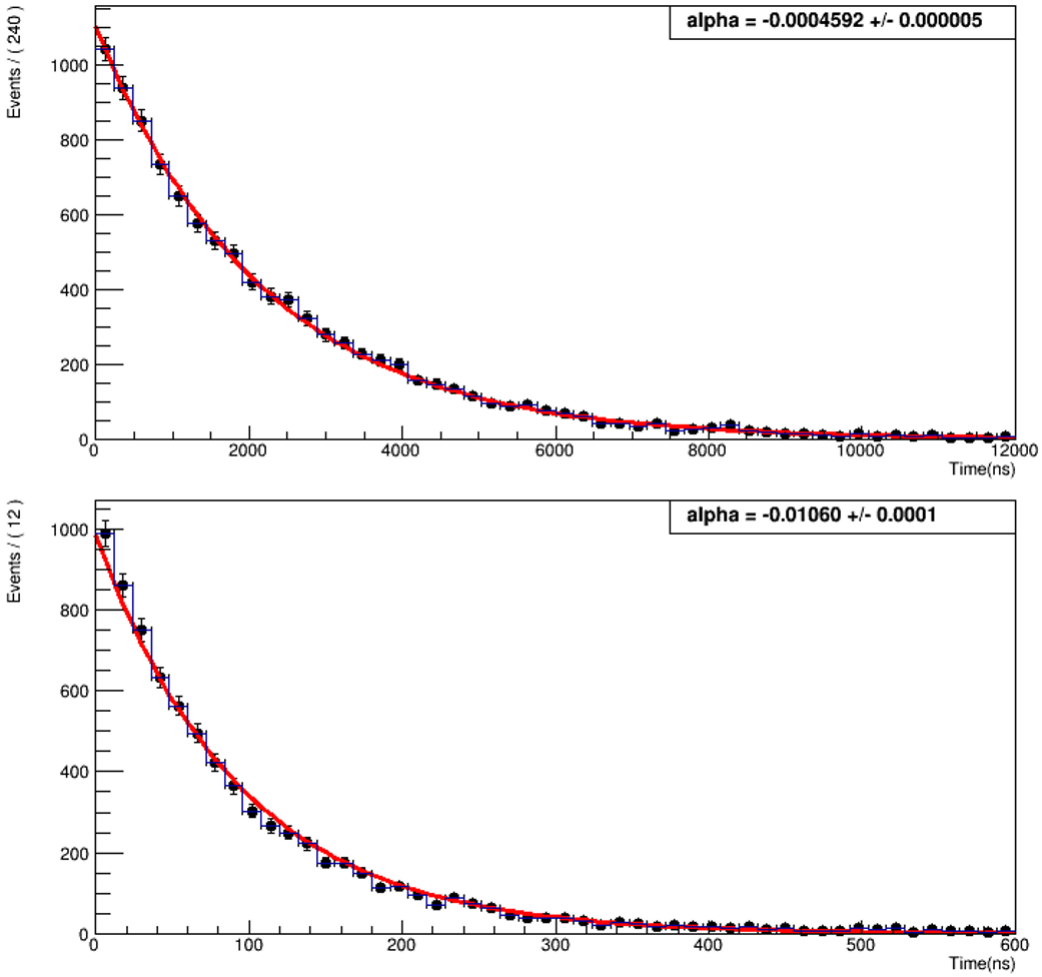

FIGURE 6.7: Top: anti-muon decay chart with a mean lifetime of 2.178±0.024 μs from the binned maximum likelihood fit result(red). Bottom: muon capture chart with a decay constant of 0.01060±0.0001 from the binned maximum likelihood fit result(red).

6.4.2 Michel Positrons

As explained from the previous subsection, Michel positrons were chosen as the simulation source. No decay process was simulated, as the same number of Michel positrons were directly initialized from a source spectrum shown in figure 6.3 (black) at random locations within each NaI crystal. The same energy treatment was applied as with the other simulations mentioned in earlier chapters. Figure 6.8 shows that the distribution of single detector Michel positron simulations in each of the 23 channel is right skewed with a peak around 16 MeV. The cutoff at the left end is due to the 900 keV hardware threshold. The 23 channels form 4 different groups in terms of the counts. Figure 6.9 provides more insights on the clustering of counts. The channels at the corner have more single detector events because positrons can fly away without interacting in another channel. The 4 different clusters correspond to the channels at the corners, the channels at the left and right edge, the channels at the top and bottom edge and the inner channels.

6.5 Markov Chain Monte Carlo

The models behind many problems in particle and nuclear physics are often expensive to compute, given the large number of parameters and low number of observations. In the case of Michel calibrations, the posterior PDF of the scaling constant(s) we want to sample can be described as:

$$p(k|x) = \frac{p(x|k)p(k)}{\int f(x|k)dk} \tag{6.4}$$

where k is the scaling constant(s), x is the data, $p(k)$ is the prior and the denominator is called the normalizing constant. This normalizing constant cannot be computed easily and precisely. To address this problem, Markov Chain Monte Carlo (MCMC) was used. MCMC has proven itself useful in providing sampling approximations

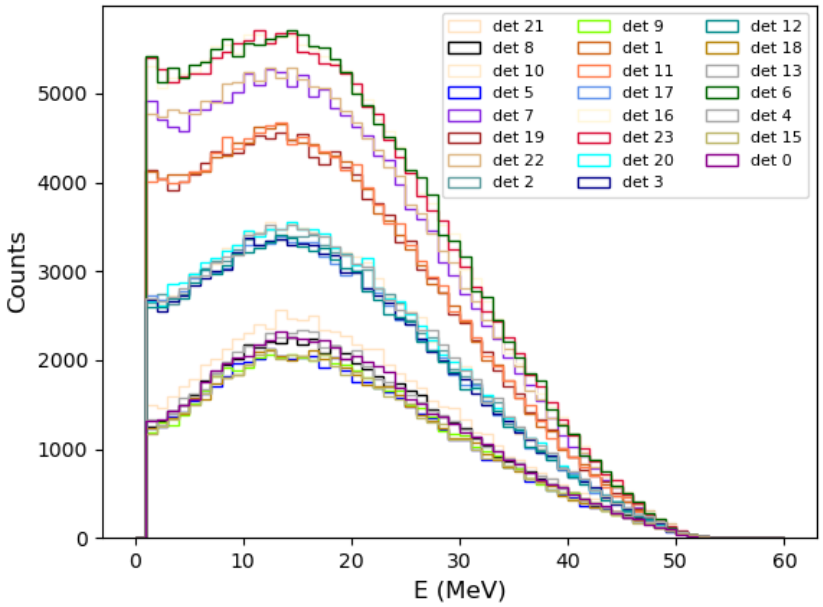

FIGURE 6.8: Single detector Michel events simulation in each of the 23 channels.

to the posterior PDF efficiently even with a large number of parameters in many research applications [111]. A good example comes from the results from the NASA Wilkinson Microwave Anisotropy Probe (WMAP) cosmology mission [112]. The goal is to use MCMC to generate N samples of k and then the marginalized constraints on k can be approximated by the histogram of the samples projected into the parameter subspace spanned by k [111]. For example, the expectation of k can be described as:

$$\mathbb{E}(k|x) \approx \frac{1}{N} \sum k_n \tag{6.5}$$

A Markov Chain is a stochastic process in which the probability of each event only depends on the state attained in the previous event. MCMC is then a procedure for generating an ensemble of Markov Chains in the parameter space, whose equilibrium distribution approximates the desired distribution. There are different methods to implement MCMC. One common option is to use the Metropolis-Hastings algorithm.

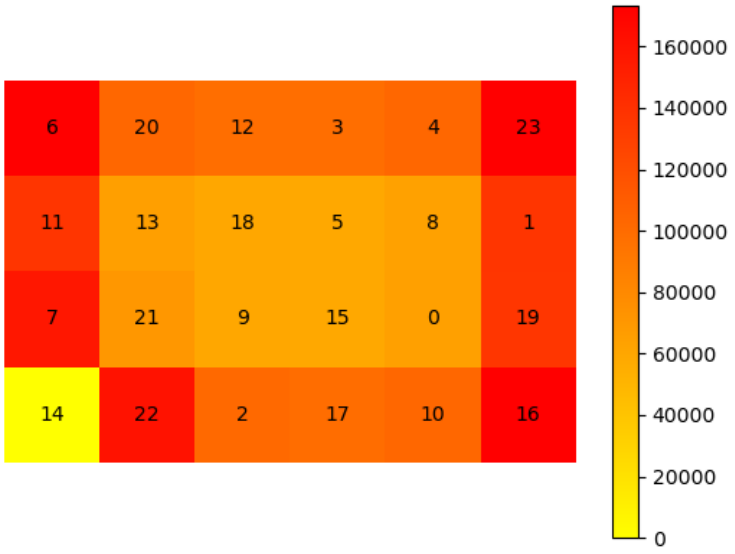

FIGURE 6.9: The number of single detector simulated Michel events in each of the 23 channels (channel 14 excluded). The channels are arranged in a way that reflects the top view of the actual setup. Colors represent counts while numbers represent channel id.

In short, each walker is initialized based on a given prior. Then in each step, a walker takes a sample from a candidate distribution with an acceptance rate determined by the ratio of the product of the posterior PDF and the PDF of the candidate distribution. Since only the ratio is needed, the exact value of the posterior is unnecessary. The actual package used for the calibration is EMCEE[4], which is based on an improved algorithm.

The sampling variance of equation 6.5 can be written as:

$$\sigma^2 = \frac{\tau}{N} \mathrm{Var}_{p(k|x)}[k] \tag{6.6}$$

where τ is the integrated autocorrelation time for the chain of k. Note that both equation 6.5 and 6.6 are simplified to suit this calibration work. In general, k is

[4] https://emcee.readthedocs.io/en/stable/

rather a function of k, $f(k)$ so τ is not unique for a given chain. The EMCEE manual gives a clear interpretation of τ: "In other words, $\frac{N}{\tau}$ is the effective number of samples and τ is the number of steps that are needed before the chain "forgets" where it started. This means that, if you can estimate τ, then you can estimate the number of samples that you need to generate to reduce the relative error on your target integral to (say) a few percent." In practice, it is best to remove certain multiple of τ samples from the MCMC output and apply thinning before analyze the distribution. EMCEE requires a $\frac{N}{\tau} > 50$ to give a good estimate of τ. For shorter chains, another approach is to apply an autoregressive model to the chain and do a maximum likelihood estimate on τ, as indicated in the EMCEE manual. As shown in figure 6.10, the machine learning approach gives good estimate even if the number of samples per chain is below 1000.

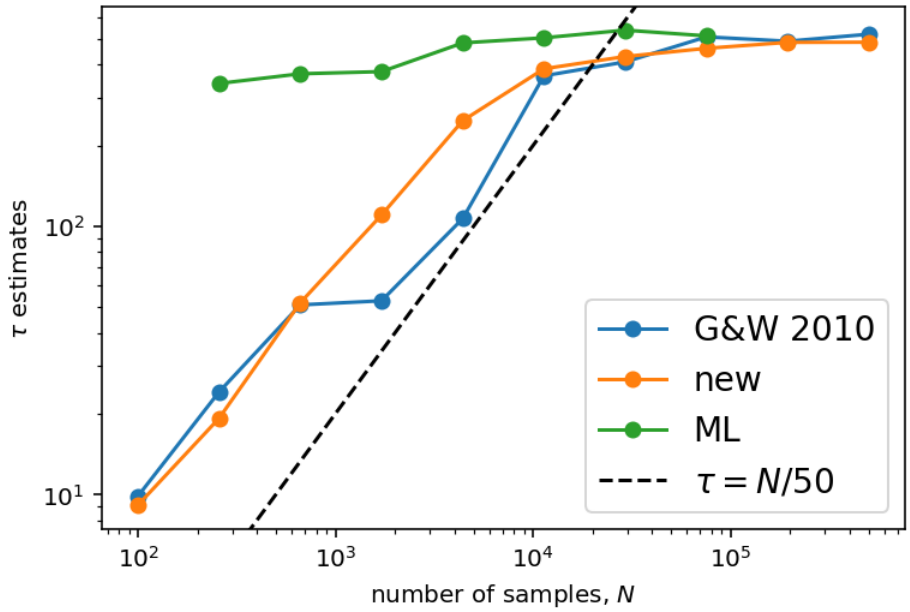

FIGURE 6.10: Effectiveness of τ estimate by different approaches from the EMCEE manual.

6.6 Calibration Analysis

6.6.1 Overview

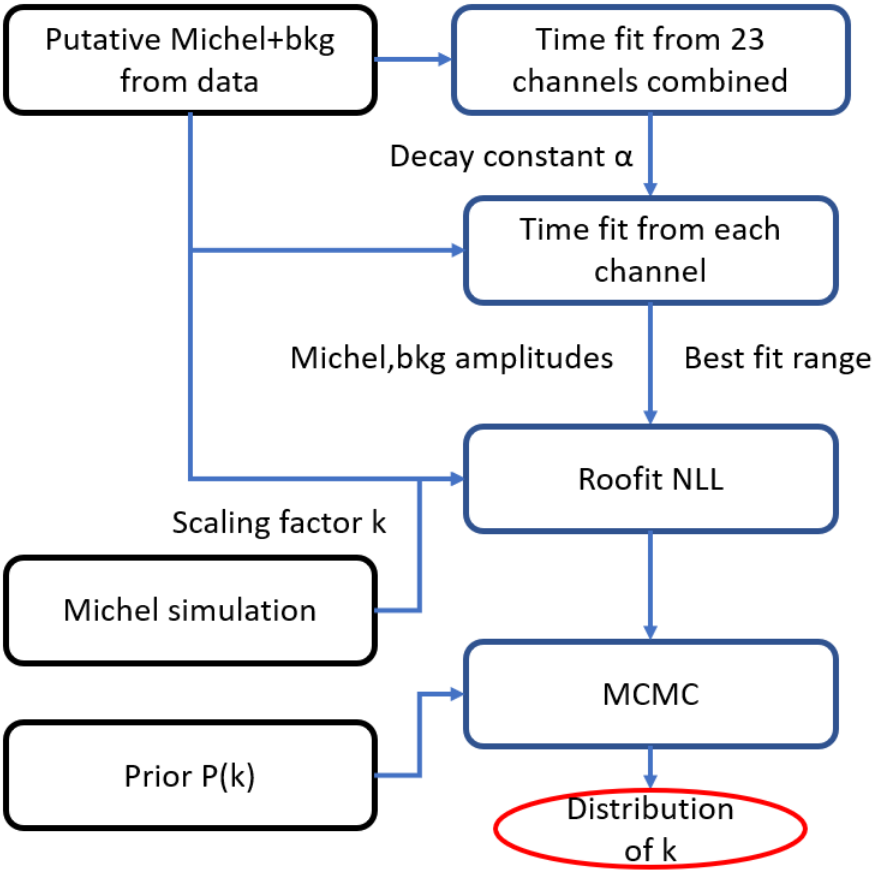

FIGURE 6.11: The workflow of the Michel calibration fitter.

Two mappings between the simulation (true value) and the data were tested. The first one assumes a linear relationship:

$$E_{data} = kE_{sim} \tag{6.7}$$

where E_{data} is the energy deposited in each channel by the putative events from the data, k is the scaling factor and E_{sim} is the energy deposited in each channel from the simulation. A linear mapping would affect the existing low energy calibrations

described in chapter 3, so the second mapping assumes a quadratic relationship, proposed by Dr. Sam Hedges:

$$E_{data} = kE_{sim}^2 + (1 - 4.075k)E_{sim} + 3.8179k \tag{6.8}$$

where $E_{data} = E_{sim}$ at 1.461 and 2.615 MeV, the ^{40}K and ^{208}Tl peak. Figure 6.11 demonstrates the workflow of the calibration fitter, whose goal is to retrieve the distribution of the scaling factor k for each channel.

6.6.2 Fitter Input

EMCEE takes a prior and a likelihood function as inputs. For the linear mapping, the prior is defined as:

$$0.75 < k < 1.25 \tag{6.9}$$

For the quadratic mapping, the prior is defined as:

$$k \geq -0.036 \tag{6.10}$$

The unbinned negative log likelihood function (NLL) used for both mappings is:

$$NLL = -\ln L(k) = -\ln \prod_{n}^{N} f(x_n, k) \tag{6.11}$$

where x_n is each of the N data points and $f(x_n, k)$ is the probability density function (PDF) or sometimes referred as $P(x_n|k)$. Unlike the user defined prior, the likelihood function is calculated through RooFit. For this work, RooFit takes the following input for NLL creation:

- Putative Michel events and background events from the data as x_n.
- Background PDF made from the background events from the data.
- Signal PDF made from the Michel simulation with a 10 MeV cut to accompany the data.

- Fixed amplitudes of the two PDF for the combined PDF.
- The scaling factor k that alters the signal PDF.

To acquire the two amplitudes for each channel, a combined PDF made of an exponential part and a flat part was fit to the time to previous muon distribution of the putative Michel + background events for all 23 channels aggregated first. As shown in figure 6.4, the decay constant α was acquired. Then a combined PDF, whose decay constant was fixed as α, was fit channel-wise. For each channel, the fitter searched for an optimal fit range, in which the sensitivity was maximized, and output the corresponding amplitudes of the two components of the combined PDF. The sensitivity is defined as:

$$s = \frac{C_{signal}}{\sqrt{C_{signal} + C_{background}}} \tag{6.12}$$

where C_{signal} is the number of signal/Michel events in the fit region given by the fit result and $C_{background}$ is the number of background events. Once the amplitudes were secured, the fitter produced a combined energy PDF with linear interpolation for each possible k value. Since the amplitudes were fixed for each channel, the NLL created by the combined energy PDF on the data was just a number instead of a function, given one k value. As a result, the product of the prior and the likelihood function is a function of k and satisfies the input requirement of EMCEE.

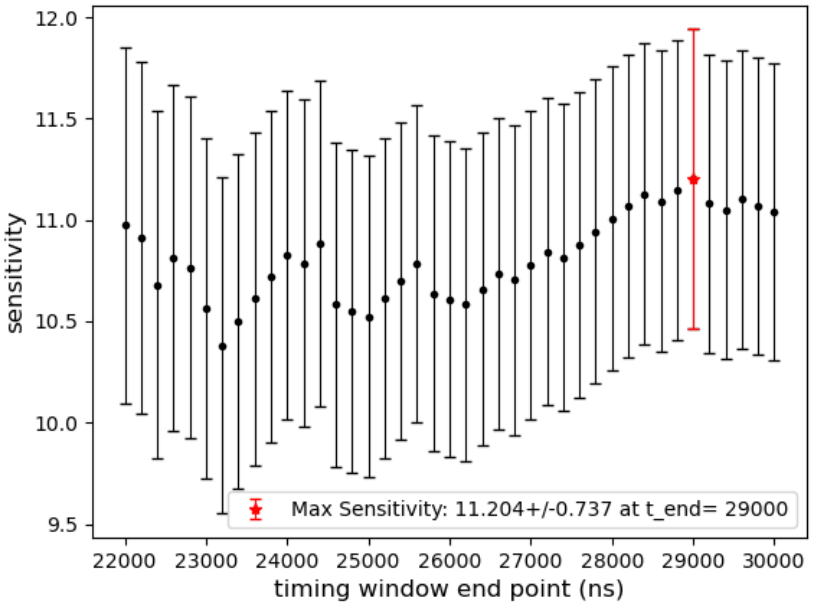

FIGURE 6.12: The sensitivity vs the right edge of the fitting range for channel 21.

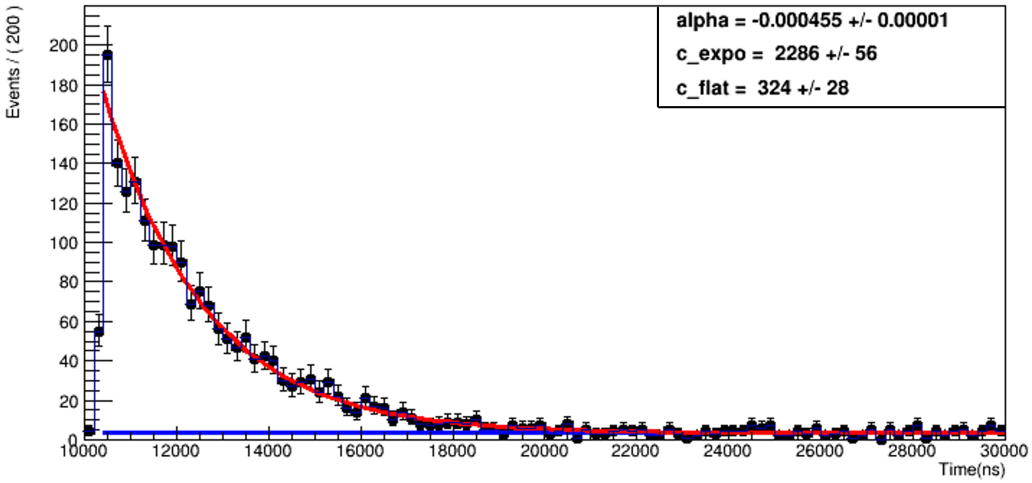

FIGURE 6.13: The fit to the time to previous muon of channel 21 in the best fit range. Red represents putative Michel events and blue is the background.

6.6.3 MCMC Tuning

As mentioned earlier, when evaluating the result of the EMCEE, it is crucial to find the value of τ for sample removal, in order to reduce the sampling error. The steps of the MCMC evaluation:

1. For each channel, run long chains (2500) with few walkers (2) only.
2. Use the EMCEE built-in function to calculate the τ value for each channel, which on average is below 35.
3. For each channel, run production chains with 2000 steps and 50 walkers.
4. Remove the first 100 steps from the samples of each walker.
5. Find the median of the distribution as the final k value for each channel, and the 16th and 84th percentiles as the 1 σ error.

In general, it's good to run long chains but it's not a good practice to generate too many samples. 50 walkers and 2000 steps already produced enough samples to reconstruct the distribution of the scaling factor. The function in EMCEE that calculates the τ value requires long chains to produce trustworthy results. To make the calculation efficient, only 2 walkers were chosen. Because EMCEE averages the τ value over all walkers, it is acceptable to get an estimate of τ using few walkers. The value of τ ranges from 20 to 35. To account for errors of τ estimation, the first 100 steps were removed from the samples of all channels. A thinning of 5 was also applied, which means that only one out of five consecutive samples were kept. The median of the distribution was chosen as the value of k and the (16th, 84th) percentile was chosen as the error bar, which corresponds to 1 σ.

6.6.4 Result

As shown in figure 6.14, the quadratic mapping (bottom) outperforms both the uncorrected data (top) and the linear mapping (middle), because the curves of the 23 channels are best aligned in the bottom subplot. As a result, the quadratic mapping would be used in the cross section analyses. Figure 6.15 shows the value of the quadratic mapping k for all 23 channels. This second order correction depends on the energy and are within 20% below 55 MeV. The size of the 1 σ error bars vary across different channels, possibly due to the nature of its channel's existing calibration and the number of data points available. Figure 6.16 and figure 6.17 demonstrates the trace plots and distribution plots of the samples of the quadratic mapping k from channel 16 and 21. The k distribution of channel 16 is much closer to a narrow peak normal distribution compared to that of channel 21. As a result, the error is smaller. The trace plots also show that the step removal along with thinning result in high quality samples. Figure 6.18 and 6.19 showcase the unbinned combined energy PDF fits using the quadratic mapping to putative Michel events plus backgrounds of channel 16 and 21. The Michel (green) PDF was generated from simulations and scaled through equation 6.7 with k sampled by EMCEE. The background PDF (blue) was made with the data. The total PDF (red) was the combination of the two based on the amplitudes from the timing fit, shown in the legend.

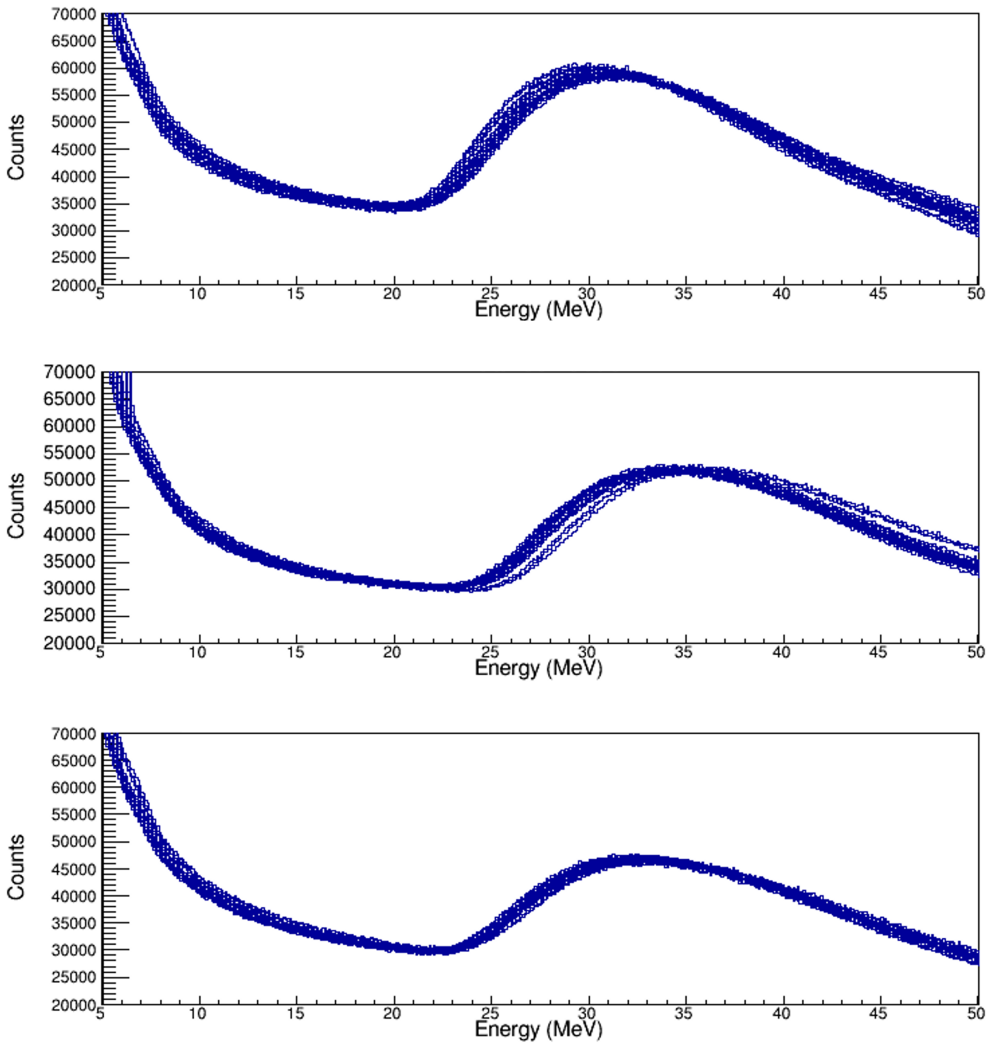

FIGURE 6.14: Comparisons between the linear mapping and the quadratic mapping applied to the blinded data (internal backgrounds of 23 channels plotted on top of each other), courtesy of Dr. Sam Hedges. From top to bottom: uncorrected data, linear mapping and quadratic mapping. The narrower the curves, the better aligned and calibrated.

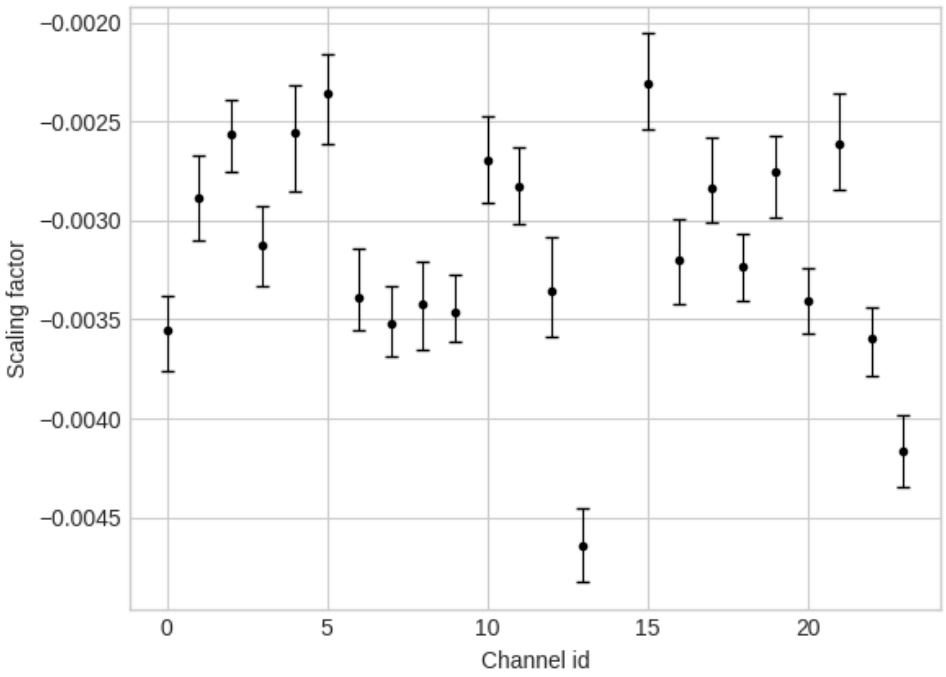

FIGURE 6.15: Scaling factor k of the quadratic mapping of all 23 channels with 1 σ error bars from EMCEE samples.

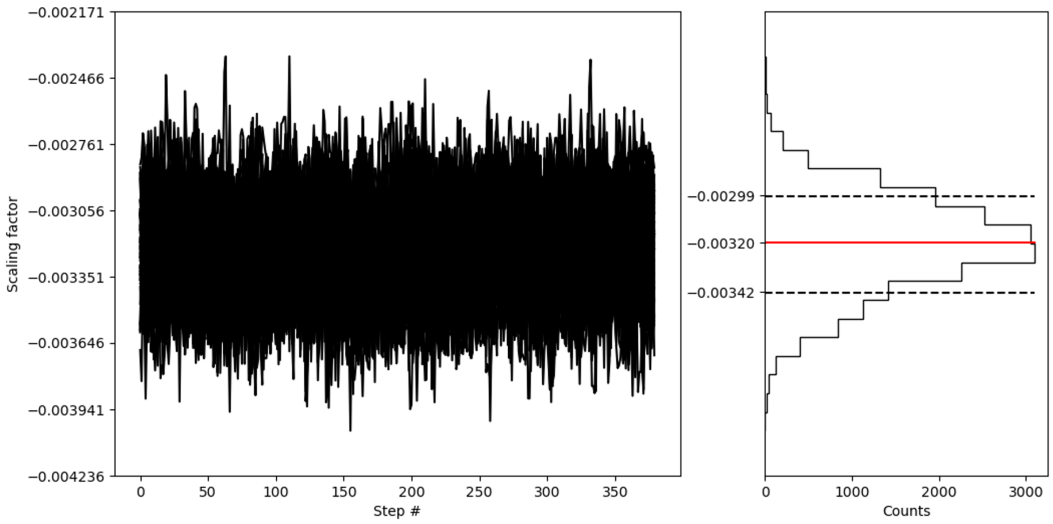

FIGURE 6.16: Left: the MCMC trace plots for channel 16 with the quadratic mapping. Right: the sample distribution with the median (red) and the 1 σ error bar (dash) after step removal and thinning for channel 16 with the quadratic mapping.

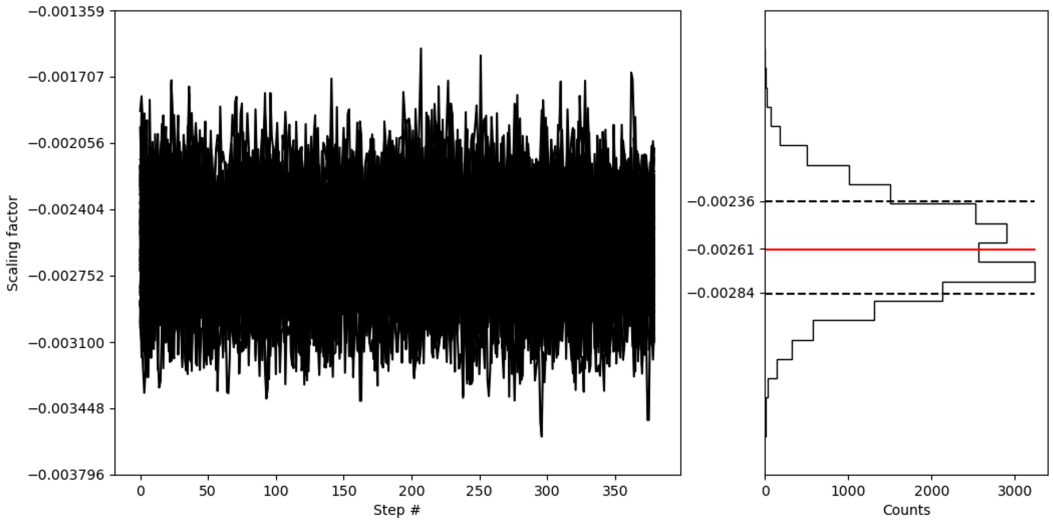

FIGURE 6.17: Left: the MCMC trace plots for channel 21 with the quadratic mapping. Right: the sample distribution with the median (red) and the 1 σ error bar (dash) after step removal and thinning for channel 21 with the quadratic mapping.

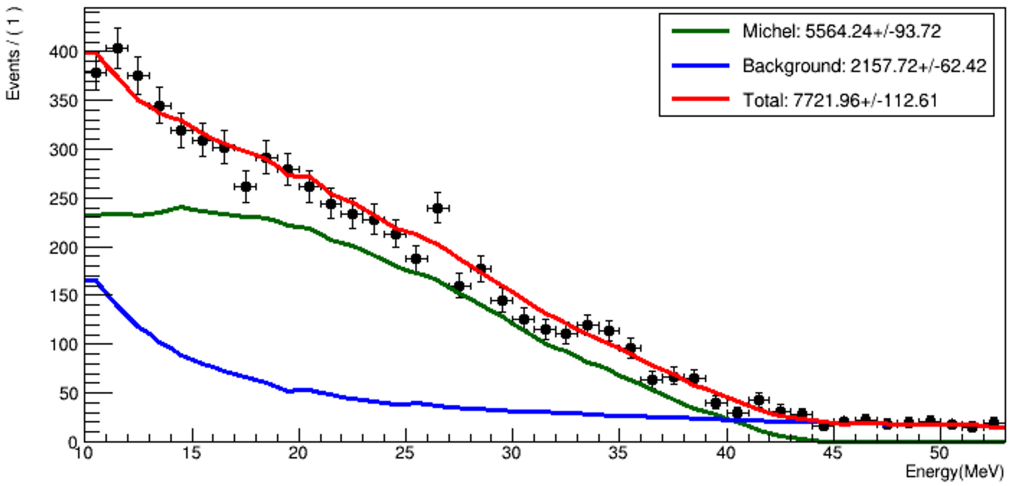

FIGURE 6.18: Unbinned energy PDF fits with with the quadratic mapping k from EMCEE samples to the data of channel 16.

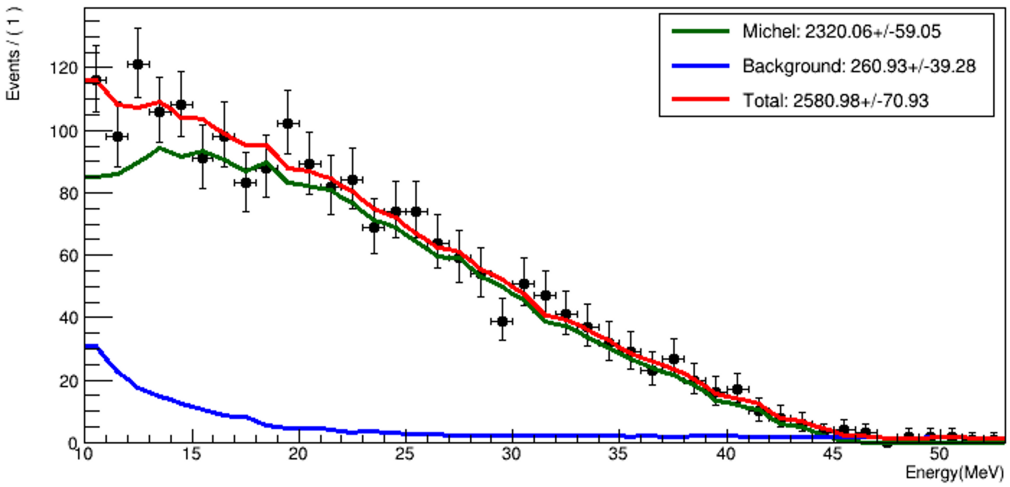

FIGURE 6.19: Unbinned energy PDF fits with with the quadratic mapping k from EMCEE samples to the data of channel 21.

7

Cross Section Analysis

7.1 PDF Construction

The work presented in this thesis has led to a measurement of the flux-averaged total cross section. The flux-averaged differential cross section, nucleon emission fractions and a finer BRN fit will follow. In the initial stage of the analyses (current), g_A is not expected to be extracted, as the effect of forbidden transitions could not be estimated due to its lack of appearance in the model. However, our data could still be valuable to theorists interested in studying g_A quenching. In the future stages, once we have a model that could handle forbidden transitions, we may extract g_A from out data. The cross section measurements rely on Probability Density Function (PDF) fitting, performed by Dr. Daniel Pershey. The energy and timing spectra of simulations of this work and steady state background data were converted into ROOT PDFs by Dr. Sam Hedges. The timing PDFs were convoluted with the SNS proton-on-target (POT) trace. The timing calculations were based on the result from the analyses of neutrino cubes [38]. The normalization of the PDFs was done by Dr. Sam Hedges and this author. The normalized counts are equal to the product of raw expected

Table 7.1: List of efficiencies at detecting $^{127}\mathrm{I}(\nu_e, e^-)^{127}\mathrm{Xe}$ signals, courtesy of Dr. Sam Hedges.

Origin	I-CC Eff	Na-CC Eff.	Fe-CC Eff.
Sim. (Geo. + thresh.)	0.990	0.971	0.118
Veto mis-ID	0.914	0.950	0.938
Energy & time ROI	0.862	0.885	0.192
Veto dead time	0.982	0.982	0.982
Pile-up flag	0.989	0.989	0.989
Total	0.757	0.793	0.021

counts and efficiencies. They were determined based on simulations and SNS beam-related calculations. The efficiencies, shown in table 7.1, took consideration of signal loss due to muon veto triggers or energy escaping the detectors, the 1 MeV threshold efficiency, the 10-55 MeV and 10 μs analysis window of interest, veto dead-time efficiency, and pile-up flag efficiency.

The systematic uncertainties of the normalization were mostly calculated by Dr. Sam Hedges and this author. The five types of uncertainties listed in table 7.2 are:

- Threshold Uncertainties: the errors on the selected 1 MeV threshold. The NaI detectors are believed to be at 100% trigger efficiency at 1 MeV, as very few events have energies lower than 1 MeV. It is important to understand how threshold variations would affect the signal rate. A threshold of 1.25 MeV, which is an extreme and rather unrealistic case, was applied. This new threshold decreased the expected signal rate in the 10-55 MeV region-of-interest by a only small amount.

- High Energy Calibration Uncertainties: the errors on the k parameter from the quadratic Michel positron calibration were tested. Their effects on the event rate in the 10-55 MeV window are negligible for $^{127}\mathrm{I}(\nu_e, e^-)^{127}\mathrm{Xe}$ and $^{23}\mathrm{Na}(\nu_e, e^-)^{23}\mathrm{Mg}$ (capped at 0.04%), but not for $^{56}\mathrm{Fe}(\nu_e, e^-)^{56}\mathrm{Co}$.

- Energy Resolution Uncertainties: the errors on the combined energy resolution function described in section 3.4.2 were tested. In the 10-55 MeV region, they have an impact of -0.0039% on the event rate of $^{127}\mathrm{I}(\nu_e, e^-)^{127}\mathrm{Xe}$ and -0.0039% on $^{23}\mathrm{Na}(\nu_e, e^-)^{23}\mathrm{Mg}$, and -0.0611% on $^{56}\mathrm{Fe}(\nu_e, e^-)^{56}\mathrm{Co}$. In an additional study by Dr. Sam Hedges, the combined energy resolution function was replaced with the channel-wise resolution functions. The resulted change in the event rates are all within the errors of the combined energy resolution function.

- Muon Veto Threshold Uncertainties: as described in section 4.7, veto triggers by the three types of charged-current interactions were simulated with three different veto thresholds: 300 keV, 500 keV and 700 keV. These thresholds were chosen to quantify the uncertainty on the actual veto threshold, as it is believed to be $\sim$500 keV, on the rising Compton edge of 511 keV gamma rays from the Hot Off-Gas Pipe[1]. This uncertainty has much larger impact on event rates than all the three types mentioned above.

- Neutrino Flux Uncertainties: the 10% uncertainty of the neutrino flux at he SNS [68] has the largest impact on the event rates.

Combining table 3.1, 7.1 and 7.2, we have the summary of expected counts of three types of charged-current events listed in table 7.3.

[1] The Hot Off-Gas Pipe is a pipe that runs through neutrino alley. It carries away radioactive gasses produced during beam operations.

Table 7.2: Total systematic uncertainty budget for the event rate predictions, added in quadrature, courtesy of Dr. Sam Hedges.

Quantity	I-CC Unc [%]	Na-CC Unc [%]	Fe-CC Unc [%]
Neutrino flux	±10.0	±10.0	±10.0
Trigger Efficiency	+0.0 -0.3	+0.0 -0.1	+0.0 -1.0
Calibration	+0.0 -0.0	+0.0 -0.0	+0.1 -0.3
Energy Resolution	+0.0 -0.0	+0.0 -0.0	+0.2 -0.2
Muon Veto Threshold	+2.8 -5.1	+1.1 -2.0	+2.0 -3.7
Total:	+10.4 -11.2	+10.1 -10.2	+10.2 -10.7

Table 7.3: Summary of expected counts of three types of charged-current events, courtesy of Dr. Sam Hedges.

Event Type	nTargets ($\times 10^{26}$)	MARLEY σ ($\times 10^{-40}$cm^2)	Eff.	Unc.(%)	Number
I-CC	7.4	22.5	0.757	+10.4-11.2	1320^{+148}_{-137}
Na-CC	7.4	0.5	0.793	+10.1-10.2	31^{+3}_{-3}
Fe-CC	50.0	2.9	0.021	+10.2-10.7	31^{+3}_{-3}

7.2 Expected Fits

The immediate measurement to be performed after the data is unblinded is the flux-averaged total cross section measurement, while the other three require further analyses. A 1D timing fit using the convoluted timing PDFs would be used so that the BRN and charged-current events could be separated. With the nominal MARLEY prediction, over 16 σ sensitivity to the $^{127}\mathrm{I}(\nu_e, e^-)^{127}\mathrm{Xe}$ signals are expected. As a result, more complicated fits are not necessary. The expected event rates are shown in figure 7.1. There are two parameters in the 1D timing fit: one that floats freely for the BRN normalization and one that uses the prediction as the prior for the steady state background normalization.

7.3 Sideband Unblinding Analysis

To test the fitter and improve normalization estimates, a low-energy analysis sideband (4-8 MeV) and a high-energy analysis sideband (55-100 MeV) of the blinded data were unblinded. There were several key findings, which provide valuable information to the ongoing cross section measurement:

- The measured BRN normalization is 6.2 times higher in the low-energy sideband and 9.9 times higher in the high-energy sideband. The scaling factors are

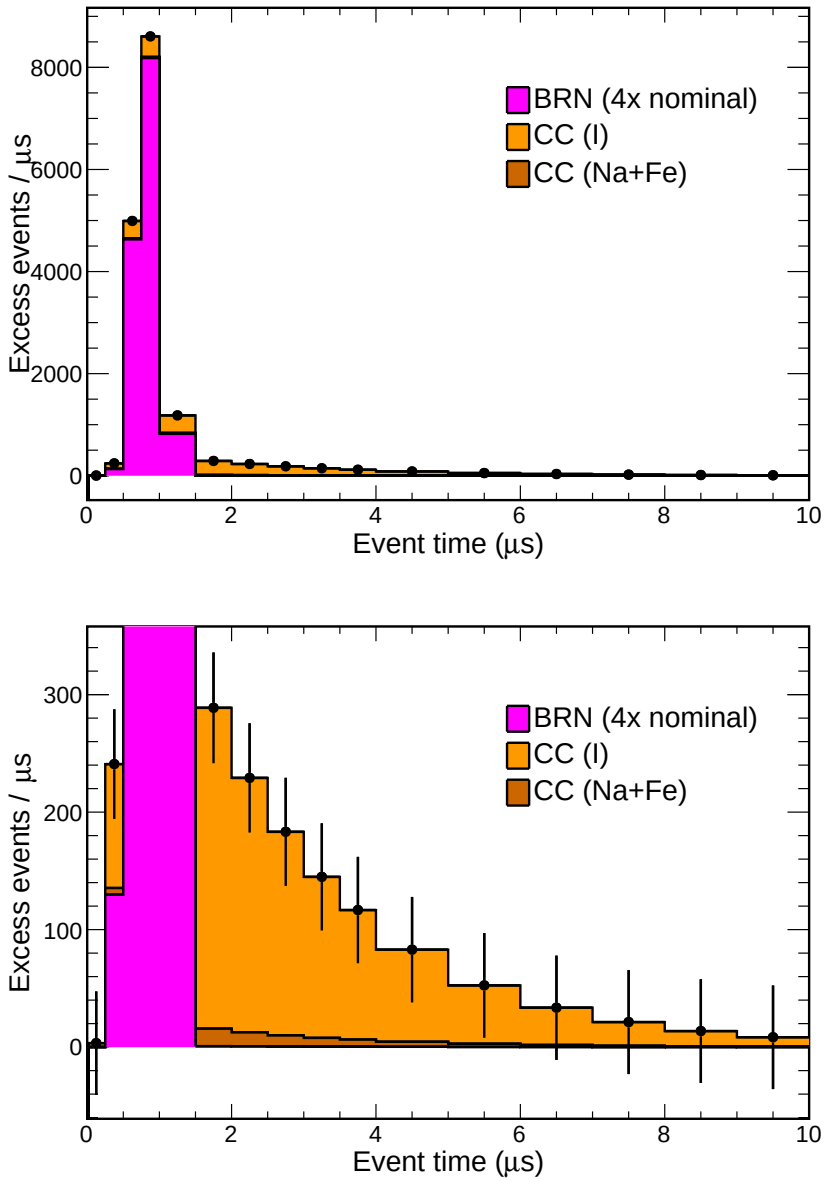

FIGURE 7.1: The expected beam excess of events as a function of event time, courtesy of Dr. Daniel Pershey. All events with observed energy are in the 10-55 MeV and 10 µs analysis window. The bottom chart is the zoomed-in view of the top chart.

not energy dependent. It's not clear whether flux or cross section mismodeling caused the discrepancy. To address this, for the sensitivity analysis, the BRN normalization used will be 8 times larger than the predicted value.

- The measured t_0, the event starting time (0 in the prediction), is -17 ± 5 ns for the low-energy sideband and -70 ± 4 ns for the high-energy sideband. These discrepancies are not surprising because the in the prediction the timing PDFs were constructed based on the timing information from neutrino cubes. They suggest that the low energy excess is produced by a population of lower energy neutrons that arrive at the detector later. Additional time broadening was also observed: 33 ± 9 ns for the low-energy sideband and < 8 ns for the high-energy sideband. Together, the observations suggest that t_0 and time width both depend on energies.

- As shown in figure 7.2, self-shielding of BRNs in the NaIνE-185 was observed in both sidebands. This suggests that the BRNs are also coming from the right side of the detector along the hallway other than from the adjacent wall. Additional neutron shielding on the side could be useful for future experiments.

- As shown in figure 7.3, in the low-energy sideband, a roll-off near 6.5 MeV, the energy of the iodine capture gamma emission, was observed. Additionally, the distribution plateaus at lower energies. However, in the simulation, the energies between 4 and 8 MeV are peaked at 6.5 MeV. This further proves that GEANT4 can only simulate one properly: the total calorimetric energy of released gammas in a capture or the individual cascade energies.

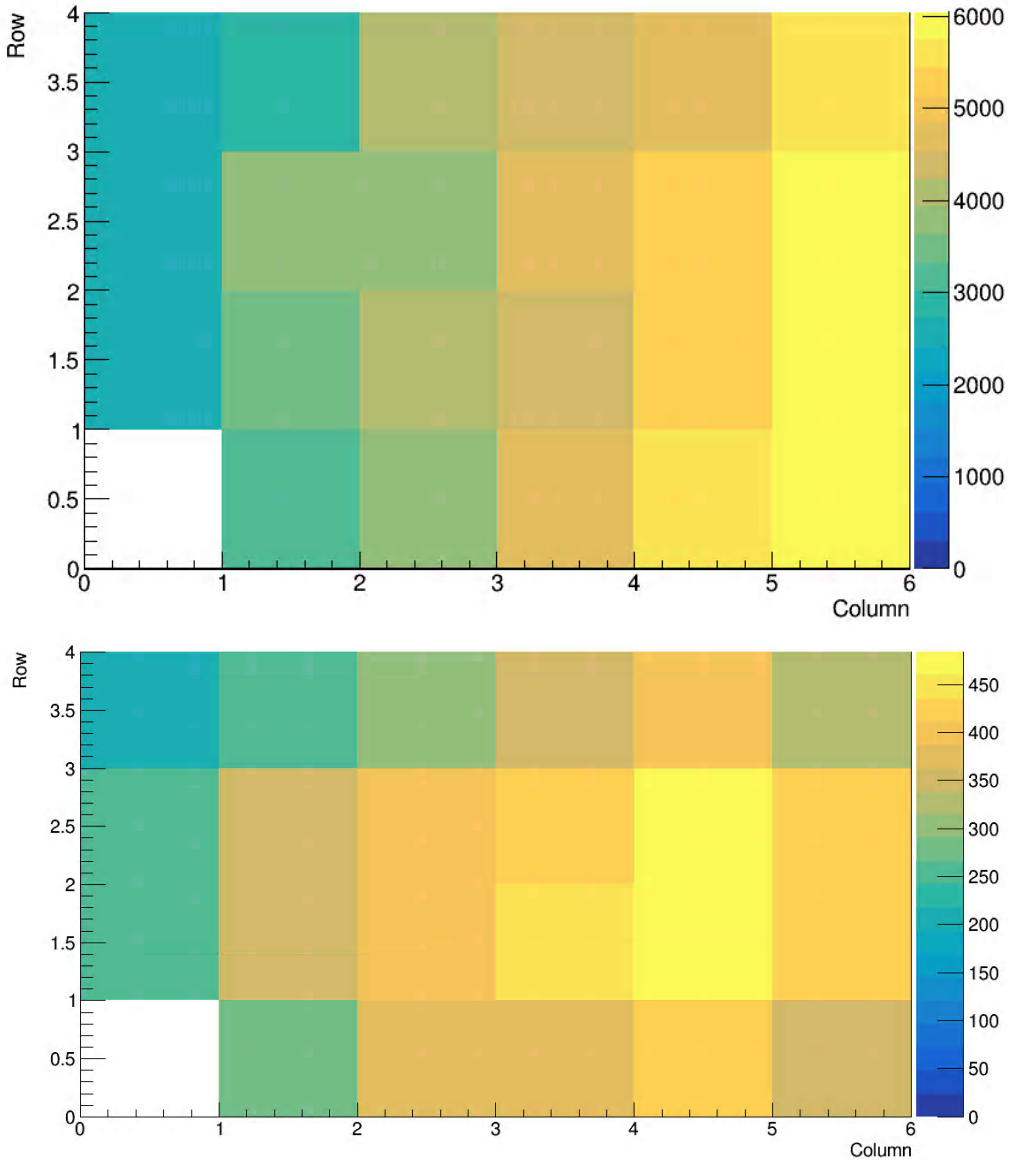

FIGURE 7.2: The multiplicity of detectors hit by neutrons in the low-energy (top) and high-energy (bottom) sidebands, courtesy of Dr. Sam Hedges.

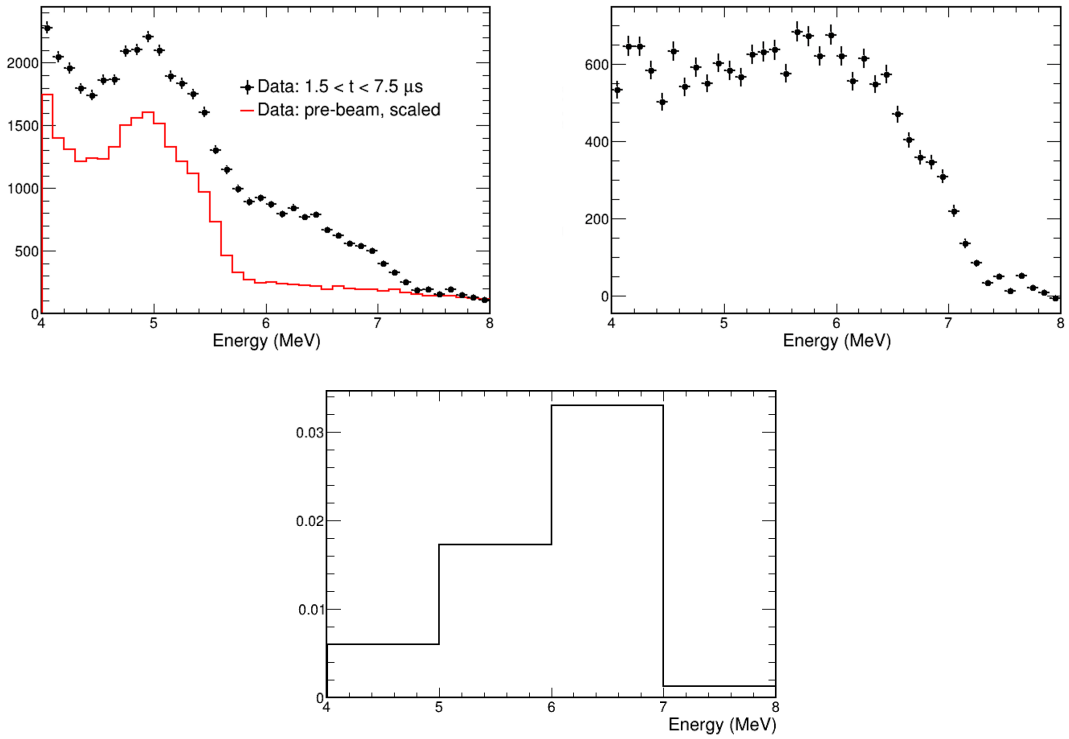

FIGURE 7.3: Top left: the histogram showing the observed data in the tail timing window compared to the pre-beam data appropriately scaled in the low-energy sideband. Top right: the histogram showing the beam excess in the tail window showing capture energies in the low-energy sideband. A roll off is observed beyond the 6.5 MeV capture energy in the region where it is expected. Bottom: the normalized histogram of the simulated capture energies for events in the same time and energy window. Simulation is peaked compared to the data, but both show the same roll-off above 7 MeV. All plots are courtesy of Dr. Daniel Pershey.

7.4 Flux-averaged Total Cross Section

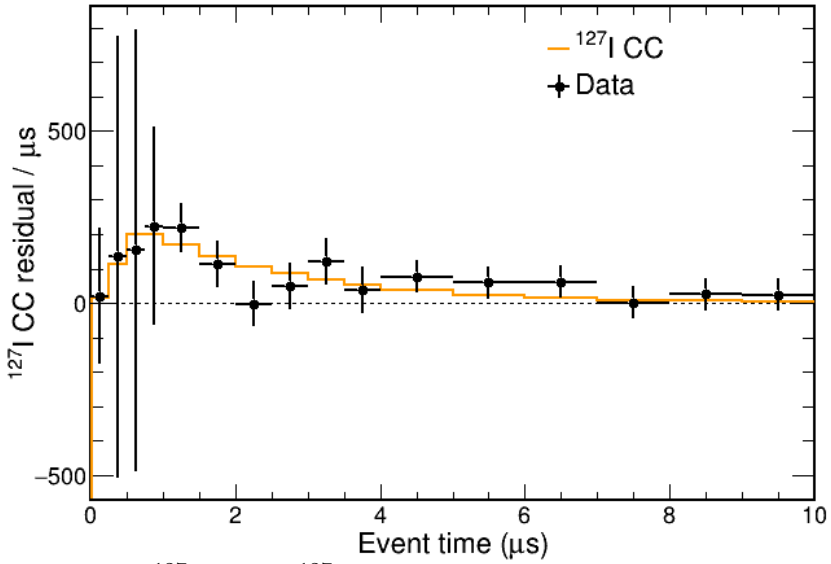

FIGURE 7.4: The $^{127}\mathrm{I}(\nu_e, e^-)^{127}\mathrm{Xe}$ signal residuals (background subtracted) as a function of event time made with the 22.8 GWhr unblinded data, courtesy of Dr. Daniel Pershey. All events with observed energy are in the 10-55 MeV and 10 μs analysis window.

After opening the box, Dr. Daniel Pershey performed a 1D timing fit on the unblinded data. The fitter returned $(541 + 121 - 108)$ $^{127}\mathrm{I}(\nu_e, e^-)^{127}\mathrm{Xe}$ events, rejecting the null hypothesis by 5.8 σ. Figure 7.4 demonstrates the signal residuals (background subtracted) as a function of event time. The measured number is about 41% of the expected value from MARLEY. This is equivalent to $g_A^{\mathrm{eff}} = 0.64 g_A$, neglecting forbidden transitions. The 41% scaling also caused the drop of the sensitivity from 16 σ to 5.8 σ. The flux-averaged total inclusive cross section was then calculated as:

$$\sigma_\Phi = \frac{N_{signal}}{\epsilon \times N_{target} \times \Phi} = (9.2 + 2.1 - 1.8) \times 10^{-40}\mathrm{cm}^2 \tag{7.1}$$

where $N_{signal} = 541 + 121 - 108$ is the number of signals or $^{127}\mathrm{I}(\nu_e, e^-)^{127}\mathrm{Xe}$ events, $\epsilon = 0.7572$ is the overall efficiency, $N_{target} = 7.432 \times 10^{26}$ is the number of ^{127}I targets

and $\Phi = 1.043 \times 10^{15} \nu/\text{cm}^{-2}$ is the neutrino flux at the SNS. All the uncertainties were incorporated in the fitter so the error bar on both the total cross section and the signal count contains both systematic and statistical errors.

As mentioned earlier, besides the flux-averaged total inclusive cross section, the differential cross section, nucleon emission fractions and BRN fits can also be extracted from the NaIνE-185 data in the future. The differential cross section would offer the opportunity to test different theoretical models that generate energy spectra. The nucleon emission fractions can be used to compare this result to the LAMPF measurement [1], in which only zero-neutron emission events were counted. The BRN fits would improve our understanding of the neutron background at the SNS and benefit all COHERENT experiments.

8

Conclusion

The work described in this thesis reflects efforts to measure the inclusive cross section of the electron neutrino charged-current interaction on ^{127}I for the first time ever, with a 185-kg NaI detector deployed at the SNS. A successful measurement would offer insights on the quenching of g_A, the axial-vector coupling constant, and in turn provide guidance to the design of future neutrinoless double beta decay experiments. Additionally, it would pave the way for the detection of solar neutrinos. The work described in this thesis also provides guidance for future simulations development and data analyses of the ton-scale NaI detector. In brief, this thesis presented:

- The design and analysis chain of the NaIνE-185 detector. See chapter 3.
- The design and results of the simulations performed using Geant4 and other particle event generators for the cross section measurement, such as MARLEY and CRY. See chapter 4.
- Two machine learning attempts for signal classification and background rejection with convolutional neural nets and XGBoost. See chapter 5.

- A high energy calibration done to the NaIνE-185 detector with Michel positrons to address non-linearity of the energy responses in the 1-55 MeV region. See chapter 6.

- The results of the analysis on the cross section measurement. See chapter 7.

In the analysis, $(541 + 121 - 108)$ $^{127}\mathrm{I}(\nu_e, e^-)^{127}\mathrm{Xe}$ events were measured rejecting the null hypothesis by 5.8 σ. The flux-averaged total inclusive cross section was calculated to be $[9.2 + 2.1 - 1.8\ (\mathrm{stat+syst})] \times 10^{-40}$ cm^2. A 41% scaling factor was observed from the expected number of events, 1320. This is equivalent to $g_A^{\mathrm{eff}} = 0.64 g_A$, neglecting forbidden transitions. Even though we could not extract the value of g_A in the initial stage of our analysis, our data could still be useful to theorists interested into g_A quenching. As shown in equation 1.1, the half-life of $0\nu\beta\beta$ decay depends on $(\frac{g_A^{\mathrm{eff}}}{g_A})^4$. As a result, our data could contribute significantly to the development of next generation detectors for $0\nu\beta\beta$ decay searches.

The efforts of the COHERENT collaboration towards neutrino charged-current interaction continue. There are more to be studied from the NaIνE-185 result, such as the differential cross section, the nucleon emission fractions and the BRN fits. In the near future, the inclusive cross section of the electron neutrino charged-current interaction on ^{23}Na could also be measured, with the ton-scale NaI detector deployed in the summer of 2022, which is expected to provide more stats.

Bibliography

[1] J. R. Distel, B. T. Cleveland, K. Lande, C. K. Lee, P. S. Wildenhain, G. E. Allen, and R. L. Burman. Measurement of the cross section for the reaction $^{127}\mathrm{I}(\nu_e, e^-)^{127}\mathrm{Xe}_{\text{bound states}}$ with neutrinos from the decay of stopped muons. *Phys. Rev. C*, 68:054613, Nov 2003.

[2] A. V. Pohm, R. C. Waddell, J. P. Powers, and E. N. Jensen. Beta spectrum of ^{14}C. *Phys. Rev.*, 97:432–433, Jan 1955.

[3] Carsten Jensen. *Controversy and consensus: nuclear beta decay 1911–1934*, volume 24. Springer, 2012.

[4] Jean Danysz. Recherches expérimentales sur les rayons β de la famille du radium. *Ann. Chim. Phys. 30*, pages 241–320, 1913.

[5] W Pauli. Letter of the 4th december 1930. *Pauli Archive at CERN*, 1930.

[6] Enrico Fermi. Versuch einer theorie der β-strahlen. i. *Zeitschrift für Physik*, 88(3):161–177, 1934.

[7] F. Reines and C. L. Cowan. Detection of the free neutrino. *Phys. Rev.*, 92:830–831, Nov 1953.

[8] Clyde L Cowan Jr, Frederick Reines, FB Harrison, HW Kruse, and AD McGuire. Detection of the free neutrino: a confirmation. *Science*, 124(3212):103–104, 1956.

[9] G. Danby, J-M. Gaillard, K. Goulianos, L. M. Lederman, N. Mistry, M. Schwartz, and J. Steinberger. Observation of high-energy neutrino reactions and the existence of two kinds of neutrinos. *Phys. Rev. Lett.*, 9:36–44, Jul 1962.

[10] Martin L Perl, GS Abrams, AM Boyarski, Martin Breidenbach, DD Briggs, F Bulos, William Chinowsky, JT Dakin, GJ Feldman, CE Friedberg, et al. Evidence for anomalous lepton production in $e^+ - e^-$ annihilation. *Physical Review Letters*, 35(22):1489, 1975.

[11] K Kodama, N Ushida, C Andreopoulos, N Saoulidou, G Tzanakos, P Yager, B Baller, D Boehnlein, Walter Freeman, B Lundberg, et al. Observation of tau neutrino interactions. *Physics Letters B*, 504(3):218–224, 2001.

[12] John N Bahcall and Raymond Davis Jr. Solar neutrinos: a scientific puzzle. *Science*, 191(4224):264–267, 1976.

[13] John N Bahcall. Solar neutrinos: Theory versus observation. *Space Science Reviews*, 24(2):227–251, 1979.

[14] Y. Fukuda, T. Hayakawa, E. Ichihara, K. Inoue, K. Ishihara, H. Ishino, Y. Itow, T. Kajita, J. Kameda, S. Kasuga, K. Kobayashi, Y. Kobayashi, Y. Koshio, M. Miura, M. Nakahata, S. Nakayama, A. Okada, K. Okumura, N. Sakurai, M. Shiozawa, Y. Suzuki, Y. Takeuchi, Y. Totsuka, S. Yamada, M. Earl, A. Habig, E. Kearns, M. D. Messier, K. Scholberg, J. L. Stone, L. R. Sulak, C. W. Walter, M. Goldhaber, T. Barszczxak, D. Casper, W. Gajewski, P. G. Halverson, J. Hsu, W. R. Kropp, L. R. Price, F. Reines, M. Smy, H. W. Sobel, M. R. Vagins, K. S. Ganezer, W. E. Keig, R. W. Ellsworth, S. Tasaka, J. W. Flanagan, A. Kibayashi, J. G. Learned, S. Matsuno, V. J. Stenger, D. Takemori, T. Ishii, J. Kanzaki, T. Kobayashi, S. Mine, K. Nakamura, K. Nishikawa, Y. Oyama, A. Sakai, M. Sakuda, O. Sasaki, S. Echigo, M. Kohama, A. T. Suzuki, T. J. Haines, E. Blaufuss, B. K. Kim, R. Sanford, R. Svoboda, M. L. Chen, Z. Conner, J. A. Goodman, G. W. Sullivan, J. Hill, C. K. Jung, K. Martens, C. Mauger, C. McGrew, E. Sharkey, B. Viren, C. Yanagisawa, W. Doki, K. Miyano, H. Okazawa, C. Saji, M. Takahata, Y. Nagashima, M. Takita, T. Yamaguchi, M. Yoshida, S. B. Kim, M. Etoh, K. Fujita, A. Hasegawa, T. Hasegawa, S. Hatakeyama, T. Iwamoto, M. Koga, T. Maruyama, H. Ogawa, J. Shirai, A. Suzuki, F. Tsushima, M. Koshiba, M. Nemoto, K. Nishijima, T. Futagami, Y. Hayato, Y. Kanaya, K. Kaneyuki, Y. Watanabe, D. Kielczewska, R. A. Doyle, J. S. George, A. L. Stachyra, L. L. Wai, R. J. Wilkes, and K. K. Young. Evidence for oscillation of atmospheric neutrinos. *Phys. Rev. Lett.*, 81:1562–1567, Aug 1998.

[15] The KATRIN Collaboration. Direct neutrino-mass measurement with sub-electronvolt sensitivity. *Nature Physics*, 18(2):160–166, 2022.

[16] Guo-yuan Huang, Werner Rodejohann, and Shun Zhou. Effective neutrino masses in KATRIN and future tritium beta-decay experiments. *Phys. Rev. D*, 101:016003, Jan 2020.

[17] Chiaki Yanagisawa. Looking for cosmic neutrino background. *Frontiers in Physics*, 2:30, 2014.

[18] James Alvey, Miguel Escudero, and Nashwan Sabti. What can CMB observations tell us about the neutrino distribution function? *Journal of Cosmology and Astroparticle Physics*, 2022(02):037, 2022.

[19] TMC Abbott, M Aguena, A Alarcon, S Allam, O Alves, A Amon, F Andrade-Oliveira, J Annis, S Avila, D Bacon, et al. Dark energy survey year 3 results: Cosmological constraints from galaxy clustering and weak lensing. *Physical Review D*, 105(2):023520, 2022.

[20] Nabila Aghanim, Yashar Akrami, Mark Ashdown, J Aumont, C Baccigalupi, M Ballardini, AJ Banday, RB Barreiro, N Bartolo, S Basak, et al. Planck 2018 results-vi. cosmological parameters. *Astronomy & Astrophysics*, 641:A6, 2020.

[21] Maria Goeppert-Mayer. Double beta-disintegration. *Physical Review*, 48(6):512, 1935.

[22] Ettore Majorana. Teoria simmetrica dell'elettrone e del positrone. *Il Nuovo Cimento (1924-1942)*, 14(4):171–184, 1937.

[23] AS Barabash. Experiment double beta decay: Historical review of 75 years of research. *Physics of Atomic Nuclei*, 74(4):603–613, 2011.

[24] E Der Mateosian and M Goldhaber. Limits for lepton-conserving and lepton-nonconserving double beta decay in ^{48}Ca. *Physical Review*, 146(3):810, 1966.

[25] Frank T Avignone III, Steven R Elliott, and Jonathan Engel. Double beta decay, majorana neutrinos, and neutrino mass. *Reviews of Modern Physics*, 80(2):481, 2008.

[26] Matteo Agostini, Giovanni Benato, and Jason A. Detwiler. Discovery probability of next-generation neutrinoless double-β decay experiments. *Phys. Rev. D*, 96:053001, Sep 2017.

[27] N Abgrall, I Abt, M Agostini, A Alexander, C Andreoiu, GR Araujo, FT Avignone III, W Bae, A Bakalyarov, M Balata, et al. Legend-1000 preconceptual design report. *arXiv preprint arXiv:2107.11462*, 2021.

[28] JB Albert, G Anton, IJ Arnquist, I Badhrees, P Barbeau, D Beck, V Belov, F Bourque, JP Brodsky, E Brown, et al. Sensitivity and discovery potential of the proposed nexo experiment to neutrinoless double-β decay. *Physical Review C*, 97(6):065503, 2018.

[29] Vicente Alvarez, Filipa IGM Borges, S Cárcel, JM Carmona, J Castel, JM Catalá, Susana Cebrián, A Cervera, D Chan, Carlos AN Conde, et al. Next-100 technical design report (tdr). executive summary. *Journal of Instrumentation*, 7(06):T06001, 2012.

[30] The CUPID Interest Group. Cupid: Cuore (cryogenic underground observatory for rare events) upgrade with particle identification. *arXiv preprint arXiv:1504.03599*, 2015.

[31] Junpei Shirai, KamLAND-Zen Collaboration, et al. Results and future plans for the kamland-zen experiment. In *Journal of Physics: Conference Series*, volume 888, page 012031. IOP Publishing, 2017.

[32] Xun Chen, ChangBo Fu, Javier Galan, Karl Giboni, Franco Giuliani, LingHui Gu, Ke Han, XiangDong Ji, Heng Lin, JiangLai Liu, et al. Pandax-III: Searching for neutrinoless double beta decay with high pressure ^{136}Xe gas time projection chambers. *Science China Physics, Mechanics & Astronomy*, 60(6):1–40, 2017.

[33] Valentina Lozza. The sno+ experiment. current status and future prospects. *Verhandlungen der Deutschen Physikalischen Gesellschaft*, 2016.

[34] Pavel P. Povinec. Background constrains of the supernemo experiment for neutrinoless double beta-decay searches. *Nuclear Instruments and Methods in Physics Research Section A: Accelerators, Spectrometers, Detectors and Associated Equipment*, 845:398–403, 2017. Proceedings of the Vienna Conference on Instrumentation 2016.

[35] R Arnold, C Augier, J Baker, AS Barabash, A Basharina-Freshville, M Bongrand, V Brudanin, AJ Caffrey, S Cebrián, A Chapon, et al. Probing new physics models of neutrinoless double beta decay with supernemo. *The European Physical Journal C*, 70(4):927–943, 2010.

[36] Fedor Šimkovic. Theory of neutrinoless double beta decay—a brief review. *Physics of Particles and Nuclei Letters*, 10(7):623–632, 2013.

[37] Zen Collaboration et al. First search for the majorana nature of neutrinos in the inverted mass ordering region with KamLAND-Zen. *arXiv preprint arXiv:2203.02139*, 2022.

[38] Samuel Carter Hedges. *Low Energy Neutrino-Nucleus Interactions at the Spallation Neutron Source*. PhD thesis, Duke University, 2021.

[39] Franz Mandl and Graham Shaw. *Quantum field theory*. John Wiley & Sons, 2010.

[40] Tina Leitner. Neutrino interactions with nucleons and nuclei. *Diplomat, Justus-Liebig-Universität Gießen*, 2005.

[41] Steven Gardiner. Simulating low-energy neutrino interactions with MARLEY. *Computer Physics Communications*, 269:108123, 2021.

[42] K Ikeda, S Fujii, and JI Funjita. The (p, n) reactions and beta decays. *Phys. Letters*, 3, 1963.

[43] E Caurier, K Langanke, G Martínez-Pinedo, and F Nowacki. Shell-model calculations of stellar weak interaction rates. I. Gamow-Teller distributions and spectra of nuclei in the mass range A = 45–65. *Nuclear Physics A*, 653(4):439–452, 1999.

[44] AL Cole, TS Anderson, RGT Zegers, Sam M Austin, BA Brown, L Valdez, S Gupta, GW Hitt, and O Fawwaz. Gamow-teller strengths and electron-capture rates for pf-shell nuclei of relevance for late stellar evolution. *Physical Review C*, 86(1):015809, 2012.

[45] Archana Saxena, Praveen C Srivastava, and Toshio Suzuki. *Ab initio* calculations of Gamow-Teller strengths in the sd shell. *Physical Review C*, 97(2):024310, 2018.

[46] DE Bainum, J Rapaport, CD Goodman, DJ Horen, CC Foster, MB Greenfield, and CA Goulding. Observation of giant particle-hole resonances in ^{90}Zr (p, n) ^{90}Nb. *Physical Review Letters*, 44(26):1751, 1980.

[47] T.N. Taddeucci, C.A. Goulding, T.A. Carey, R.C. Byrd, C.D. Goodman, C. Gaarde, J. Larsen, D. Horen, J. Rapaport, and E. Sugarbaker. The (p, n) reaction as a probe of beta decay strength. *Nuclear Physics A*, 469(1):125–172, 1987.

[48] Jonathan Engel and Javier Menéndez. Status and future of nuclear matrix elements for neutrinoless double-beta decay: a review. *Reports on Progress in Physics*, 80(4):046301, 2017.

[49] WC Haxton. Radiochemical neutrino detection via ^{127}I (ν_e, e^-) ^{127}Xe. *Physical review letters*, 60(9):768, 1988.

[50] G Martínez-Pinedo, A Poves, E Caurier, and AP Zuker. Effective g_A in the pf shell. *Physical Review C*, 53(6):R2602, 1996.

[51] M Ichimura, H Sakai, and T Wakasa. Spin–isospin responses via (p, n) and (n, p) reactions. *Progress in Particle and Nuclear Physics*, 56(2):446–531, 2006.

[52] BH Wildenthal, MS Curtin, and B Alex Brown. Predicted features of the beta decay of neutron-rich sd-shell nuclei. *Physical Review C*, 28(3):1343, 1983.

[53] Ian Stuart Towner. Quenching of spin matrix elements in nuclei. *Physics Reports*, 155(5):263–377, 1987.

[54] GF Bertsch and I Hamamoto. Gamow-teller strength at high excitations. *Physical Review C*, 26(3):1323, 1982.

[55] A Arima, K Shimizu, W Bentz, and H Hyuga. Nuclear magnetic properties and Gamow-Teller transitions. *Adv. Nucl. Phys*, 18(1), 1987.

[56] E Caurier, A Poves, and AP Zuker. Missing and quenched Gamow-Teller strength. *Physical review letters*, 74(9):1517, 1995.

[57] Tae-Sun Park, Hong Jung, and Dong-Pil Min. In-medium effective axial-vector coupling constant. *Physics Letters B*, 409(1-4):26–32, 1997.

[58] Morten Hjorth-Jensen, Thomas TS Kuo, and Eivind Osnes. Realistic effective interactions for nuclear systems. *Physics reports*, 261(3-4):125–270, 1995.

[59] T Siiskonen, M Hjorth-Jensen, and J Suhonen. Renormalization of the weak hadronic current in the nuclear medium. *Physical Review C*, 63(5):055501, 2001.

[60] Jason D Holt and Jonathan Engel. Effective double-β-decay operator for ^{76}Ge and ^{82}Se. *Physical Review C*, 87(6):064315, 2013.

[61] J Menéndez, D Gazit, and A Schwenk. Chiral two-body currents in nuclei: Gamow-teller transitions and neutrinoless double-beta decay. *Physical review letters*, 107(6):062501, 2011.

[62] Andreas Ekström, Gustav R Jansen, Kyle A Wendt, Gaute Hagen, Thomas Papenbrock, Sonia Bacca, Boris Carlsson, and Doron Gazit. Effects of three-nucleon forces and two-body currents on Gamow-Teller strengths. *Physical Review Letters*, 113(26):262504, 2014.

[63] J Engel, S Pittel, and P Vogel. Capture of solar and higher-energy neutrinos by ^{127}I. *Physical Review C*, 50(3):1702, 1994.

[64] John N Bahcall, Aldo M Serenelli, and Sarbani Basu. New solar opacities, abundances, helioseismology, and neutrino fluxes. *The Astrophysical Journal*, 621(1):L85, 2005.

[65] Yu S Lutostansky, AN Fazliakhmetov, GA Koroteev, NV Klochkova, AP Osipenko, and VN Tikhonov. Cross sections of solar neutrino capture by ^{127}I nuclei and Gamow-Teller resonances. *arXiv preprint arXiv:2103.12325*, 2021.

[66] T.E. Mason, D. Abernathy, I. Anderson, J. Ankner, T. Egami, G. Ehlers, A. Ekkebus, G. Granroth, M. Hagen, K. Herwig, J. Hodges, C. Hoffmann, C. Horak, L. Horton, F. Klose, J. Larese, A. Mesecar, D. Myles, J. Neuefeind, M. Ohl, C. Tulk, X-L. Wang, and J. Zhao. The spallation neutron source in Oak Ridge: A powerful tool for materials research. *Physica B: Condensed Matter*, 385-386:955–960, 2006.

[67] D Akimov, S Alawabdeh, P An, A Arteaga, C Awe, PS Barbeau, C Barry, B Becker, V Belov, I Bernardi, et al. The COHERENT experimental program. *arXiv preprint arXiv:2204.04575*, 2022.

[68] D Akimov, P An, C Awe, PS Barbeau, B Becker, V Belov, I Bernardi, MA Blackston, C Bock, A Bolozdynya, et al. Simulating the neutrino flux from the spallation neutron source for the COHERENT experiment. *Physical Review D*, 106(3):032003, 2022.

[69] D Akimov, P An, C Awe, Phillip S Barbeau, B Becker, V Belov, Igor Bernardi, MA Blackston, A Bolozdynya, B Cabrera-Palmer, et al. A D_2O detector for flux normalization of a pion decay-at-rest neutrino source. *Journal of Instrumentation*, 16(08):P08048, 2021.

[70] Ben Suh. Measuring the ^{127}I,ν_e charged-current cross-section of NaI[Tl]. 2016.

[71] M. Palarczyk, J. Rapaport, C. Hautala, D. L. Prout, C. D. Goodman, I. J. van Heerden, J. Sowinski, G. Savopulos, X. Yang, H. M. Sages, R. Howes, R. Carr, M. Islam, E. Sugarbaker, D. C. Cooper, K. Lande, B. Luther, and T. N. Taddeucci. Measurement of Gamow-Teller strength for ^{127}I as a solar neutrino detector. *Phys. Rev. C*, 59:500–509, Jan 1999.

[72] Y. Fujita, Y. Shimbara, I. Hamamoto, T. Adachi, G. P. A. Berg, H. Fujimura, H. Fujita, J. Görres, K. Hara, K. Hatanaka, J. Kamiya, T. Kawabata, Y. Kitamura, Y. Shimizu, M. Uchida, H. P. Yoshida, M. Yoshifuku, and M. Yosoi. $m1$ and Gamow-Teller transitions in $t = 1/2$ nuclei ^{23}Na and ^{23}Mg. *Phys. Rev. C*, 66:044313, Oct 2002.

[73] J. Rapaport, T. Taddeucci, T. P. Welch, C. Gaarde, J. Larsen, D. J. Horen, E. Sugarbaker, P. Koncz, C. C. Foster, C. D. Goodman, C. A. Goulding, and T. Masterson. Excitation of giant spin-isospin multipole vibrations in ^{54,56}Fe and ^{58,60}Ni. *Nucl. Phys. A*, 410(3):371–398, December 1983.

[74] N. Paar, T. Marketin, D. Vale, and D. Vretenar. Modeling nuclear weak-interaction processes with relativistic energy density functionals. *International Journal of Modern Physics E*, 24(9):1541004, 2015.

[75] Robin P. Gardner and Charles W. Mayo. NaI detector nonlinearity for PGNAA applications. *Applied Radiation and Isotopes*, 51(2):189–195, 1999.

[76] Glenn F Knoll. *Radiation detection and measurement*. John Wiley & Sons, 2010.

[77] R. Bernabei, P. Belli, A. Bussolotti, F. Cappella, R. Cerulli, C.J. Dai, A. d'Angelo, H.L. He, A. Incicchitti, H.H. Kuang, J.M. Ma, A. Mattei, F. Montecchia, F. Nozzoli, D. Prosperi, X.D. Sheng, and Z.P. Ye. The DAMA/LIBRA apparatus. *Nuclear Instruments and Methods in Physics Research Section A: Accelerators, Spectrometers, Detectors and Associated Equipment*, 592(3):297–315, 2008.

[78] Chris Hagmann, David Lange, Jerome Verbeke, and Doug Wright. Cosmic-ray shower library (cry). *Lawrence Livermore National Laboratory document UCRL-TM-229453*, 2012.

[79] Steven Gardiner. Nuclear de-excitations in low-energy charged-current ν_e scattering on ^{40}Ar. *Phys. Rev. C*, 103:044604, Apr 2021.

[80] G. P. Yost et al. Review of Particle Properties: Particle Data Group. *Phys. Lett. B*, 204:1–486, 1988.

[81] J B Birks. Scintillations from organic crystals: Specific fluorescence and relative response to different radiations. *Proceedings of the Physical Society. Section A*, 64(10):874–877, oct 1951.

[82] Hans A Bethe. Passage of radiations through matter. *Experimental nuclear physics*, 1953.

[83] L Reichhart, D Yu Akimov, HM Araújo, EJ Barnes, VA Belov, AA Burenkov, V Chepel, A Currie, L DeViveiros, B Edwards, et al. Quenching factor for low-energy nuclear recoils in a plastic scintillator. *Physical Review C*, 85(6):065801, 2012.

[84] VI Tretyak. Semi-empirical calculation of quenching factors for ions in scintillators. *Astroparticle Physics*, 33(1):40–53, 2010.

[85] Steven P. Ahlen. Theoretical and experimental aspects of the energy loss of relativistic heavily ionizing particles. *Rev. Mod. Phys.*, 52:121–173, Jan 1980.

[86] Patricia Dalton and JE Turner. New evaluation of mean excitation energies for use in radiation dosimetry. *Health Physics*, 15(3):257–262, 1968.

[87] JE Turner. Calculation of stopping power of a heavy charged particle in matter. *Health Physics*, 13(12):1255–1264, 1967.

[88] H. W. Joo, H. S. Park, J. H. Kim, S. K. Kim, Y. D. Kim, H. S. Lee, and S. H. Kim. Quenching factor measurement for NaI(Tl) scintillation crystal. *Astropart. Phys.*, 108:50–56, 2019.

[89] Y.J. Ko, G. Adhikari, P. Adhikari, E. Barbosa de Souza, N. Carlin, J.J. Choi, S. Choi, M. Djamal, A.C. Ezeribe, C. Ha, I.S. Hahn, E.J. Jeon, J.H. Jo, W.G. Kang, M. Kauer, G.S. Kim, H. Kim, H.J. Kim, K.W. Kim, N.Y. Kim, S.K. Kim, Y.D. Kim, Y.H. Kim, E.K. Lee, H.S. Lee, J. Lee, J.Y. Lee, M.H. Lee, S.H. Lee, D.S. Leonard, W.A. Lynch, B.B. Manzato, R.H. Maruyama, R.J. Neal, S.L. Olsen, B.J. Park, H.K. Park, H.S. Park, K.S. Park, R.L.C. Pitta, H. Prihtiadi, S.J. Ra, C. Rott, K.A. Shin, A. Scarff, N.J.C. Spooner, W.G. Thompson, L. Yang, and G.H. Yu. Comparison between DAMA/LIBRA and

COSINE-100 in the light of quenching factors. *Journal of Cosmology and Astroparticle Physics*, 2019(11):008–008, nov 2019.

[90] Jens Lindhard, V Nielsen, M Scharff, and PV Thomsen. Integral equations governing radiation effects. *Mat. Fys. Medd. Dan. Vid. Selsk*, 33(10):1–42, 1963.

[91] JD Lewin and PF Smith. Review of mathematics, numerical factors, and corrections for dark matter experiments based on elastic nuclear recoil. *Astroparticle Physics*, 6(1):87–112, 1996.

[92] Yu. S. Lutostansky and N. B. Shul'gina. Strength function of ^{127}Xe and iodine-xenon neutrino detector. *Phys. Rev. Lett.*, 67:430–432, Jul 1991.

[93] J. Engel, S. Pittel, and P. Vogel. Capture of solar and higher-energy neutrinos by ^{127}I. *Phys. Rev. C*, 50:1702–1708, Sep 1994.

[94] Aobo Li, Zhenghao Fu, Lindley A Winslow, Christopher P Grant, Hasung Song, Hideyoshi Ozaki, Itaru Shimizu, and Atsuto Takeuchi. KamNet: An integrated Spatiotemporal Deep Neural Network for Rare Event Search in KamLAND-Zen. *arXiv preprint arXiv:2203.01870*, 2022.

[95] Wei Zhang, Jun Tanida, Kazuyoshi Itoh, and Yoshiki Ichioka. Shift-invariant pattern recognition neural network and its optical architecture. In *Proceedings of annual conference of the Japan Society of Applied Physics*, pages 2147–2151, 1988.

[96] Yann LeCun, Bernhard Boser, John S Denker, Donnie Henderson, Richard E Howard, Wayne Hubbard, and Lawrence D Jackel. Backpropagation applied to handwritten zip code recognition. *Neural computation*, 1(4):541–551, 1989.

[97] Yann LeCun, Léon Bottou, Yoshua Bengio, and Patrick Haffner. Gradient-based learning applied to document recognition. *Proceedings of the IEEE*, 86(11):2278–2324, 1998.

[98] Zewen Li, Fan Liu, Wenjie Yang, Shouheng Peng, and Jun Zhou. A survey of convolutional neural networks: analysis, applications, and prospects. *IEEE transactions on neural networks and learning systems*, 2021.

[99] Tianqi Chen and Carlos Guestrin. Xgboost: A scalable tree boosting system. In *Proceedings of the 22nd acm sigkdd international conference on knowledge discovery and data mining*, pages 785–794, 2016.

[100] Jerome H Friedman. Greedy function approximation: a gradient boosting machine. *Annals of statistics*, pages 1189–1232, 2001.

[101] Wei-Yin Loh. Classification and regression trees. *Wiley interdisciplinary reviews: data mining and knowledge discovery*, 1(1):14–23, 2011.

[102] Peibo An and The COHERENT Collaboration. XGBoost based particle classifier, February 2022.

[103] P.A. Zyla et al.(Particle Data Group). Review of Particle Physics. *Progress of Theoretical and Experimental Physics*, 2020(8), 08 2020. 083C01.

[104] Toichiro Kinoshita and Alberto Sirlin. Radiative corrections to fermi interactions. *Phys. Rev.*, 113:1652–1660, Mar 1959.

[105] L Michel. Interaction between four half-spin particles and the decay of the μ-meson. 63(5):514–531, may 1950.

[106] Charalampos Anastasiou, Kirill Melnikov, and Frank Petriello. The electron energy spectrum in muon decay through $\mathcal{O}(\alpha^2)$. 2007(09):014–014, sep 2007.

[107] Andrzej Czarnecki, Matthew Dowling, Xavier Garcia i Tormo, William J. Marciano, and Robert Szafron. Michel decay spectrum for a muon bound to a nucleus. *Phys. Rev. D*, 90:093002, Nov 2014.

[108] Toichiro Kinoshita. Mass singularities of feynman amplitudes. *Journal of Mathematical Physics*, 3(4):650–677, 1962.

[109] T. D. Lee and M. Nauenberg. Degenerate systems and mass singularities. *Phys. Rev.*, 133:B1549–B1562, Mar 1964.

[110] T. Suzuki, D. F. Measday, and J. P. Roalsvig. Total nuclear capture rates for negative muons. *Phys. Rev. C*, 35:2212–2224, Jun 1987.

[111] Daniel Foreman-Mackey, David W. Hogg, Dustin Lang, and Jonathan Goodman. emcee: The MCMC hammer. *Publications of the Astronomical Society of the Pacific*, 125(925):306–312, mar 2013.

[112] Joanna Dunkley, Martin Bucher, Pedro G. Ferreira, Kavilan Moodley, and Constantinos Skordis. Fast and reliable Markov chain Monte Carlo technique for cosmological parameter estimation. *Monthly Notices of the Royal Astronomical Society*, 356(3):925–936, 01 2005.